2018

Association Between Mechanics And Biology In Vascular Graft Remodeling

David Andrew Prim
University of South Carolina

Association Between Mechanics and Biology in Vascular Graft Remodeling

by

David Andrew Prim

Bachelor of Science
University of South Carolina, 2013

Submitted in Partial Fulfillment of the Requirements

For the Degree of Doctor of Philosophy in

Biomedical Engineering

College of Engineering and Computing

University of South Carolina

2018

Accepted by:

John F. Eberth, Major Professor

Tarek Shazly, Committee Member

Jay Potts, Committee Member

Taixing Cui, Committee Member

Cheryl L. Addy, Vice Provost and Dean of the Graduate School

DEDICATION

The last five years would have been wholly different without the love and support of my family and friends. Most importantly, I would like to thank my wife, Rosanne, for her love, patience, understanding, and partnership; my parents, Harry and Cheryl, for their unwavering love and support throughout my life; and my dogs, Beauregard and Wheatley, for being a source of unbridled joy no matter the circumstances.

ACKNOWLEDGEMENTS

I would like to acknowledge first my advisor and mentor, Dr. John F. Eberth, for thoughtfully guiding my research while allowing me the freedom to make my own decisions and pursue my own interests in and out of the lab. I also would like to thank my committee members – Dr. Shazly, Dr. Potts, and Dr. Cui – for contributing their own candid guidance and advice. I would like to thank my fellow graduate students Brooks Lane and William Torres for regular conversations, commiseration, and advice. Finally, I would like to thank everyone at the School of Medicine and College of Engineering who has contributed advice, protocols, assistance, training, and more, when I sought their expertise.

ABSTRACT

Coronary artery bypass grafting (CABG) restores myocardial perfusion in patients with severe coronary artery disease by utilizing autografts – usually at least one of the internal thoracic artery (ITA), radial artery (RA), and great saphenous vein (GSV) – to bypass stenosed regions of coronary arteries. While decades of research and clinical improvements have made CABG an indispensable procedure, tens of thousands of grafts fail each year, which is due, at least in part, to an inability of the source vessels to adapt to the altered stimuli of the coronary circulation. In this dissertation, we first quantify and compare the mechanical deviation experienced by ITAs, RAs, and GSVs when subjected to coronary loads to better understand the nature and magnitude of forces stimulating remodeling processes. Those mechanical deviations are correlated with known clinical failure rates taken from large-cohort meta-analysis in existing literature. To better understand the early signaling and gene expression activity of grafts subjected to these coronary loads, we then culture ITAs, RAs, and GSVs in an ex vivo perfusion bioreactor for up to one week, identifying differential responses across source vessels that are associated with adaptive and maladaptive remodeling. Maladaptive remodeling processes and eventual graft failure may be associated with the large mechanical mismatching that results from implantation in the coronary circulation and the sudden exposure to coronary loading. We therefore test a stepwise approach wherein gradual increases in pressure and flow of ex vivo culture conditions over three weeks stimulate adaptive GSV remodeling while avoiding maladaptive pathways. This adaptive culture technique could be applied to

engineered grafts, such as xenografts to improve the material properties prior to decellularization. To demonstrate the range of scaffolds that may be available from animal donors, we evaluate the passive mechanical properties of carotid arteries from six species of mammal. Vascular graft remodeling may also be sensitive to the intricacies of applied pressure and flow waveforms, so we developed and validated a novel pulsatile perfusion bioreactor capable of replicating any in vivo hemodynamic waveform. The combination of these techniques and results furthers understanding of CABG failure and vascular remodeling, while also providing a framework for engineering improved vascular grafts.

TABLE OF CONTENTS

LIST OF TABLES

LIST OF FIGURES

CHAPTER 1

INTRODUCTION – VASCULAR MECHANOBIOLOGY

1.1 VASCULAR STRUCTURE AND FUNCTION

The mammalian vasculature evolved to distribute oxygenated, nutrient-rich blood from the myocardium through the arterial tree to capillaries throughout the body, to return deoxygenated blood through the venous system to the right atrium, and to circulate blood through the pulmonary system for reoxygenation. Most vessels share common basic characteristics; however, the structure of any given vessel is uniquely adapted to function optimally in its environment, which results in general differences between arteries and veins as well as large variation within each group [2]. Several discrete classifications are commonly used throughout the vascular tree, starting most proximal to the left ventricle, moving distally to capillary beds, and returning to the right atrium: elastic arteries, muscular arteries, arterioles, capillaries, venules, and veins. While these classifications are based on structural and functional patterns within each group, it is important to note that variations exist across vessels within groups (e.g., carotid vs. femoral elastic arteries) and even at different points along one vessel (e.g., proximal and distal aorta). Elastic arteries, muscular arteries, and veins are of primary interest herein due to their importance in disease and graft treatments, and further discussion will focus exclusively on these groups.

Blood vessels are generally considered to have three layers, or tunics: tunica intima, tunica media, and tunica adventitia. The differences in the relative size and constituent make-up of these layers allow for vessels to be distinguished histologically (e.g.,

comparing arteries to veins). The intima is the innermost layer and thus the one that is directly adjacent to the vessel lumen through which blood flows. In all blood vessels, it is a semi-porous membrane comprised primarily of endothelial cells (ECs) that interact with blood and the solutes therein by allowing selective transport into the vessel wall through several processes including diffusion, filtration, and pinocytosis [2]. Furthermore, the intima senses and responds to mechanical and chemical stimuli by releasing a variety of biochemical factors into the blood and into neighboring cells of the vessel wall [8].

In veins and arteries the media is separated from the intima by a basement membrane and layer of collagen type IV and elastin known as the internal elastic lamina. The media, usually accounting for most of the wall thickness, is composed of varying amounts of smooth muscle cells (SMCs), elastin, and collagen of primarily type III. SMCs are generally arranged in a helical alignment that is close to circumferential and are the primary regulators of peripheral blood flow via coordinated contraction or relaxation, which alters lumen diameter and thus resistance to flow at that location. While the intima is generally considered to have little mechanical strength, the media contributes much of the vessel's mechanical stability under physiologic loads (i.e., normal blood pressure and flow). In elastic arteries – the aorta and others proximal to it – the media is composed of many elastic lamellae that distend cyclically in response to increased pressure during systole which increases lumen diameter and volume. The vessel wall then retracts during diastole, ejecting stored blood. This effect of the elastic structure dampens pulsatility and results in steadier downstream perfusion. In muscular arteries, which are those distal to the aorta and other elastic arteries, the media has less elastin organized into fibers rather than concentric sheets, and more SMCs, as their primary function is selectively regulating flow

to distal tissues. Veins generally have little to no elastin beyond an internal and external elastic lamina as they experience exclusively steady flow, with a media composed largely of smooth muscle cells to control blood return to the right atrium of the heart [2,8].

The adventitia is the outermost layer of the blood vessel and is responsible for both mechanical strength and perivascular interactions. Much of the adventitia is composed of type I collagen arranged in an undulating pattern, whereby most fibers are arranged axially but others are circumferentially and helically aligned [8]. Fibroblasts (FBs) are the cells most closely associated with the adventitia, and they play an important role in extracellular matrix (ECM) protein deposition, among several other functions; however, the adventitia is also home to many other cell types, including progenitor cells, nerve cells, macrophages, T cells, B cells, mast cells, and dendritic cells. Phenotypic plasticity of fibroblasts and other progenitor cells is particularly important to this work, as such differentiation further enables remodeling as well as repopulation of damaged tissue [9]. Moreover, in larger vessels where the intima does not provide a sufficient source of solute transport, the adventitia is home to a microvasculature that supplies resident vascular cells known as the vasa vasorum [8].

Broadly speaking, it is important to recognize that blood vessel structure in any given location along the vascular tree is a result of the functional needs and stimuli applied throughout development at that location. Furthermore, vascular properties are endowed not only by the overall composition of cells and ECM but by their specific orientation and distribution throughout the wall. This results in distinct structure and function for large groups (e.g., veins, elastic arteries, muscular arteries) as well as variations within those groups.

1.2 CORONARY ARTERY BYPASS GRAFTING

One of the most common – and dangerous – pathologies affecting the vasculature is coronary artery disease (CAD), characterized by atherosclerosis of the coronary arteries that supply the heart muscle with the oxygenated blood it needs to maintain normal function. While other treatment options exist for early stages of CAD, severe cases are usually treated with a vascular graft(s) to bypass the stenosed section(s) of the coronary vasculature, which can include the right coronary artery, left main coronary artery, circumflex artery, and left anterior descending (LAD) coronary artery. These coronary artery bypass grafts (CABGs) were first developed in the 1960s and have since grown in use to the point that over 400,000 procedures are performed in the U.S. each year [10,11].

The internal thoracic artery (ITA), radial artery (RA), and great saphenous vein (GSV) are the most common conduits utilized for CABG, with the gastroepiploic and epigastric arteries used less frequently. The left ITA, also known as the left internal mammary or LIMA, provides a unique graft option, as it branches off the left subclavian artery in situ and runs along the left side of the sternum just superficial to the anterior side of the heart. When a patient requires bypass of the LAD, the left ITA can thus be used by leaving the proximal end of the artery intact, freeing a length of the vessel, and making a single anastomosis beyond the blockage in the LAD (Figure 1.1). This method has become the consensus first choice bypass conduit, while the right ITA can be used to bypass a second coronary artery in a similar fashion but is done so less frequently [12,13]. For CABGs involving the RA, GSV, or other graft conduits, the graft tissue must be fully excised from its in situ location and implemented in the coronary circulation with two anastomoses (Figure 1.1 A). Usually the proximal anastomosis is made to the aortic root,

while the distal anastomosis is made to the coronary artery beyond the blockage; however, in some cases surgeons use more complex configurations such as a GSV branching off of a left ITA (i.e. "Y graft") or an RA being used to extend a right ITA. A more thorough discussion of the current considerations that go into graft selection can be found in [7].

Importantly, despite the vast amount of collective experience and incremental improvements in CABGs over time, approximately 6% of patients – 24,000 people – experience some level of graft failure within the first year alone [14]. Of these, wide variations in first year failure rates exist between common graft tissues, with GSVs failing most often (15.3%), ITAs least often (4.9%), and RAs in between these two (9.8%) [15]. GSVs continue to have the highest rates of failure long term, with 39% losing patency by 10 years post operation [16]. Despite the undesirable rate of failure, GSVs continue to be an important graft conduit due to their length, appropriate caliber, superficial location, and redundant circulation, as well as the prevalence of multi-vessel CAD necessitating grafts beyond the first choice left ITA. Reports suggest that at least 2/3 of CABG patients receive at least one GSV graft [17,18].

Understanding CABG failure and improving long term graft patency has long been an important topic of clinical and basic science research. Graft failures are most often the result of intimal hyperplasia, stenosis of the graft via cell infiltration, proliferation, and ECM deposition between the media and intima resulting in significant lumen narrowing. While intimal hyperplasia progression has been well characterized, specific causes and mechanisms are not as well understood [19–21]. Clinicians and researchers generally agree that molecular mechanisms, vascular injury, and mechanical factors all contribute to graft failure and the differential outcomes of various graft conduits. Molecular mechanisms

involve the overexpression of growth factors in response to highly altered flows, immune cell accumulation, and calcification [19,22,23]. Vascular injury can easily occur perioperatively through mishandling of tissue during graft harvesting and preparation; specifically, damage to ECs inhibits production of anti-thrombogenic factors, further initiating inflammatory processes [24]. Mechanical factors leading to graft failure include compliance mismatch at anastomoses; hemodynamic factors such as disturbed flow at anastomoses, pulsatility in vein grafts, and altered wall shear stress; and wall structure incapable of effectively distributing loads in the coronary circulation [15]. As discussed in greater detail below, the ability of CABGs to adapt to the stimuli present in the coronary circulation is imperative to their success.

1.3 VASCULAR HOMEOSTASIS AND REMODELING

150 years ago Virchow and contemporaries began to recognize the importance of cells to effecting changes in tissues [25]. Then in the 1890s, Wolff observed that chronic changes to the mechanical forces applied to living tissues result in structural changes in response to the altered stimuli. These observations have been further refined and expanded over time into the concept of mechanical homeostasis, or the idea that tissues organize partly in response to the mechanical loads acting upon them to achieve some unknown stress distribution, maintain this state through regular tissue turnover, and then remodel in response to chronically altered loads to restore the original homeostatic stress state [26]. Blood vessels are no exception, responding to genetic cues and local loading conditions through growth and development to distribute hemodynamic loads in the mature state, then responding to chronic deviations such as endurance training, hypertension, or indeed, grafting [8,27–29].

The primary forces acting on blood vessels and driving growth and remodeling are the frictional force of flowing blood along the intima, the normal force of pressurized blood pushing outward on the vessel wall, and axial force along the length of the vessel due to somatic growth. To more accurately account for how forces are distributed based on an individual vessel's geometry and how those forces may be sensed at the cellular level, vascular mechanics are often considered in a continuum mechanics framework, whereby stresses describe forces acting on an oriented area. The primary stresses of interest here are wall shear stress (τ_w), circumferential stress (σ_θ), and axial stress (σ_z) [8]:

$$\tau_w = \frac{4\mu Q}{\pi r_i^3} \quad , \quad \sigma_\theta = \frac{P r_i}{r_o - r_i} \quad , \quad \sigma_z = \frac{F}{\pi\left(r_o^2 - r_i^2\right)} \quad , \tag{1.1}$$

where r_o and r_i are the deformed outer and inner radius, μ the fluid viscosity, Q the volumetric flow rate, P the pressure, and F the axial force. Following the theory of mechanical homeostasis, healthy mature blood vessels exist at some homeostatic values of τ_w^h, σ_θ^h, and , σ_z^h, which we collectively refer to as the homeostatic stress state. Thus, deviations to the homeostatic stress state initiate remodeling processes to regain original values. While these formulae are simplified mean values of physiological stresses that do not fully capture the mechanical deformations of the vessel wall, they do provide a general framework to understand the remodeling processes that might be initiated in response to chronically altered loads.

As an example of particular relevance here, we might look at the theoretical remodeling that should occur for a great saphenous vein used a replacement graft for a left anterior descending coronary artery (Figure 1.2). At approximate in vivo values of Q = 0.17 mL/s and P = 20 mmHg [3], representative experimental values r_o = 2.35 mm, r_i =

1.98 mm, and $F = 0.409$ N (see Chapter 6), and assuming $\mu = 4.6$ mPa·s [30], homeostatic stress values can approximated from (1.1) as $\tau_w^h = 0.13$ Pa, $\sigma_\theta^h = 14.2$ kPa, and $\sigma_z^h = 81.1$ kPa. Subjecting the same vessel to conditions characteristic of the coronary circulation where $Q = 0.52$ mL/s and $P = 100$ mmHg [31], representative experimental values become $r_o = 2.52$ mm, $r_i = 2.18$ mm, and $F = 0.415$ N, and grafted stress values can be approximated as $\tau_w = 0.29$ Pa, $\sigma_\theta = 84.9$ kPa, and $\sigma_z = 82.2$ kPa. In this hypothetical scenario, we can see that τ_w and σ_θ are increased in the coronary circulation, while σ_z remains relatively unchanged. Thus, in the absence of other factors and making the reasonable assumption that μ and Q are relatively constant, one can see that increasing r_i is the only way that the vessel will restore its homeostatic value of τ_w, which would then require r_o to increase at a faster rate than r_i – increasing wall thickness – in order to restore homeostatic levels of σ_θ. It is worth noting that, while σ_z would have been unchanged between the two loading environments without remodeling, an increase in wall thickness would then decrease σ_z, which would create a conflict in this theoretical scenario and potentially lead to other remodeling processes such as changing fiber orientation, reducing axial force, or altering axial prestretch [32].

Indeed, significant evidence supports the theory of mechanical homeostasis and adaptive remodeling. In a canine model of adaptive remodeling, Kamiya and Togawa demonstrated that veins restore preoperative values of shear rate by increasing vessel radius in response to increased flow in the graft environment [33], while Langille and O'Donnell demonstrated that decreasing flow produces a compensatory decrease in diameter [34,35]. More recently, Baeyens and colleagues provide compelling physiological evidence

associated with molecular mechanisms to support the concept of a shear stress set point or homeostatic value that can vary between vessels of different function [36]. Hayashi and colleagues further show that flow-induced remodeling and restoration of homeostatic τ_w occurs independently of pressure in a thorough analysis of murine carotid artery remodeling in vivo, and they similarly show that τ_w restoration through vessel remodeling occurs in response to lowered flow equally well as increased flow [37].

Matsumoto and Hayashi utilized a murine model to demonstrate normalization of hoop (i.e., circumferential σ_θ) stress through wall thickening in response to hypertension [28], and this finding has been corroborated in hypertensive veins as well [38]. More recently, Matsumoto and colleagues show that, in an arteriovenous shunt of the common carotid artery, rabbit carotids maintain a relatively constant hoop stress despite increased r_i in response to increased Q [39]. Fridez and colleagues show similar results of eccentric hypertrophy, with thickness increasing while r_i remains constant; however, by analyzing temporal adaptations over 56 days, they also demonstrate that the stress-strain response shifts such that the vessel is compliant about the higher postoperative pressures [40]. In a study of hypertensive porcine coronary veins, Choy and colleagues show a compensatory thickening of the vein in response to increased σ_θ that is localized to regions that are not supported by perivascular tissue, further supporting that local stresses drive local remodeling [41].

Axial stress (σ_z) homeostasis has generally been given less scrutiny than τ_w and σ_θ by researchers. While Q and P can be selectively modulated relatively easily through knockout models, therapeutics, and surgical procedures such as banding to evaluate

remodeling outcomes, F is not as easily modulated without affect other stimuli, and F is also not intuitively associated with altered hemodynamics in the same way as the other parameters. As part of a series on vein graft experiments in dogs, Dobrin and colleagues overstretched end-to-end vein grafts and found that overstretching increased unstretched length after three months and led to insignificant wall thickening without intimal hyperplasia [42]. Qualitatively, this suggests a reduction in σ_z from the acute grafted state to experimental end point, but the axial stress data was not quantified. While significant evidence supports at least partial maintenance or restoration of τ_w^h and σ_θ^h, in studies where Q and P have been altered resulting in morphometric adaptations neither σ_z nor axial strain were maintained [39,43]. More investigations have been undertaken in ex vivo tissue culture experiments, whereby researchers have additional freedom to manipulate axial loads which are discussed below [44].

In addition to remodeling resulting from the three primary stresses described above, consideration must also be given to the cyclic stresses resulting from pulsatility in the arterial circulation, as each of the parameters described above can vary throughout the cardiac cycle. For example, Powell and Gosling synthesize the findings of several relevant studies to conclude that minimizing circumferential strain via external stenting ameliorates progression of intimal hyperplasia and medial thickening [45]. On the other hand, Eberth and colleagues demonstrated in a series of murine banding models that increased pulsatility has significant effects on remodeling processes and mechanical properties, even when there is little change to mean values of flow and pressure [46,47]. For CABG to be successful, especially those involving GSVs, grafts must adapt not only to altered mean values of stresses and strains but also altered cyclic loads due to unique coronary hemodynamics.

1.4 MECHANOTRANSDUCTION IN GRAFT REMODELING

Mechanotransduction is the process by which cells sense and respond to mechanical forces acting upon them via cell-cell junctions, ECM attachment, and internal cytoskeletal proteins, and respond via a variety of processes including release of kinases, transcription factors, protein synthesis and remodeling, cell differentiation, cell migration, and cell proliferation [48–50]. Researchers have explored many pathways by which vascular cells sense and respond to stimuli in the context of CABG and have found numerous mechanisms implicated in the upstream signaling leading to eventual adaptive remodeling or pathological maladaptation, with methods spanning cell culture, tissue culture, and in vivo experimentation [51,52]. To better understand the clinical and remodeling outcomes described above and to craft new strategies for improving grafts, one must understand the underlying processes and stimuli affecting graft adaptation.

ECs have received the most attention with respect to mechanotransduction, as they directly sense τ_w, σ_θ, and σ_z, although ECs in the intima of blood vessels were long considered to only have a passive role in preventing thrombosis until Hollis and Bolitho discovered that vascular ECs secrete biomolecules in response to mechanical stimulation [53]. Since then, researchers have shown many differential responses in relation to Q and τ_w: static versus steady flow (e.g., Malek, Greene, & Izumo, 1993; Shyy, Hsieh, Usami, & Chien, 1994), low versus high shear [56], laminar versus turbulent flow [57], oscillatory versus pulsatile flow [58], and steady versus pulsatile flow (e.g., Blackman, García-Cardeña, & Gimbrone, 2002; Hsiai et al., 2003). A large body of research is also built around the effects of cyclic stretch (and thus σ_θ) on ECs: uniaxial versus biaxial planar stretching [61], magnitudes of uniaxial cyclic stretching [62], and combining shear stress

with cyclic circumferential stretch [63]. These phenomena have been synthesized and reviewed in detail by several authors [48,64–66].

Similarly, robust data describes mechanotransduction in vascular SMCs and FBs. Leung and colleagues found that stretching of blood vessels induces collagen deposition, suggesting not only signaling but protein deposition within the vessel wall in response to mechanical stimuli [67]. Leung et al.'s findings highlight an important distinction between ECs in the intima and SMCs and FBs in the media and adventitia; mechanotransduction in ECs primarily signals other processes through biochemical activity, while SMCs and FBs are involved in direct ECM remodeling with a lesser role in mechanotransduction. In other words, while the intima contributes negligible mechanical stability, medial and adventitial homeostasis are dependent on intact EC signal transduction [68,69]. These collective findings provide further evidence supporting both the importance of functional endothelium in CABGs and the delicate balance necessary to signal and effect graft adaptation without promoting maladaptation.

The effects of the intricacy of pulsatile pressure and flow waves on remodeling outcomes must also be considered. Well characterized hemodynamic differences exist throughout the vascular tree, particularly in the arterial circulation [70–72], and previous research has demonstrated synthesis of vasoreactants in response to variable oscillatory flow conditions [58]. Further, deviations from physiological hemodynamics can lead to deleterious pathologies [73]. Preliminary evidence demonstrates a differential response to intricacies of flow waveforms beyond the fundamental frequency. For example, Dai and colleagues demonstrate that cultured human ECs exhibit differential gene expression and functional characteristics following exposure to pulsatile shear stress characteristic of two

regions along the carotid artery [74]. Feaver and colleagues further demonstrate the sensitivity of inflammation pathways within cultured ECs to individual harmonics of the Fourier transform of human carotid artery flow waves [75]. As the mechanisms and implications of this hemodynamic sensitivity have not been fully explored, further exploration is necessary to understand the level of biomimetic replication necessary to maintain or restore homeostasis and to elucidate the specific signaling and gene expression mechanisms that support such processes.

1.5 EX VIVO TISSUE CULTURE

Studying vascular remodeling presents a logistical challenge, as plated cell-based experiments inherently change the microenvironment and thus the stimuli acting on vascular cells, while in vivo experiments in humans or animals are limited in their ability to isolate and control individual stimuli. Vascular tissue culture poses its own unique set of challenges but generally provides an acceptable compromise between freedom to test and observe hypotheses while maintaining a 3D loading environment and similar mechanical parameters. Some issues with ex vivo models of vascular remodeling in general include loss of vasa vasorum, loss of innervation, and surgical manipulation; however, for studying CABG adaptations these factors are the same in clinical procedures. An additional point of consideration for ex vivo tissue culture is the absence of immune cells such as macrophages that play a role in injury response and graft adaptation.

Many groups have utilized forms of ex vivo tissue culture to assess vascular remodeling. Early studies focused on very short term effects – 24 hours or less – such as endothelial permeability [76] and cholesterol content [77]; however, studies quickly moved to longer time points, including demonstrating viability for almost one month depending

on the applied conditions [78]. Ex vivo culture also affords the ability to investigate gene expression and protein synthesis in response to specific stimuli [79,80,52,81]. Ex vivo culture has also found that both active and passive mechanical changes due to remodeling occur as early as 3 days after chronically altered stimuli [82].

Many ex vivo culture apparatus to date have utilized some form of roller pump that outputs nonspecific pulsatile flow [83] or dampened, mostly steady flow [84]. However, considering the sensitivity of vascular cells to specific flow and pressure waveforms, ex vivo tissue culture may also be affected by applied fluid dynamics from bioreactor pumps. Several groups have described models methods to model and recreate biomimetic waveforms [85–89], and still others have developed experimental apparatus capable of recreating physiological flows on the benchtop [90–93]. Few bioreactors for ex vivo tissue culture have incorporated this level of biomimetic fidelity, and such attention to detail may well become more important as we continue to learn about the effects of hemodynamic specificity on vascular remodeling.

1.6 CABG TISSUE CULTURE

Ex vivo tissue culture experiments relating to CABG are of particular interest to in this dissertation. Several groups have used ex vivo tissue culture to understand vein graft failure, utilizing the tunability of ex vivo culture systems to isolate the effects of specific stimuli. In a series of experiments, Gusic and colleagues evaluated GSVs after 7 days under a variety of flow conditions, finding that ramping applied pressure over 7 days leads to a greater increase in wall thickness than acute exposure to arterial conditions and alteration stress-strain relationships, while acute exposure to graft conditions leads to endothelial denudation and cell death [84,94]. Another research group has published a series of

investigations based on 7 and 14 day human saphenous vein cultures, showing that intimal thickening is stimulated within 7 days of ex vivo culture under arterial conditions, and expression of MMP2, MMP9, TIMP1, and PAI-1 are all increased by arterial shear stress [52,95,96]. In a separate research group, shorter investigations with human saphenous veins (1-4 days) have demonstrated loss of cell density, apoptosis, and induction of cytosine-rich protein (CRP3/MLP) that influences cell proliferation, with CRP3/MLP being correlated with increased circumferential stretch but not wall shear stress [97,98]. Dummler and colleagues compare viability of human saphenous veins under venous and arterial ex vivo culture conditions, finding that GSVs under venous conditions survive for up to 14 days but die by 8 days under arterial conditions while upregulating MMP2 expression [83].

In another series of investigations, Piola, Prandi, and colleagues have perhaps taken the broadest range of observations about the effects of CABG-like tissue culture on human saphenous veins. In 7 day experiments, GSVs cultured under arterial conditions show wall thinning, rearranging muscle fibers, and partial endothelial denudation [99]. Similar 7 day experiments went on to demonstrate differential expression of remodeling-associated genes and microRNAs, increased vasa vasorum density, and increasing presence of progenitor cells due to coronary loading conditions. Another creative investigation demonstrated that a trans-wall oxygen gradient mimicking grafted conditions triggers cell proliferation in the vasa vasorum, which could be an upstream factor in restenosis [100].

To the best of our knowledge, two CABG tissue culture experiments have incorporated recreation of physiological flow waves into their bioreactors. Voisard and colleagues use a Windkessel model to compare the effects of arterial versus venous

waveforms on human GSVs, demonstrating reactive cell proliferation starting at day 4 as well as media thinning. Recent work from Piola and colleagues also cultured human GSVs under biomimetic coronary conditions, demonstrating medial thinning, endothelial denudation, and apoptosis that aligned with their earlier work [101]. Further experimentation will be necessary to determine whether accurate replication of physiological flow and pressure waves has a differential effect from steady flow or simple sinusoid flow patterns.

1.7 SUMMARY

Blood vessel structure, mediated by resident vascular cells, is inherently linked to applied mechanical loads in a given circulatory environment, especially axial force and oscillatory pressure and flow. Large, chronic alterations to those loads trigger remodeling processes within blood vessels, which, in the case of CABGs, results in either successful remodeling adaptation to the coronary circulation or unsuccessful, maladaptive remodeling and eventual graft failure. In this dissertation, we aim to understand why failures occur differentially across CABG tissues through (i) mechanical characterization and comparison of graft vessels in their native state and under coronary loads (Chapter 2) and (ii) observation of early biological response of graft vessels subjected to coronary loads ex vivo to explore whether remodeling capacity is similar across graft vessels (Chapter 3). We then aim to build upon that knowledge and build upon previous literature to improve adaptive remodeling of graft vessels through stepwise manipulation of graft loading conditions over an extended culture period (Chapter 6).

In most previous ex vivo tissue culture investigations, precise replication of physiological flow and pressure waves is neglected, which may affect growth and

remodeling processes. To better understand the importance of biomimetic pulsatility and facilitate graft development going forward, we design and validate a bioreactor capable of replicating arterial fluid dynamics (Chapter 4). Future translational application of this work may likely include guided ex vivo culture toward tissue engineering of graft vessels, with decellularized and reseeded xenografts being one potential candidate for ex vivo culture applications. As an example of a potential catalog of xenograft scaffolds, we mechanically characterize carotid arteries across several mammalian species (Chapter 5). As a whole, this dissertation seeks to better understand why CABGs fail and explore avenues for future graft improvement through mechanical stimulation in ex vivo tissue culture.

1.8 FIGURES

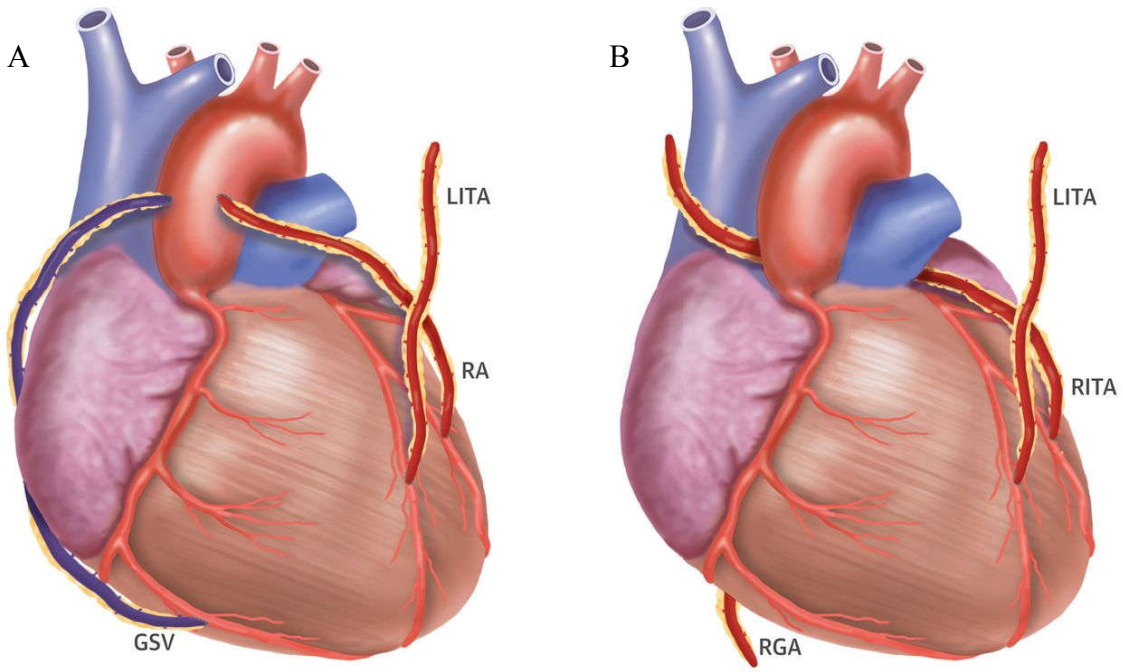

Gaudino, M. et al. J Am Coll Cardiol. 2015; 66(15):1729-37.

Figure 1.1 – (A) Diagram of heart with three CABGs: GSV from aortic root to right marginal artery, left ITA with single anastomosis to LAD; and RA from aortic root to diagonal branch of LAD; (B) Diagram of heart with three CABGs: left ITA with single anastomosis to LAD, right ITA with single anastomosis to diagonal branch of LAD, and right gastroepiploic artery with single anastomosis to distal right coronary artery [7].

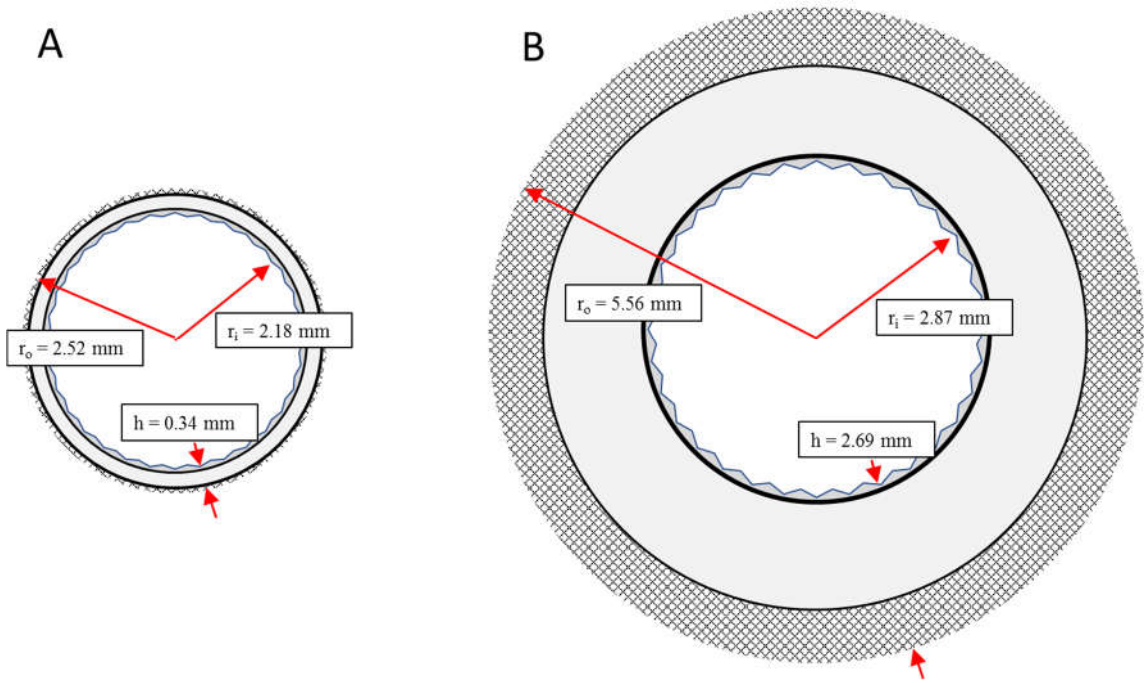

Figure 1.2 – Hypothetical remodeling of GSV to restore in vivo homeostatic values of τ_w^h and σ_θ^h under coronary loading conditions (Q = 0.52 ml/s, P = 102 mmHg): (A) scale diagram of native GSV deformed under coronary loads, and (B) scale diagram of GSV remodeled to restore homeostatic stresses.

CHAPTER 2

A MECHANICAL ARGUMENT FOR THE DIFFERENTIAL PERFORMANCE OF CORONARY ARTERY GRAFTS[1]

[1] Prim, D. A., Zhou, B., Hartstone-Rose, A., Uline, M. J., Shazly, T., & Eberth, J. F. (2016). *Journal of the Mechanical Behavior of Biomedical Materials*, *54*, 93–105. http://doi.org/10.1016/j.jmbbm.2015.09.017

2.1 ABSTRACT

Coronary artery bypass grafting (CABG) acutely disturbs the homeostatic state of the transplanted vessel making retention of graft patency dependent on chronic remodeling processes. The time course and extent to which remodeling restores vessel homeostasis will depend, in part, on the nature and magnitude of the mechanical disturbances induced upon transplantation. In this investigation, biaxial mechanical testing and histology were performed on the porcine left anterior descending artery (LAD) and analogs of common autografts, including the internal thoracic artery (ITA), radial artery (RA), great saphenous vein (GSV) and lateral saphenous vein (LSV). Experimental data were used to quantify the parameters of a structure-based constitutive model enabling prediction of the acute vessel mechanical response pre-transplantation and when loaded as an LAD replacement graft. A novel metric Ξ was developed to quantify mechanical differences between each graft vessel in situ and the LAD in situ, while a second metric Ω compares the graft vessels in situ to their grafted state in the coronary vasculature. The relative values of these metrics among candidate autograft sources are consistent with vessel-specific variations in CABG clinical success rates with the ITA as the superior and GSV the inferior graft choices based on mechanical performance. This approach can be used to evaluate other candidate tissues for grafting or to aid in the development of synthetic and tissue engineered alternatives.

2.2 INTRODUCTION

Coronary artery grafts bypass (CABG) can restore long-term myocardial perfusion following advanced-stage coronary artery disease [102]. Annually more than 400,000 CABG procedures are performed in the United States alone. The health care cost of these CABG procedures is close to 200 billion USD [103,104]. Despite decades of improvements

to surgical techniques, approximately 6% of all CABGs fail in the first year, putting patients with compromised cardiovascular systems at greater risk of myocardial infarction and other pathologies [14]. Failure rates depend strongly on the source tissue. For example, when collated from large clinical outcomes 15.3% of great saphenous veins fail in the first year while only 4.87% of internal thoracic failures occur [105–117]. By comparison, when used as a CABG graft, the radial artery has first year failure rates around 9.78% [105–117]. Although numerous factors contribute to the differential response, the mechanical mismatch of the grafted vessel with the host environment likely underlies a multitude of etiologies including ischemia, hemorrhage, dissection, inflammation, and restenosis [42,118,119].

Grafted vascular tissue must undergo an adaptive growth and remodeling process to retain optimal performance under the new mechanical loads imposed by the coronary circulation including altered blood pressure, flow, and axial force [32,33,46,120,121]. These loads generate mechanical signals that are sensed by vascular endothelial, smooth muscle, and fibroblast cells eliciting gene expression pathways that lead to microstructural adaptations and tissue reorganization [48]. Stress provides a continuum mechanics-based metric to assess the effects of loading on the local mechanical environment of vascular cells, specifically intramural stresses that act in the circumferential and axial directions as well as flow induced wall shear stresses acting on the endothelial-lined lumen [8,122]. Biaxial mechanical testing, typically inflation and extension of a tubular tissue sample, and subsequent data processing in the framework of finite elasticity are necessary to quantify the intramural stresses in the vessel wall [8]. Wall shear stress on the other hand, is dependent on the flow velocity profile and exponentially related to the vessel's radius, a

structural property. Compliance provides an additional structure-based measure that is fundamental to a graft's performance in a pulsatile environment. Collectively, these passive mechanical responses are determined by the geometry, orientation, and composition of the extracellular matrix proteins present in the wall [123–125].

Currently, the most common tissue sources for grafting to the left anterior descending coronary artery (LAD) include the internal thoracic (also known as the internal mammary) artery (ITA), radial artery (RA), and great saphenous vein (GSV) [13,18,102,113]. The anatomical and functional location of each graft vessel (i.e., ITA, RA, and GSV) along the vascular tree (Figure 2.1) determines the native mechanical loading environment, which, in concert with vessel-specific properties, give rise to a vessel-specific homeostatic state. For example, the LAD and ITA nominally experience highly pulsatile blood flow, and as a result exhibit high mechanical compliance to dampen pulsatility and reduce cardiac preload [2,126]. The RA is subjected to slightly lower blood pressures but less pulsatility than the LAD and ITA, resulting in a less compliant and more muscular structure [127,128]. The GSV and LSV are subjected to substantially lower pressures across a more narrow range, giving rise to a venous architecture that is structurally and compositionally different from its arterial counterpart [2,83,129–131]. Concatenate with hemodynamic loading, somatic growth influences these tissues to experience in situ axial load [32]. This manifests as an axial extension as evidenced by an immediate retraction upon excision to relieve the axial force. These axial loads are very different than the neutral axial loads surgeons create during a CABG procedure [132].

The differential performance of CABG grafts have been highlighted in numerous clinical studies that include long-term metrics such as graft patency [18,110,113],

reintervention rates [107], case-matching [107,133], and meta-analysis [13,18]. These studies identified the ITA as the superior performer in terms of clinical outcomes due to its anatomical position – descending from the subclavian and running very close to the heart in its normal anatomical position – requiring only one site of anastomosis to achieve coronary perfusion [102]. In many cases however, the ITA is not available and a second source tissue needs to be selected. GSV grafts were historically the preferred choice due to their superficial anatomical position, non-branching morphology, and comparable caliber to coronary arteries [113,134]. Other autologous source tissue options include RAs and GSVs, and far less commonly the right gastroepiploic artery or inferior epigastric artery [110,112]. RAs have similar caliber and have superficial location, but RAs suffer from susceptibility to vasospasm, calcification, intimal hyperplasia, and are relatively poor in patients with peripheral artery disease [135].

Here we investigated if mechanical differences among autologous vascular tissue sources, particularly under pre- and post-grafting loading conditions, correspond with differences in clinical outcomes. To this end, we quantified the passive mechanical response of the healthy porcine LAD and a host of candidate vessels used as LAD replacement grafts under uniform LAD loads. Obtained mechanical data were processed in a continuum mechanics-based framework, enabling prediction of each vessel's mechanical response under varied loading conditions. Vessel-specific mechanical metrics that account for changes caused by grafting were developed and found to correlate with reported clinical outcomes. Our findings help explain differential outcomes following autologous grafting in the coronary artery and can be extended towards the development

and assessment of other grafting alternatives (i.e. alternative tissue sources and tissue engineered materials).

2.3 MATERIALS AND METHODS

2.3.1 Tissue Acquisition and Handling

All porcine tissue was obtained fresh from a local abattoir and dissections were performed immediately following tissue acquisition. Isolated blood vessels included the LAD, ITA, RA, GSV, and an additional vessel, the lateral saphenous vein (LSV) (Figure 2.1). While there is no true translational equivalent to the porcine lateral saphenous vein in humans, it is included due to its prevalence in other veterinary studies and similar caliber to the porcine great saphenous vein. American Yorkshire pigs were used in this study and all animals were 6 month old ± 1 week. All target vessels were dissected as a set from the same animal (n=6), and animal weights ranged from 102-113 kg. Upon dissection each vessel was stored in a sterile solution of 1% phosphate buffered saline (PBS) and refrigerated until mechanical testing could be performed, which was always within 24 hours of tissue dissection.

2.3.2 Biaxial Mechanical Testing

Mechanical testing was carried out using a Bose BioDynamic 5270 biaxial mechanical testing device. Vessels were cut to approximately 20 mm tubular sections, and initial measurements were taken of the unloaded length, outer diameter, and wall thickness. All measurements were made along the middle section of each vessel to avoid extreme conditions at proximal and distal ends. Each vessel was mounted into the testing chamber of the biaxial testing device; the chamber was filled with Krebs-Henseleit solution (37 deg C and pH 7.4); and sodium nitroprusside (10^{-5} M) was flushed through the vessel and

device tubing at 60 mL/min to elicit the fully relaxed (passive) state of the SMCs and to remove all air from the flow loop.

Each vessel was axially extended by approximately 40% of the unloaded length at a displacement rate of 0.01 mm/s and pressures of 60 mmHg, 100 mmHg, and 140 mmHg. The *in vivo* axial stretch ratio was then determined to be the intersection of resultant axial force vs. displacement curves. This phenomenological observation of *in vivo* axial stretch has been documented historically and in our prior work [136,137]. Each vessel then underwent five cycles of pressurization for preconditioning, helping to ensure reproducible results. For data collection, pressure was increased from 20 to 200 mmHg at a constant rate of approximately 1.3 mmHg/s while pressure-outer diameter and pressure-longitudinal force curves were recorded at an axial stretch ratio below the *in vivo* value. Data collection was then carried out at the approximated *in vivo* stretch ratio and again above the *in vivo* stretch ratio. Between tests, axial displacement was increased at a rate of 0.01 mm/s, and the vessel was allowed to acclimate for 15 minutes at the new stretch ratio. Each test was repeated three times [137,138].

2.3.3 Zero Stress State

A radial, stress-relieving cut was made into 1 mm thick ring sections taken from the middle region of each vessel following mechanical testing [120]. This radial cut causes ring sections to spring open into a sector. After allowing 30 minutes in PBS for each vessel to equilibrate, a digital image was taken of the resultant open sector using a Nikon Coolpix s3500 (resolution of 20 μm/pixel). Image-Pro 6.0 image analysis software was used to measure the sector thickness H, inner arc length L_i, and outer arc length L_o. From these data, cross-sectional area A and opening angle Φ of the sector were calculated using

$$H = \frac{2A}{L_i + L_o} \text{ and } \Phi = \pi - \frac{L_o - L_i}{2H} \quad . \qquad [2.1]$$

Collectively, these data enable quantification of the zero stress state for each sample.

2.3.4 Data Analysis

Vessels are assumed to be 3-D thick-walled cylindrical tubes that experience an axisymmetric finite elastic deformation under applied pressure and longitudinal extension. Neglecting the contribution of vascular smooth muscle cells, the passive mechanical properties of vessels depend predominantly on the properties, amount, and spatial arrangement of collagen and elastin in the vessel wall. Through mechanical testing, sample luminal pressure P and axial stretch λ_z were controlled, and response data for the deformed outer radius r_o and axial force F were recorded. Under the assumption of tissue incompressibility, the deformed inner radius r_i is calculated as:

$$r_i = \sqrt{r_o^2 - \frac{A}{\pi \lambda_z}} \quad . \qquad [2.2]$$

Likewise, the lumen area compliance is calculated as:

$$c = \pi \frac{\Delta r_i^2}{\Delta P} \quad . \qquad [2.3]$$

The average circumferential σ_θ and axial σ_z wall stresses are calculated as:

$$\sigma_\theta = \frac{P r_i}{r_o - r_i} \quad , \quad \sigma_z = \frac{F}{\pi \left(r_o^2 - r_i^2 \right)} \quad . \qquad [2.4]$$

The mid-wall circumferential λ_θ and axial λ_z stretch ratios provide wall strain measures, and are calculated as:

$$\lambda_\theta = \frac{2\pi\left(r_i + r_o\right)}{L_i + L_o}, \quad \lambda_z = \frac{l}{L} \quad , \qquad [2.5]$$

where l and L are the deformed and undeformed vessel lengths, respectively.

2.3.5 Theoretical Framework

For inflation and extension of an axisymmetric tube, its deformation is characterized by the right Cauchy-Green strain tensor

$$[C] = diag\left\{\left(\frac{dr}{dR}\right)^2, \left(\chi\frac{r}{R}\right)^2, \lambda_z^2\right\}, \quad \chi = \frac{\pi}{\pi - \Phi} \quad , \qquad [2.6]$$

where r and R are the radial coordinates of an arbitrary point within the vessel wall before and after deformation.

Due to the incompressibility of the vessel wall

$$\frac{dr}{dR}\frac{r}{R}\chi\lambda_z = 1 \quad , \qquad [2.7]$$

which after integration yields

$$r = \sqrt{r_o^2 - \frac{1}{\chi\lambda_z}\left(R_o^2 - R^2\right)} \quad . \qquad [2.8]$$

Given the zero-stress configuration, axial stretch ratio, and the deformed outer radius, the components of the strain tensor can be completely described. A diagrammatic representation of the zero-stress state and deformed configurations can be found in Zhou et al. (2013) and is consistent with that of other researchers (e.g., Matsumoto and Hayashi (1996)) [43,138].

We use an analytical form of the strain energy function, whereby stress and stretch are related by the energy stored in the vessel wall as it is distended [29,139]. This strain energy function was first described by Holzapfel and colleagues [5,8]:

$$W = \phi_e b_0 \left[\left(\lambda_\theta^2 + \lambda_z^2 + \left(\lambda_\theta \lambda_z \right)^{-2} \right) - 3 \right] + \frac{\phi_c}{4} \sum_{k=1-4} \frac{b_{k1}}{2b_{k2}} \left\{ \exp\left[b_{k2} \left(\sqrt{\lambda_\theta^2 \sin^2 \alpha_k + \lambda_z^2 \cos^2 \alpha_k}^{\,2} - 1 \right)^2 \right] - 1 \right\} \quad [2.9]$$

The constitutive model of equation [2.9] is a microstructural motivated strain-energy function. The first collection of terms and material constant b_0 describe the isotropic, neo-Hookean contribution of an elastin-dominated, non-collagenous extracellular matrix [5,140–142]. The second term describes the anisotropic contribution of four collagen fiber families, where subscript k denotes a particular family of fibers oriented at a mean angle of α_k with respect to the longitudinal axis with material constants b_{k1} and b_{k2}. As shown, the four-fiber family model with 8 independent parameters gives an excellent representation of biaxial mechanical data without being over parameterized [143]. In this model, the contributions of passive smooth muscle cells to the overall mechanics have been neglected. Considering the circumferential or diagonally oriented smooth muscle cell orientation [144], the effect is difficult to isolate from the dominant anisotropic collagenous structure [145]. In this model $\alpha_1 = 90$ deg represents circumferentially oriented fibers, and $\alpha_2 = 0$ deg represents axially oriented fibers. Additionally, $\alpha_3 = -\alpha_4 = \alpha$ represents diagonally oriented fibers, with the value for α obtained from the model. Accordingly, the stress-like and dimensionless parameters for these fiber families are equivalent so that $b_{31} = b_{41}$ and $b_{32} = b_{42}$ respectively. ϕ is the area fraction of (e) elastin or (c) collagen compared to the total tissue as determined through histological analysis.

Any deformed configuration characterized by the deformed outer radius and axial stretch ratio is realized by imposing pressure, and axial force, from a given inner arc length,

outer arc length, and opening angle in the zero-stress state and strain energy function W so that

$$P = \int_{r_i}^{r_o} \lambda_\theta \frac{\partial W}{\partial \lambda_\theta} \frac{dr}{r} \quad , \quad F = \pi \int_{r_i}^{r_o} \left(2\lambda_z \frac{\partial W}{\partial \lambda_z} - \lambda_\theta \frac{\partial W}{\partial \lambda_\theta} \right) r dr \, . \qquad [2.10]$$

Using data obtained through our mechanical testing and zero-stress state measurements, the material constants of the constitutive model were found for each vessel. The material parameters associated with the constitutive model were determined via non-linear regression of equation [2.10] which was implemented in Matlab 2010b (Mathworks. Inc) using the lsqnonlin subroutine. The lower and upper limits of the parameters were prescribed as b_0 and $b_{k1} \in [0, 105]$, $b_{k2} \in [0, 10]$, and $\alpha \in [0°, 90°]$. The constitutive model was then used to predict the deformed configurations, stretch ratios, and average transmural stresses under prescribed, in situ and coronary, loading conditions.

The in situ and grafted loads include both transmural pressure and axial force. The value of in situ pressure for the LAD, ITA, RA, GSV, and LSV was taken from the literature (Table 2.3) and represents a rough estimate of the mean value throughout the cardiac cycle [83,126,127,129]. For example, a pressure of 100 mmHg was selected as a loading condition for the LAD. In situ force, on the other hand, was determined as a result of biaxial testing. The grafted coronary loads for the ITA, RA, GSV, and LSV were the values of the pressure and axial force of the LAD.

2.3.6 Histological Analysis

Upon completion of mechanical testing, sections of each vessel were fixed in 4% fresh paraformaldehyde, followed by embedding in paraffin wax. Sections approximately 5 μm thick were stained with a combination of Verhoeff's elastic and Masson's trichrome stain

[146]. All vessels were sectioned and stained together to prevent batch-to-batch variations. Images were obtained using a Nikon E600 microscope with CCD camera and computer interface with Q Capture (QImaging). Each tested tissue was imaged at 4-6 different locations and the best representative image was selected for each tissue to be used for thresholding analysis. Mean and standard deviations for each group were therefore found from a sample size of n=6. Area fractions occupied by black, blue, and red pixels were quantified using ImageJ software (NIH) with the "Threshold_Colour" plugin, which serves to estimate fractions of elastin, collagen, and smooth muscle in each vessel, respectively [147]. In an effort to maintain consistency across samples, unstained pixels were not considered, and threshold values were fixed. Black pixels were quantified using a bandpass filter from Brightness 0 – 83; blue pixels were quantified using a bandpass filter from Brightness 83 – 255 and Hue 33 – 230; and red pixels were quantified using a bandpass filter from Brightness 83 – 255 and bandstop filter from Hue 33 – 230. Thus, the sum of these areas was approximately 100% for each sample, and the contribution of other constituents (e.g., ground substance) was assumed to be negligible.

2.3.7 Comparison of Native and Grafted States

The normalized difference between each vessel (i.e., ITA, RA, GSV, LSV) in situ (IS) and the left anterior descending artery (LAD) in situ for inner radius, compliance, circumferential stress, and axial stress are described by

$$\Xi_{ri} = \frac{2\left|r_i^{IS} - r_i^{LAD}\right|}{r_i^{IS} + r_i^{LAD}}\ ,\ \Xi_c = \frac{2\left|c^{IS} - c^{LAD}\right|}{c^{IS} + c^{LAD}}\ ,\ \Xi_{\sigma\theta} = \frac{2\left|\sigma_\theta^{IS} - \sigma_\theta^{LAD}\right|}{\sigma_\theta^{IS} + \sigma_\theta^{LAD}}\ ,\ \Xi_{\sigma z} = \frac{2\left|\sigma_z^{IS} - \sigma_z^{LAD}\right|}{\sigma_z^{IS} + \sigma_z^{LAD}}\ . \quad [2.11]$$

Likewise, the normalized difference between (IS) and that same vessel used as a replacement graft for the LAD for end-to-end anastomosis under coronary loading conditions (G) is calculated in a similar manner to [2.11] by

$$\Omega_{ri} = \frac{2\left|r_i^{IS} - r_i^{G}\right|}{r_i^{IS} + r_i^{G}},\ \Omega_{c} = \frac{2\left|c^{IS} - c^{G}\right|}{c^{IS} + c^{G}},\ \Omega_{\sigma\theta} = \frac{2\left|\sigma_\theta^{IS} - \sigma_\theta^{G}\right|}{\sigma_\theta^{IS} + \sigma_\theta^{G}},\ \Omega_{\sigma z} = \frac{2\left|\sigma_z^{IS} - \sigma_z^{G}\right|}{\sigma_z^{IS} + \sigma_z^{G}}. \quad [2.12]$$

Summing the above expressions generates three overall mechanical remodeling utility scores

$$\Xi = \Xi_{ri} + \Xi_{c} + \Xi_{\sigma\theta} + \Xi_{\sigma z} \text{ and } \Omega = \Omega_{ri} + \Omega_{c} + \Omega_{\sigma\theta} + \Omega_{\sigma z}. \quad [2.13]$$

Here values closest to zero indicate the smallest differences.

2.3.8 Statistics

Statistical analysis was performed with a two-tailed paired *t*-test and one-way or two-way ANOVA using GraphPad Prism 3.02 (San Diego, CA, USA). Dunnet's post-hoc test was used for multiple comparisons to the control. Statistical significance was taken at a level of $p < 0.05$.

2.4 RESULTS

2.4.1 Blood Vessel Histology

The microstructure of the vessels used in our comparative analysis varies considerably in spatial organization between anatomical locations, a feature reflective of its functional and native environment (Figure 2.2, Figure 2.3). Of note, the proximal LAD (Figure 2.2A) and ITA (Figure 2.2C) show numerous circumferentially oriented elastic lamellae in the media, whereas elastin is only somewhat evident in the media of the distal LAD (Figure 2.2B). Elastin is present exclusively as internal and external elastic laminas in each of the RA, GSV, and LSV vessels (Figure 2.2D, E, and F, respectively). Despite

these apparent differences, the only statistical significance in overall elastin content of any graft vessel and the LAD (ϕ_e=0.14 ± 0.12) was for the ITA (ϕ_e=0.30 ± 0.08) (Figure 2.3) while the collagen and smooth muscle fractions of the RA (ϕ_c=0.15 ± 0.07; ϕ_{smc}=0.80 ± 0.10) and GSV (ϕ_c=0.18 ± 0.08; ϕ_{smc}=0.74 ± 0.08), were found to be statistically different than the LAD (ϕ_c=0.34 ± 0.06; ϕ_{smc}=0.52 ± 0.06).

2.4.2 Zero Stress State and Material Parameters

Table 2.1 shows the measurements obtained for the stress-free configuration of each vessel following biaxial testing. In the nearly zero stress state, the opening angle, responsible for homogenizing the circumferential stress through the vessel wall, was not found to be statistically different for any of the potential graft vessels and the LAD. There was however, statistical significance between the stress-free wall thickness of the ITA (H = 0.55 ± 0.06 mm) and LAD (H = 0.88 ± 0.11 mm). The RA and GSV were also found to be different from the LAD in terms of both inner (LAD = 10.4 ± 1.45; RA = 4.65 ± 1.21; GSV = 6.06 ± 1.74 mm) and outer (LAD = 13.8 ± 1.53; RA = 8.70 ± 1.63; GSV = 9.84 ± 2.32 mm) arc lengths. Based on these biaxial testing data and stress-free measurements, the material parameters for the constitutive model were calculated and are shown in Table 2.2. Parameter b_{11}, representing the stress-like parameter in the exponential form for circumferentially oriented fibers, is significantly lower for the LSV than other vessels. Parameter b_{21} is significantly different between the RA and LAD; this represents the stress-like parameter in exponential form for axially oriented fibers. The parameter for diagonally oriented fibers – b_{31} – is significantly different between the RA and LAD.

2.4.3 In Situ Structural and Mechanical Values

A representative sample of the measured pressure-inner radius relationship at in situ conditions for each vessel shows similar behavior amongst the ITA, RA, GSV, and LSV (Figure 2.4A) while the LAD has a consistently larger lumen radius than the potential graft vessels. The GSV (r_i^{IS}=0.70 ± 0.39 mm) and LSV (r_i^{IS}=1.54 ± 0.73 mm) in situ radii (Table 2.3) were found to be different from the LAD (r_i^{IS}=2.29 ± 0.38 mm). In situ area compliance can be interpreted from the tangential slope of Figure 2.4A and is shown in Table 2.3. Compliance values however, were not found to have statistical significance. When comparing the axial force-axial distension at in situ pressures, the LAD fell within the group of tested blood vessels (Figure 2.4B) and the only statistically different in situ axial force from the LAD (F^{IS} =0.4 ± 0.12 N) was the LSV (F^{IS} =0.16± 0.09 N). The in situ circumferential stretches were statistically significant between the GSV (λ_θ^{IS} =0.93± 0.09) and LSV (λ_θ^{IS} =1.12± 0.14) compared to the LAD (λ_θ^{IS} =1.31 ± 0.26) while axial stretches were not.

When circumferential stress-stretch is plotted (Figure 2.4C) an overall increasingly stiffer behavior is demonstrated at higher stretches especially for the ITA and LAD. Note that all data in Figure 2.4C is shown at the in situ axial stretch which is measured from the unloaded state therefore axial stretches less than 1 are possible. Dramatic differences in the in situ circumferential stresses were observed for the RA (σ_θ^{IS} =14.3± 3.1 kPa), GSV (σ_θ^{IS} =3.66± 0.67 kPa), and LSV (σ_θ^{IS} =7.40± 3.36 kPa) compared to the LAD (σ_θ^{IS} =66.7 ± 39.3 kPa). The in situ axial stresses are much closer amongst the tissues than the

circumferential stresses and were only statistical significance for the LSV (σ_z^{IS} =28.6 ± 24.5 kPa) compared to the LAD (σ_z^{IS} =51.3 ± 10.4 kPa) (Figure 2.4D; Table 2.3). Collectively, the differences in structural and mechanical properties were normalized and plotted for all vessels at in situ states compared to the LAD as indicated by Ξ in Figure 2.5. Using this approach, the ITA (Ξ =0.90 ± 0.34) is the best overall match to the LAD followed by the RA (Ξ =3.61 ± 0.44), LSV (Ξ =3.84 ± 0.69), and GSV (Ξ =4.44 ± 1.47).

2.4.4 Grafted Structural and Mechanical Values

Using a uniform prescribed mean pressure of 100 mmHg and the axial force measured for the LAD of 0.4 N to approximate coronary loading conditions for the graft tissue, deformed inner radius and compliance, circumferential stress and axial stress were calculated for the graft conditions of the coronary environment (Table 2.3). When comparing an autograft tissue in its in situ environment to that of the coronary environment we found statistical significance for the inner radius of the RA (r_i^{IS}=0.9 ± 0.15; r_i^{G}=0.92 ± 0.12 mm), GSV (r_i^{IS}=0.70 ± 0.39; r_i^{G}=1.10 ± 0.28 mm) and LSV (r_i^{IS}=1.54 ± 0.73; r_i^{G} =1.91± 0.67 mm). The LSV (c^{IS}=0.89 ± 0.61; c^{G}=0.23 ± 0.04 10^{-6}m^2/kPa) also had a significant change in compliance. Despite the apparent increases in grafted axial stress shown in Table 2.3, statistical significance was only found in the circumferential direction. Specifically, the RA (σ_θ^{IS} =14.3 ± 3.1; σ_θ^{G} =17.2 ± 4.00 kPa), GSV (σ_θ^{IS} =3.66 ± 0.67; σ_θ^{G} = 22.8 ± 5.71 kPa), and LSV (σ_θ^{IS} =7.40 ± 3.36; σ_θ^{G} = 49.4 ± 15.1 kPa) all experience increased circumferential stress. The overall differences in structural and mechanical properties were normalized and plotted for all vessels at in situ states compared to the grafted environment as indicated by Ω in Figure 2.5. Using this approach, the ITA (Ω=0.28

± 0.20) is the best overall match to the LAD followed by the RA (Ω=1.00 ± 0.20), GSV (Ω=3.66 ± 1.19), and LSV (Ω=3.74 ± 0.62).

2.5 DISCUSSION

Landmark clinical studies have identified the existence of a performance differential for autologous vascular grafts based on anatomical tissue source location [12,13,107,113,116,133,135,148–150]. Although clinical outcomes are inarguably the key determinant for CABG graft selection, the mechanisms of differential performance are not well explicated. Our data, and that of classic literature, shows that vascular tissues from functionally different origins have unique histoarchitecture [151]. This histoarchitecture determines the inherent mechanical behavior dictating how a tissue responds to the altered loading environment of the coronary vasculature (Figure 2.4). While remodeling is nominally an adaptive process that restores homeostasis, the mechanical, compositional, and geometrical incongruities between the grafted and adjacent tissues can lead to deleterious outcomes that compromise lumen patency. In fact, a plot of the normalized difference in mechanical properties metrics – Ω and Ξ – versus first year CABG failure rate (Figure 2.6) suggests a positive relationship between graft failure rate and mechanical deviations. Further, our important findings suggest that a range of unique mechanical conditions exist for each of these tissues in situ and for their graft environment. Collectively, this information will help guide surgeons towards optimal tissue sources for bypass grafting, some of which are yet to be realized, and provide a basis for alternate therapeutic approaches such as tissue engineering [14,112].

2.5.1 Structural and Mechanical Parameters and Vessel Selection

Although a multitude of logistical and practical criteria are used for surgical CABG vessel selection, matched inner radii in the in situ state has provided a historical foundation to initiate candidate vessels for transplantation. This fortunate selection criterion conveniently provides a common basis for comparison between grafts in situ and can be easily assessed using ultrasound. Under the increased pressure loading of the grafted environment however, the inner radii are modified from their in situ condition and is most evident for the GSV that experiences an increase in radius from 0.70 ± 0.39 to 1.10 ± 0.28 mm as indicated by $\Omega = 0.54 \pm 0.44$. These subtle differences may have a dramatic effect on wall shear stress, a known stimulus for remolding and intimal hyperplasia of venous grafts [42]. For instance, shear stress τ_w under steady Poiseuille flow has an exponential dependence on inner radius so that

$$\tau_w = \frac{4\mu Q}{\pi r_i^3}, \qquad [2.14]$$

where Q is the mean volumetric flow rate and μ the dynamic viscosity of blood [2]. It should be noted that the GSV graft will also experience an increase in Q upon implantation from roughly 0.14 ml/s in the greater saphenous vein environment to 0.52 ml/s in the coronary vasculature making the wall shear stress change less dramatic [3,31]. Whereas comparable radii are important regulators of steady perfusion and shear stress, the pulsatile perfusion environment is dependent upon vascular compliance. Compliance is a contributing factor for anastomotic intimal hyperplasia, and the change in compliance from the in situ to the grafted environment is indicative of the nonlinear pressure-radius relationship [152]. The latter emphasizes the importance of accurate structure-based strain energy function as presented in [2.9]. It is not surprising that the ITA has a similar

compliance to that of the LAD considering their comparable microstructure and physiologic loading conditions.

Through mechanotransductive pathways intramural stresses apply physical signals to resident vascular cells [122]. The stress distribution throughout the wall of the blood vessel also has important implications in health and disease with large opening angles shifting the circumferential stress distribution from the intima towards the adventitia [153]. Veselý et al., (2015) found that the optimal opening angle in the human great saphenous vein for uniform stress distribution is around 40 degrees [154]. In smaller pig studies than ours the opening angles were found to be considerably higher than our study [155]. This phenomenon does depend on the species and likely other taxonomic ranks [156]. Overall, we did not find statistical significance between opening angles of our tissues. It is surprising, however, to see that the magnitude of mean circumferential stress differed so dramatically between graft tissues in situ and that the RA, GSV, and LSV had much higher stresses in the axial direction. Although the passive state of the smooth muscle cells contributes to a lower in situ stress than would be achieved with basal tone, an 18-fold difference exists between GSV (3.66 ± 0.67 kPa) and ITA (67.1 ± 14.7 kPa) so that Ξ=1.79 ± 0.04. The veins would also experience the greatest increase in circumferential stress upon grafting (GSV = 18.9 kPa, Ω = 1.44 ± 0.08; LSV = 42.0 kPa, Ω = 1.49 ± 0.09). In situ and grafted saphenous vein circumferential stresses (σ_θ^{IS} =3.66± 0.67; $\sigma_\theta^{G} \approx 22.8 \pm 5.71$ kPa), were close to the mean values of the human counterpart at a 40 degree fiber angle ($\sigma_\theta^{IS} \approx 6$; $\sigma_\theta^{G} \approx 22$ kPa) [154]. Enigmatically, the axial stresses were much higher than circumferential stresses which is known to play a fundamental role in compensatory adaptation by blood vessels [32]. Since axial prestretch is reduced with aging and disease

conditions, our tissue, taken from mature but young pigs, is likely at a higher stretch than those used for grafting [32,154]. A likely contributing factor is the somatic growth and axial extension during development of these source tissues (i.e., extremities of the leg and arm). Moreover, the tested invariant force-pressure relationship that holds for arteries may need to be evaluated more extensively for venous structures [136]. It is interesting enforcing volume preservation and axial extension could be used to decrease inner radius and increase compliance and circumferential stress. While application of axial distension to CABGs might increase the difficulty of the procedures and put stress on the suture interface, it is worth further examination if it has the potential to reduce the incidence of graft failure in the vessels.

2.5.2 Framework for Evaluation of Candidate Vessels and Clinical Significance

In this work we have initiated two competing hypotheses that underlie the mechanical analysis of vessels used for the CABG procedure that likely contribute to differential outcomes: 1) Ξ, a comparison of a graft vessel in situ to the LAD in situ, or 2) Ω, comparisons of a graft vessel in situ to that same vessel under conditions of the LAD. The latter presents a uniform loading condition to facilitate comparisons between these unique tissues. These subtle distinctions could have profound effects on how graft vessels are evaluated for candidacy in the future. Using both approaches the ITA was found to be the best mechanical choice followed by the RA. The results are less clear however, for the GSV and LSV raising the question, is it better for a graft to be more like the coronary artery ($\Xi \rightarrow 0$) or more like its native condition ($\Omega \rightarrow 0$)? Unfortunately, the question does not have an immediate and clear answer. For example, it is tempting to assign a linear relationship to Figure 2.6 yet these clinical observations are limited to only three data points and could

also be fit to an exponential or polynomial, whereby the behavior of that nonlinear fit for Ξ and Ω would appear to be reversed. We do know however, that the normalized contribution of each of the individual parameters that make up Ξ (i.e., Ξ_{ri}, Ξ_{c}, $\Xi_{\sigma\theta}$, $\Xi_{\sigma z}$), is more evenly distributed than Ω where $\Omega_{\sigma\theta}$ and $\Omega_{\sigma z}$ contribute to 62-86% of the overall value. It is also provocative to consider a case where both Ξ and Ω intersect the origin in Figure 2.6. This would represent an idealized scenario where the coronary artery is used as a CABG graft resulting in zero first year failures. This is an unlikely, if not impossible scenario since the underlying cause of clinical failures are not isolated to mechanical reasons, yet it may provide insight into the importance of these two metrics. The high slopes of the linear fits used in Figure 2.6 suggest inner radius and axial stress as major contributors to clinical failure rates. The latter observation is profound since surgical guidelines for the CABG procedure recommend against applying axial loads. The answer to these questions and more will undoubtedly improve as clinical reports for other vessels (*e.g.,* gastroepiploic or inferior epigastric artery) becomes available and are matched to mechanical data.

An important distinction between our in vitro study that considers vessels as replacement tissues for the LAD and the actual CABG procedure lies in how axial loads are applied. Current surgical guidelines for the CABG procedure advise against using excessive graft lengths to prevent kinking while tensile forces should be minimized to improve suture retention [132]. This configuration puts vessels into neutral axial loading prior to reperfusion. Upon reperfusion however, small axial forces will be generated and can lead to bending and buckling. Still these stresses are far lower than those observed in situ resulting in a transplantation stress difference (Table 2.3). Khonsari points out

"Saphenous vein grafts tend to shrink over time … shrinkage may cause tension on the anastomosis and predispose the graft to premature failure." This observation is indicative of our stress-mediated growth and remodeling hypothesis described in the introduction aimed at restoration of in situ axial stresses. Regardless, the analysis described herein simplifies a complicated clinical procedure that involves bending and buckling instabilities that do not lend well to analytical approaches implemented within the framework of continuum mechanics.

In future investigations, the methods described here will be utilized in conjunction with a perfusion bioreactor to evaluate and control the vascular remodeling process and determine the dominance of the utility scores Ξ or Ω. Many theoretical studies have been proposed using stress-based growth and remodeling process for CABG for venous grafts and the current study has established the initial conditions for those future investigations which will determine the adaptability of the candidate tissues to new environments [157,158]. We hypothesize that adaptability is dependent upon cellular function and the current state of the extra cellular matrix. In these future investigations, the grafted conditions applied by the *ex vivo* culture device will provide a prolonged remodeling stimulus, which we expect will lead to growth and remodeling within the cultured vessels. However, it is not clear whether vessels will continue to seek their initial homeostatic stress state indefinitely, take on a stress objective of a coronary artery, or a hybrid of both conditions. Furthermore, we will utilize a predictive mathematical approach of the remodeling required to regain homeostasis and compare to experimental vascular cultures.

While this investigation is focused on analyzing autologous CABG vessels, the outlined procedure is a universal approach that could be applied to other non-coronary

grafting such as treatments for peripheral vascular disease. Beyond autologous grafts, the above methodology can give a more rigorous mechanical analysis of tissue engineered blood vessels (TEBVs) than is commonly presented. Generally, the mechanical data presented for TEBVs include uniaxial tensile tests, burst pressure, suture retention strength, and compliance, but these metrics do little to describe the functionality of the vessels *in vivo* [126,159,160]. Although the conditions most conducive to tissue growth will need to be identified, utilization of the current methods for mature vascular grafts could aid researchers in developing more functional TEBVs with quiescent properties [161]. If the aforementioned grafts are to be used for grafting applications such as CABG where mechanical compatibility is paramount, it will be important to elucidate how the vessels develop a homeostatic state as it is influenced by biaxial loading. Moreover, *ex vivo* investigations under controlled mechanical stimuli could potentially allow researchers to define the homeostatic stress state for TEBVs. This would facilitate the creation of artificial grafts compatible with any mechanical loading conditions and thus any anatomical location.

2.5.3 Limitations

We hold that this investigation represents a meaningful contribution to the collective knowledge of vascular mechanics, but we acknowledge that there are limitations to the study that merit further consideration. First and foremost, we assume that uniform loading of the grafted replacement vessels is equivalent to that of a native LAD artery. This implies that we are considering an end-to-end anastomosed graft replacing a section of the LAD rather than following the surgical guidelines for a CABG procedure. Furthermore, grafted conditions were assumed to be 100 mmHg at an axial force of 0.4 N, approximately

representing the mean values experienced by the LAD. This does not account for the constant variation in stresses and strains caused by hemodynamic pulsatility and contraction of the myocardium. We also point out that all vessels were harvested taken from healthy, young pigs and that these vessels which would likely experience altered mechanics in disease and aging [162,163].

Of further note, histological differences exist between the proximal (Figure 2.2A) and distal (Figure 2.2B) sections of the LAD coronary artery due to the significant structural variations along its length. Based on our previous assumption of vessels organizing to homogenize stress at their homeostatic state, this change in histology would indicate that the loading environment changes significantly along the length of the LAD. As such, the optimal structure of a CABG graft of the LAD would vary according to where along its length it is being grafted. Moreover, the peripheral vessels of a quadraped are a less direct analogy to the human than the coronary vessels. Nowhere is this truer than for the LSV, a tissue that does not exist in the human but has applicability in veterinary medicine and laboratory studies (Figure 2.1). Moreover, the zero-stress state measurements were performed following mechanical testing therefor the supra-physiological loading conditions could potentially have an effect on opening angle measurements. This is likely a small contribution but one that should be considered in future work. Lastly, this investigation focused on the passive mechanics of the potential graft tissue. In highly muscular blood vessels such as the RA, GSV, or LSV, the stress state depends on smooth muscle activation and likely contributes to the low native circumferential stress values predicted in Table 2.3. An additional term could be added to account for active smooth muscle behavior [144,164].

2.6 CONCLUSION

Mechanical loading is an important factor driving vascular growth and remodeling in autologous grafting of mature blood vessels. Differences in structural and mechanical characteristics, as demonstrated by our novel metrics Ξ and Ω, provide a reference to the extent that remodeling must occur in the grafted environment and provides supportive evidence for the differential performance of CABG grafts. The results of the current study are consistent with vessel-specific variations in clinical success rates and provides the groundwork for engineering a better CABG graft. Further investigation and experimentation is necessary to determine if these metrics can be manipulated, acutely or chronically on native tissues, to improve CABG outcomes.

2.7 ACKNOWLEDGEMENTS

The authors would like to acknowledge the imaging and histological assistance of Dr. Robert Price and Benny Davidson, dissection assistance of Brooks Lane and Carissa Leischner, image collection and processing assistance of Liam McNamara, and Caughman's Meat'n Place.

2.8 FUNDING

This research was supported by NIH INBRE grant for South Carolina (P20GM103499) and through a provost sponsored graduate scholarship from BMEN.

2.9 TABLES

Table 2.1 Vessel geometry of stress-free configuration.

	Outer arc-length (L_o) [mm]	Inner arc-length (L_i) [mm]	Opening angle (Φ) [°]	Stress-Free Thickness (H) [mm]
LAD	13.8 ± 1.53	10.4 ± 1.45	70.1 ± 12.5	0.88 ± 0.11
ITA	13.4 ± 0.9	10.8 ± 0.86	44.9 ± 18.2	0.55 ± 0.06*
RA	8.70 ± 1.63*	4.65 ± 1.21*	45.2 ± 26.4	0.87 ± 0.06
GSV	9.84± 2.32*	6.06 ± 1.74*	51.5 ± 25.0	0.84 ± 0.05
LSV	12.0 ± 4.26	8.65 ± 4.35	67.8 ± 22.2	0.87 ± 0.15

Table 2.2 – Material Parameters for LAD, ITA, RA, GSV, and LSV obtained for a four-fiber constitutive model.

	b_0 [kPa]	b_{11} [kPa]	b_{12}	b_{21} [kPa]	b_{22}	b_{31} [kPa]	b_{32}	α [°]	Residual
LAD	3.47 ± 2.83	18.7 ± 12.7	1.81 ± 2.92	1.96 ± 1.88	3.15 ± 2.08	7.51 ± 10.8	3.98 ± 1.4	40.5 ± 10.0	0.73 ± 0.34
ITA	17.5 ± 17.0	17.2 ± 5.74	0.34 ± 0.11	4.52 ± 3.70	3.38± 2.42	22.7± 30.6	4.05 ± 2.26	34.1 ± 13.2	0.52 ± 0.15
RA	5.17 ± 8.16	7.98 ± 11.3	0.64 ± 0.78	17.8± 10.8*	4.19 ± 2.02	17.8± 27.6*	3.73 ± 2.82	35.3 ± 4.98	0.52 ± 0.12
GSV	4.40 ± 5.85	6.95 ± 4.98	1.75 ± 2.93	14.0 ± 10.6	3.93± 3.16	24.5 ± 33.6	4.46 ± 2.55	37.7 ± 14.3	0.74 ± 0.23
LSV	5.53 ± 8.25	4.75± 4.03*	0.63 ± 0.62	0.91 ± 1.31	2.83± 3.09	2.62 ± 3.23	4.02 ± 2.97	42 ± 14.91	0.43 ± 0.23

Table 2.3 – Loads, structure, stretch, and stress for the LAD, ITA, RA, GSV, and LSV in situ or grafted under coronary loads.

	P (mmHg)	F (N)	r_i (mm)	c (10^{-6}m^2/kPa)	λ_θ	λ_z	σ_θ (kPa)	σ_z (kPa)
LAD	100	0.4 ± 0.12	2.29 ± 0.38	0.32 ± 0.11	1.31 ± 0.26	1.33 ± 0.02	66.7 ± 39.3	51.3 ± 10.4
	In Situ Loads		**In Situ Structure**		**In Situ Stretch**		**In Situ Stress**	
ITA	100	0.35 ± 0.08	1.98 ±0.13	0.39 ± 0.13	1.17 ± 0.11	1.22 ± 0.07	67.1 ± 14.7	64.4 ± 17.2
RA	80	0.33 ± 0.21	0.9 ± 0.15	0.09 ±0.04	1.16 ± 0.23	1.17 ± 0.07	14.3± 3.12[§]	65.1 ± 34.2
GSV	20	0.26 ± 0.14	0.70± 0.39[§]	0.17 ± 0.12	0.93± 0.09[§]	1.24 ± 0.10	3.66± 0.67[§]	46.1 ± 44.7
LSV	20	0.16± 0.09[§]	1.54± 0.73[§]	0.89 ± 0.61	1.12± 0.14[§]	1.34 ± 0.17	7.40± 3.36[§]	28.6± 24.5[§]
	Grafted Loads		**Grafted Structure**		**Grafted Stretch**		**Grafted Stress**	
ITA	100	0.4	1.97 ± 0.13	0.38 ± 0.13	1.17 ± 0.11	1.24 ± 0.07	67.9 ± 15.6	75.7 ± 14.3
RA	100	0.4	0.92± 0.12[*]	0.10 ± 0.06	1.17 ± 0.17	1.21± 0.05[*]	17.2± 4.00[*]	79.3 ± 20.1
GSV	100	0.4	1.10± 0.28[*]	0.15 ± 0.05	1.12± 0.14[*]	1.25 ± 0.09	22.8± 5.71[*]	93.5 ± 39.7
LSV	100	0.4[*]	1.91± 0.67[*]	0.23± 0.04[*]	1.35 ± 0.16	1.34 ± 0.19	49.4± 15.1[*]	74.2 ± 24.7

2.10 FIGURES

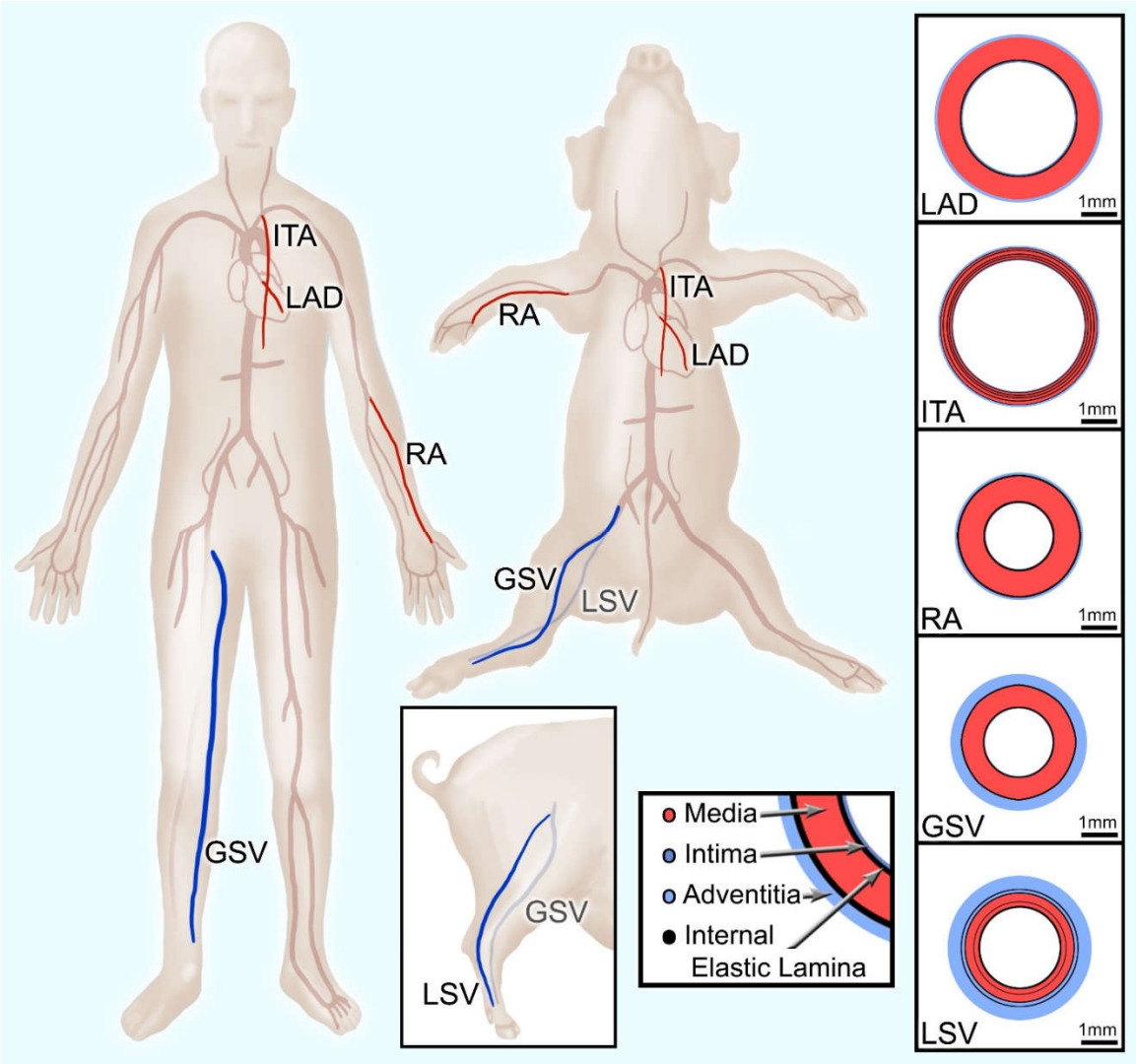

Figure 2.1 – Translational schematic comparing vessel locations in human and porcine anatomy and vessel wall diagrams to scale based on geometric and histological data from study.

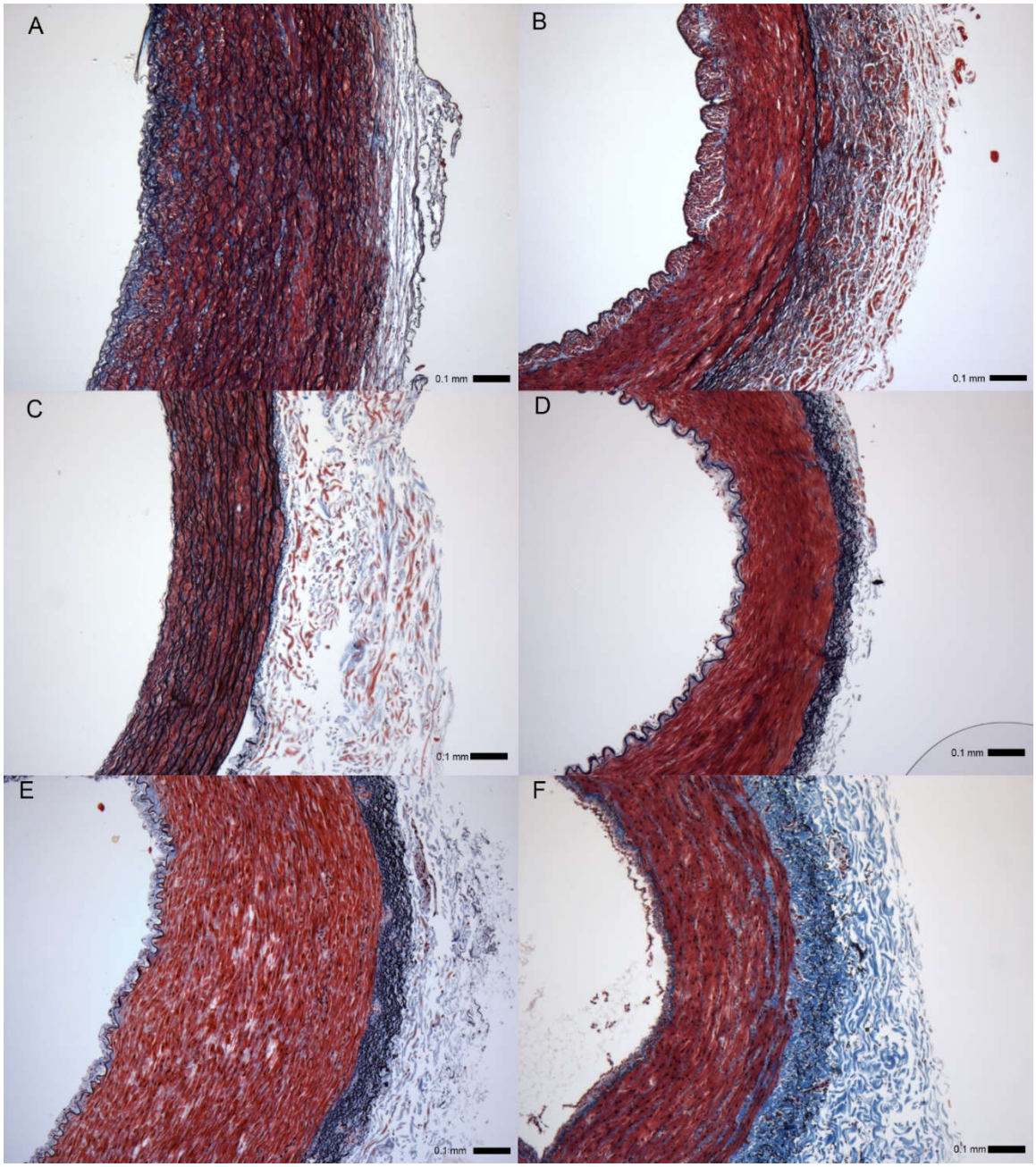

Figure 2.2 – Verhoeff-Masson's stained cross-sections of (A) proximal and (B) distal left anterior descending artery - LAD approximately 2 cm apart; (C) internal thoracic artery - ITA, (D) radial artery - RA, (E) great saphenous vein - GSV, and (F) lateral saphenous vein - LSV.

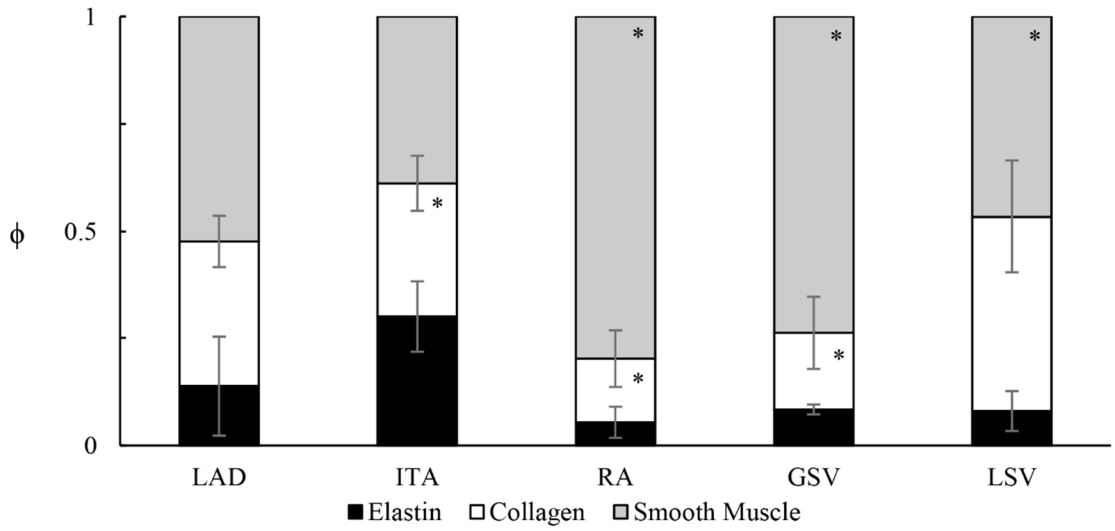

Figure 2.3 – Area fractions ϕ of elastin (black), collagen (white), and smooth muscle (gray) determined by thresholding analysis of Verhoeff – Masson's stained cross-sections for the ITA, RA, GSV, and LSV.

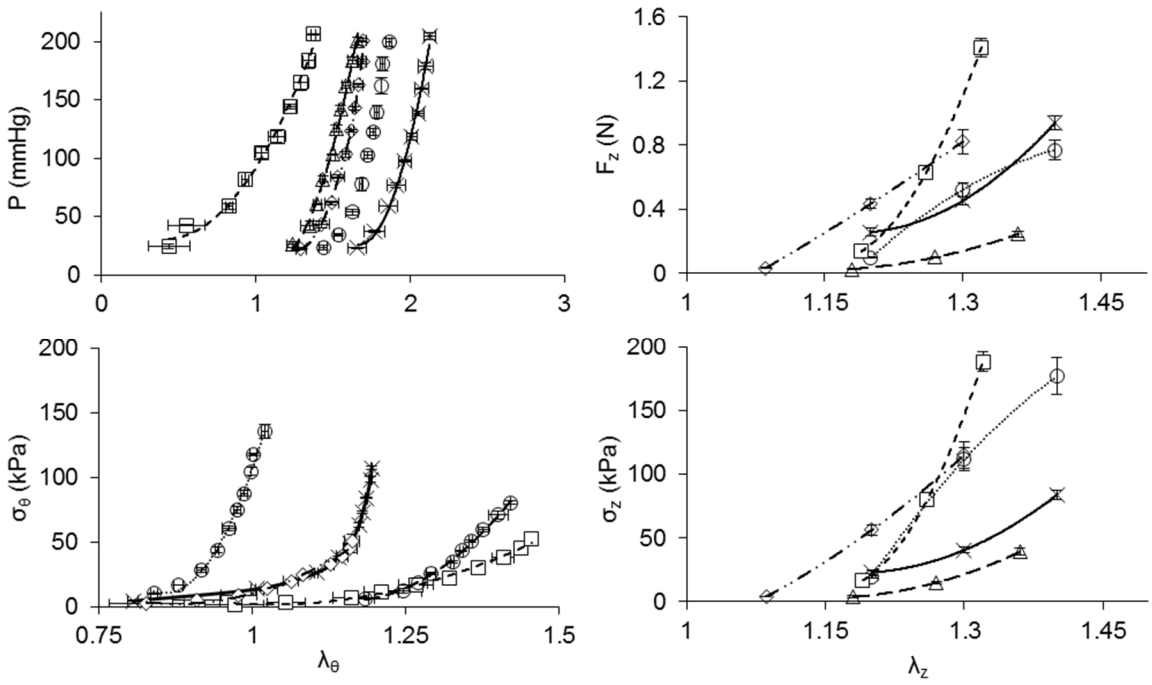

Figure 2.4 – Representative plots at in situ conditions of (A) pressure-inner radius (B), axial force-stretch, (C) circumferential stress-stretch, and (D) axial stress-stretch for the LAD (—×—), ITA (·····⊙·····), RA (- -⊡- -), GSV (- ·△· -), and LSV (—◇—).

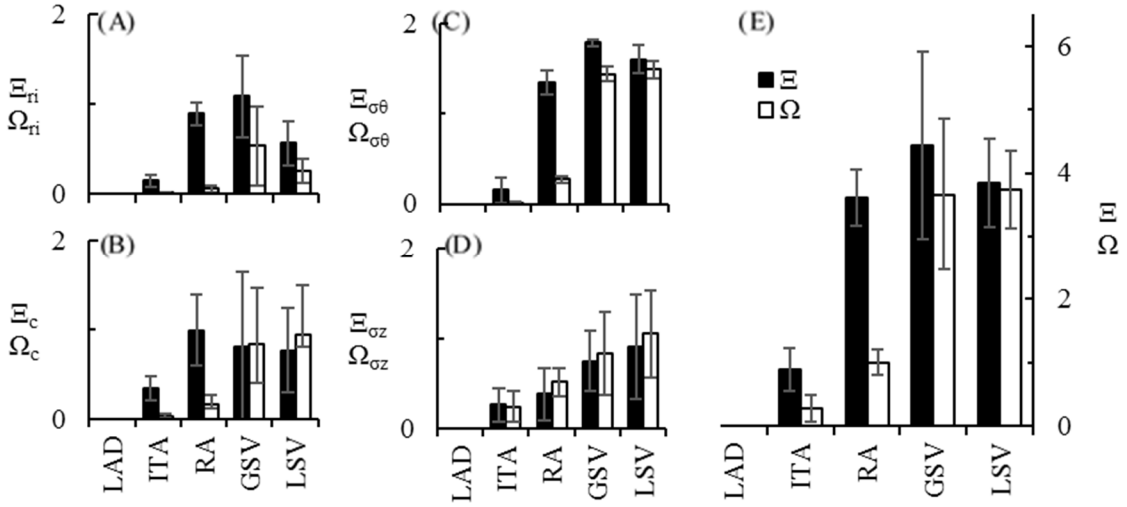

Figure 2.5 – Comparison of normalized differences between vessels (ITA, RA, GSV, or LSV) in situ and the LAD (Ξ, ■) or between vessels in situ and that vessel grafted under uniform loads of the LAD environment (Ω,□), where subscripts (ri), (c), (σθ), and (σz) represent the normalized inner radius, compliance, circumferential stress, and axial stress respectively as plotted in (A), (B), (C), and (D) respectively, while Ξ and Ω (no subscript) are the summation of those metrics (E).

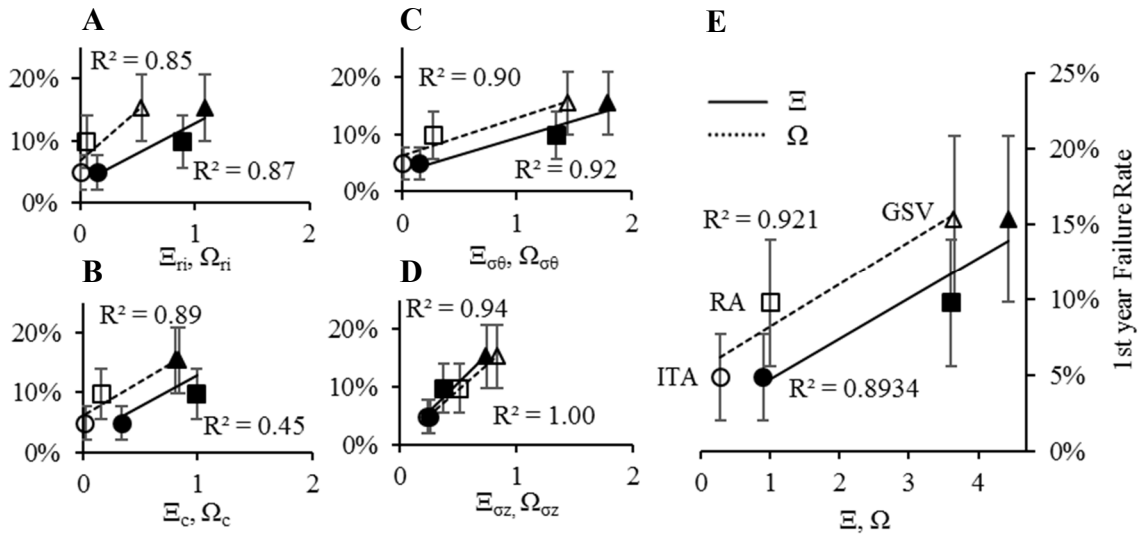

Figure 2.6 – Relationship between the first year CABG failure rate (mean ± SD) and the state of the vessels in situ compared to the LAD (Ξ dashed line: ITA ●; RA ■; GSV ▲) or between the vessels in situ and that vessel grafted under uniform loads of the LAD environment (Ω solid line: ITA ○; RA □; GSV △), where subscripts (ri), (c), (σθ), and (σz) represent the normalized inner radius, compliance, circumferential stress, and axial stress as plotted in (A), (B), (C), and (D) respectively, while Ω and Ξ (no subscript) are the summation of those metrics (E).

CHAPTER 3

PERFUSION TISSUE CULTURE INITIATES DIFFERENTIAL REMODELING OF INTERNAL THORACIC ARTERIES, RADIAL ARTERIES, AND SAPHENOUS VEINS [2]

[2]Prim, D. A., Menon, V., Hasanian, S., Carter, L., Shazly, T., Potts, J. D., & Eberth, J. F. Submitted to *Journal of Vascular Research*, 1/17/2018

3.1 ABSTRACT

Adaptive remodeling processes are essential to the maintenance and viability of coronary artery bypass grafts where clinical outcomes depend strongly on the tissue source. In this investigation, we utilized an *ex vivo* perfusion bioreactor to culture porcine analogs of common human bypass grafts: the internal thoracic artery (ITA), the radial artery (RA), and the great saphenous vein (GSV), and evaluated samples acutely (6 hours) and chronically (7 days) under *in situ* or coronary-like perfusion conditions. Although morphologically similar, primary cells harvested from ITAs illustrated lower intimal and medial, but not adventitial, cell proliferation rates compared to RAs or GSVs. Basal gene expression levels were similar between all vessels with only *COL3A1*, *SERPINE1*, *FN1* and *TGFB1* differentially expressed prior to culture; however, over half of all genes were affected nominally by the culturing process. When exposed to coronary-like conditions, RAs and GSVs experienced pathological remodeling not present in ITAs or when vessels were studied under their *in situ* conditions. Many of the remodeling genes perturbed at 6 hours were restored after 7 days (*COL3A1*, *FN1*, *MMP2*, *TIMP1*) while others (*SERPINE1*, *TGFB1*, *VCAM1*) were not. Findings elucidate potential mechanisms of graft failure and highlight strategies to encourage healthy *ex vivo* pre-graft conditioning.

3.2 INTRODUCTION

Coronary artery bypass grafts (CABGs) experience wide variations in failure rates depending on the source tissue used for the graft, with approximately 6% of 400,000 procedures per year experiencing some sort of failure in the first 12 months [11,14]. Although vascular cell activity is vital to healthy remodeling, graft failure is often the result of intimal hyperplasia, whereby a complex remodeling cascade of smooth muscle cell

(SMC) differentiation, migration, and proliferation; extracellular matrix (ECM) protein deposition; and infiltration of circulating inflammatory and progenitor cells lead to the formation of an abnormal tissue layer between the intima and internal elastic lamina. This process eventually causes graft narrowing, restenosis, and occlusion resulting in surgical reintervention [22,165,166]. An intuitive approach to improving clinical outcomes would therefore be to stimulate the inherent healthy processes in a graft tissue while attenuating maladaptive remodeling.

Throughout development, mechanosensitive vascular cells dictate the growth and organization of blood vessels in response to hemodynamic loads. The resulting mature vascular tissues are optimized with respect to their specific loading conditions [120,167,168]. While the number of CABG failures remains unacceptably high, for the majority of current CABGs to be successful one of the following must be true: (i) vessels can function effectively in loading conditions for which they may not be developmentally optimized or (ii) vessels adapt to chronic changes to their environment. Others have reported long-term compensatory changes in grafts that are successful [52,169], supporting the validity of (ii). This adaptation hypothesis assumes that vascular cells within graft vessels sense and respond to chronically altered mechanical loads, which has been theoretically accepted for decades and corroborated in a wide-range of experiments [29,32,46,47,170–173]. Separately, evidence suggests that vascular cells in discrete vessels, arising from different embryological origins, do not function uniformly and respond differently to stimuli [174,175]. Thus, it is plausible that inherent differences between CABG vessels could affect their ability to successfully adapt to grafting.

To assess remodeling capability at a reasonable time scale, we can evaluate expression of genes associated with vascular remodeling as a proxy for eventual growth and remodeling outcomes. Type III Collagen (*COL3A1* gene), for example, is associated with structural fibers contributing to the mechanical strength of the vessel wall as well as a component of the basement membranes. COL3A1 deposition and remodeling is also associated with graft restenosis and intimal hyperplasia [176,177]. Matrix metallopeptidase II (*MMP2* gene) degrades several types of collagen, and it is inhibited by tissue inhibitors of metallopeptidases (*TIMP1* gene), both of which are known to exhibit altered expression in response to blood flow and pressure; therefore, altered expression of either of these genes could be an indicator of active vascular remodeling [52,83]. Fibronectin 1 (*FN1* gene) is an ECM component that has been shown to be activated by cyclic stretch and play roles in SMC phenotype modulation, proliferation, and cell adhesion [178]. Plasminogen activator inhibitor type 1 (*SERPINE1* gene) is expressed by endothelial cells (ECs) and SMCs in response to both altered cyclic strain and flow and plays influencing fibrinolytic balance, regulates ECM proteolysis, and can inhibit matrix degradation by inhibiting MMPs [179]. Vascular cell adhesion molecule type 1 (*VCAM1* gene) is an endothelial marker that responds to flow and is implicated in inflammatory processes as a precursor to neointima formation [180]. Transforming growth factor beta 1 (*TGFB1* gene) is implicated in numerous cardiovascular processes, specifically cell growth, proliferation, differentiation, and apoptosis, and its expression has been shown to change in response to altered cyclic strain [181,182].

In this investigation, we measured and compared the early remodeling response of three common CABG tissues – the internal thoracic artery (ITA), radial artery (RA), and

great saphenous vein (GSV) – to coronary loading conditions by culturing samples in an *ex vivo* perfusion bioreactor. We hypothesized that inherent differences exist in each vessel's response to altered stimuli and thus their ability to remodel in response to CABG. Further understanding of differential remodeling can then be used to guide future investigations into graft preconditioning optimization strategies.

3.3 MATERIALS AND METHODS

3.3.1 Tissue Harvesting and Preparation

The left anterior descending coronary artery, internal thoracic artery, radial artery, and great saphenous vein samples were dissected from freshly slaughtered American Yorkshire sows (approx. 200kg, 3 years old) at a local abattoir. All tissue used in this study were acquired from animals designated for human consumption and therefore did not fall under IACUC protocol. Prior to any experimental manipulation, fresh samples (time 0, t0) were briefly rinsed in sterile Moscona's saline solution then snap frozen on dry ice. All other samples were excised then transported in tubes containing sterile Moscona's saline solution supplemented with 20 U/mL heparin, 1% penicillin/streptomycin, 1% amphotericin-B, and 1% gentamycin. Upon arrival at the laboratory, vessels were cleaned of excess perivascular and adventitial tissue, branches ligated with sterile 6-0 silk suture, and samples mounted to custom made barbed glass cannulas within custom-made lidded glass bioreactor baths (Adams & Chittenden Scientific Glass, Berkeley, CA). For 7 day experiments, tissue sections adjacent to mounted samples were fixed in 4% paraformaldehyde for later comparison to cultured samples.

3.3.2 Cell Isolation and Proliferation for Plated Studies

To isolate intimal cells, one end of each vessel was occluded with sterile 3-0 silk suture. The lumen was then filled with 0.15% w/v collagenase II solution in serum-free DMEM (Worthington Biochemical, Lakewood, NJ), followed by clamping of the open end of the vessel and incubation for 8 minutes at 37 C. After incubation, the collagenase solution within each vessel was decanted into 15mL centrifuge tubes, and DMEM supplemented with 10% FBS rinsed through the lumen into a centrifuge tube to further dislodge intimal cells. A cut was then made along the length of the vessel so that the lumen could be gently scraped with a cell scraper to isolate any remaining intimal cells. These contents were centrifuged for 8 minutes at 800 rpm, resuspended in DMEM supplemented with 5% FBS, and plated for culture in dishes with collagen-coated coverslips. Endothelial cell populations were confirmed at day 7 using immunofluorescent images of platelet endothelial adhesion molecule 1 (CD31/PECAM1) phalloidin, and 4',6-diamidino-2-phenylindole (DAPI) (All antibodies: Abcam Inc, Cambridge MA) on the Zeiss LSM 510 confocal microscope (Carl Zeiss Microscopy GmbH, Jena, Germany).

Following intima removal, denuded vessels were placed in fresh tubes containing collagenase II solution (as described above) and incubated for 10 minutes at 37 C with mechanical agitation. After incubation, samples were removed from tubes, and the loosened adventitia removed with forceps and returned to tubes of collagenase solution. DMEM supplemented with 10% FBS was added to the tubes containing adventitia and collagenase solution, and tubes were centrifuged for 8 minutes at 800 rpm, followed by resuspension in fresh DMEM with 10% FBS and plated for culture with collagen-coated coverslips. Smooth muscle populations were confirmed with confocal microscopy at day

7 using immunofluorescent images of fluorescently labeled Alpha Smooth Muscle Actin (α-SMA) antibodies and DAPI on the Zeiss LSM 510 confocal microscope

After adventitia removal, the remaining tissues were placed in fresh tubes of collagenase solution and incubated with agitation for 30 minutes at 37 C. Samples were then cut into small pieces (1-2 mm^2), returned to tubes containing collagenase solution, and incubated further at 37 C for 4 hours with agitation. Following incubation, DMEM with 10% FBS was added, and samples were centrifuged for 8 min at 800 rpm, resuspended in fresh DMEM with 10% FBS, and plated for culture with collagen-coated coverslips. Fibroblast populations were confirmed with confocal microscopy at day 7 using immunofluorescent images of Fibroblast-Specific Protein 1 (FSP1/S100A4) and DAPI on the Zeiss LSM 510 confocal microscope.

Cell cultures were assessed qualitatively using an inverted phase contrast microscope with CCD camera. Proliferation was quantitated using the Roche 5-Bromo-2'-deoxy-uridine (BrdU) Labeling and Detection Kit I according to the manufacturer's instructions (Roche Diagnostics GmbH, Mannheim, Germany). Briefly, after 7 days of culture, 3 uL BrdU per mL medium was added to plates containing coated coverslips for 3h. After labeling, coverslips were rinsed thrice in PBS and fixed in Ethanol/Glycine fixative solution at -20 C for 30 minutes, then rinsed thrice more in PBS. For staining, coverslips were covered with 100 uL anti-BrdU diluted 1:10 with Incubation Buffer (both from Roche kit, above) and incubated for 1 hour at 37 C, followed by 3 rinses for 10 minutes each in PBS. Next, coverslips were covered with fluorescein-labeled anti-mouse IgG diluted 1:10 in PBS and incubated for 1 hour in the dark at 25 C, followed by 3 rinses of 10 minutes each in PBS and staining with DAPI diluted 1:5000 in PBS and incubation

for 1 hour in the dark at room temperature. After rinsing, coverslips were mounted using a 1:1 PBS/Glycerol mounting medium and imaged using the Zeiss LSM 510 confocal microscope (Carl Zeiss Microscopy GmbH, Jena, Germany).

3.3.3 Ex Vivo Vessel Culture

The *ex vivo* bioreactor used for this investigation was designed so that most wetted parts could be easily autoclaved and contained in an incubator when assembled (Figure 1). Flow was generated via a Cole-Parmer Masterflex L/S Easy-Load II roller pump head (model 77201-60) attached to a Cole-Parmer Masterflex L/S roller pump (model 7552-02), and output was controlled by a Cole-Parmer Masterflex Wash-Down Modular Controller (model 7552-71) (Cole-Parmer, Vernon Hills, IL). Pressure was adjusted via a tubing pinch valve downstream of the vessel and measured by an Omega digital pressure gauge (model DPG8001) (Omega, Norwalk, CT) located upstream of the sample offset. All tubing consisted of 0.64 cm inner diameter Masterflex PharMed BPT (Cole-Parmer, Vernon Hills IL). Temperature in the incubator was maintained at 37^{o} C, and CO_2 concentration was maintained at 5%.

ITAs, RAs, and GSVs were cultured in the *ex vivo* perfusion bioreactor with DMEM supplemented with 10% fetal bovine serum, 1% penicillin/streptomycin, 1% amphotericin-B, and 1% streptomycin for six hours (6h) or seven days (7d) under *in situ* (IS) or coronary-like (LAD) media perfusion pressure and flow conditions (Table 3.1). For 7d cultures, all media (150 ml), was replaced at day 4. Endothelial and smooth muscle cell viability was confirmed at day 4 using phenylephrine HCl (10^{-5} M) and carbamylcholine chloride (10^{-5} M) to elicit smooth muscle-dependent contraction and endothelial-dependent relaxation, respectively. At the end of each culture, sections were cut from the middle of

each sample, snap frozen on dry ice, and stored at -80^{o} C for gene expression analysis or cut and fixed in 4% paraformaldehyde for histological analysis.

3.3.4 Gene Expression Analysis

Total RNA was isolated from snap frozen tissue samples using the Qiagen RNeasy Fibrous Tissue Mini Kit (Qiagen, Hilden, Germany) including a homogenization step using the Qiagen TissueRuptor (Qiagen, Hilden, Germany). Concentrations of isolated RNA was quantified using the Implen Nanophotometer Pearl (Implen, Munich, Germany). All RNA samples had A_{260}/A_{280} and A_{260}/A_{230} ratios > 1.9. 500ng. RNA was converted to cDNA using an iScript cDNA Synthesis Kit (Bio-Rad, Hercules, CA). Relative gene expression within diluted cDNA samples (5x in RNase-free H_2O) was then quantified via real-time PCR on a Bio-Rad CFX Connect Real-Time System (Bio-Rad, Hercules, CA) using Fast SYBR Green Master Mix (Applied Biosystems, Foster City, CA). Seven genes associated with vascular remodeling were selected for analysis as mentioned and beta-actin (*ACTB*) used a housekeeping gene (Table 3.2). Samples (n=3) were run in triplicate, and all plate configurations run three times. Fluorescence threshold (300 RFU) was set the same for each plate to enable comparison across different plates. Relative gene expression was calculated using the Pfaffl method [183]. Melt curve analysis was performed for each real-time PCR run.

3.3.5 Histological Analysis

Paraformaldehyde fixed samples were embedded in paraffin, sectioned with a microtome at 5 μm thick, and stained with hematoxylin/eosin. Digital images of stained slides were acquired on a Nikon E600 microscope (Nikon Instruments, Melville, NY) using QCapture imaging software (QImaging, Surrey, BC).

3.3.6 Statistical Analysis

Data are reported as the mean ± SEM of all measurements for a given experimental group. All cultured groups have sample size n=3; for t0 samples n=6. Two-tailed, two sample, Student's T-tests assuming unequal variance were conducted at $\alpha = 0.05$ between reference samples (see *Gene Expression Analysis* above) and experimental groups.

3.4 RESULTS

3.4.1 Basal Gene Expression

To provide a baseline comparison of healthy gene expression, genes associated with remodeling were compared between freshly isolated LAD, ITA, RA, and GSV samples (n=6) immediately after animal sacrifice (Figure 3.2). Overall, basal gene activity was similar across the four vessel types, with certain notable differences. COL3A1 ($p=0.030$) was the only gene found to be statistically lower when comparing basal gene expression of ITAs to LADs. Basal gene expression of FN1 ($p=0.049$) however, was found to be significantly higher in the RA than the LAD while SERPINE1 was lower in the RA than either the LAD ($p=0.002$) or ITA ($p=0.031$). SERPINE1 ($p=0.021$) and TGFB1 ($p<0.001$) were both lower in the GSV compared to the LAD.

3.4.2 Comparison of Primary Vascular Cells

Cell populations were successfully isolated from intimal, medial, and adventitial layers of LAD, ITA, RA, and GSV samples. Confocal microscopy qualitatively suggests intimal populations consisting of mostly endothelial cells, medial populations consisting of mostly smooth muscle cells, and adventitial populations consisting of mostly fibroblasts. Intimal populations appeared qualitatively similar across vessel types and with characteristics similar to disorganized endothelial cells (Figure 3.3). Medial populations

appeared to consist primarily of spindle-shaped SMCs in ITA samples; however, LAD, RA, and GSV samples appear to have significant populations of non-spindle shaped cells as well. Initial adventitial population sizes varied widely across vessels due to the amount of tissue available and the perivascular environment of each vessel. Once in culture, cells from all vessels appeared similar, exhibiting classic stellate fibroblast morphology.

BrdU uptake suggested variable proliferation rates across both layers and vessel types at 7 d. RA and GSV intimal populations proliferate at higher rates (131 of 213 and 46 of 67 observed cells, respectively) than LAD and ITA (141 of 396 and 66 of 410, respectively). Proliferation rates appeared relatively similar for medial cells of observed LAD, RA, and GSV samples (89 of 202, 27 of 48, and 108 of 214, respectively), but ITA samples exhibited a lower proportion of proliferating cells (60 of 215). In observed adventitial samples, LAD and ITA cells almost all exhibit BrdU uptake (28 of 29 and 85 of 86, respectively), while RA and GSV cells have much lower proportions (18 of 62 and 44 of 113, respectively).

3.4.3 Effects of CABG Loading Conditions on Gene Expression

To assess the early remodeling effects of mechanical stimuli characteristic of the coronary environment, gene expression activity was compared between ITAs, RAs, and GSVs cultured under *in situ* or LAD conditions and measured after 6 h and 7 d of perfusion culture (Figure 3.5). Collectively 66.7±9.91% of genes tested after 6 h and 52.4±7.27% of genes after 7 d were disturbed by IS culture when compared to acutely measured gene expression.

Four total ITA genes were affected by short and long-term LAD culture conditions when compared the IS culture conditions. The ITA had significantly higher *COL3A1*

($p<0.001$) and significantly lower *SERPINE1* ($p=0.004$) and *TGFB1* ($p=0.025$) gene expression at 6 h LAD. *SERPINE1* ($p<0.001$) and *TGFB1* ($p=0.021$) remained low after 7 d LAD culture while a significant increase in *TIMP1* ($p=0.027$) gene expression occurred at this alter time point.

Six total RA genes were affected by short and long-term LAD culture conditions. The RA had significantly higher *COL3A1* ($p<0.001$) and lower *FN1* ($p<0.001$), *SERPINE1* ($p=0.016$), *TGFB1* ($p<0.001$), and *TIMP1* ($p=0.004$) at 6 h LAD culture conditions. After 7 d LAD culture, *COL3A1* returned to basal levels while *SERPINE1* ($p=0.005$) and *TGFB1* ($p<0.001$) decreased further with significant increases in *FN1* ($p<0.001$) and *MMP2* ($p=0.006$) observed.

Five total GSV genes were affected by LAD culture conditions compared to IS. *FN1* ($p=0.005$), *MMP2* ($p=0.035$), and *TIMP1* ($p=0.033$) were all decreased at 6 h LAD compared to 6 h IS. After 7 d LAD culture *FN1* ($p=0.020$) gene expression actually increased compared to 6h LAD but was still less than that of 6 h IS ($p=0.001$).

3.4.4 Effect of Ex Vivo Culture on Histology

ITA, RA, and GSVs at day 0 were histologically distinct (Figure 3.6, top). Most notably was the presence of approximately 15 elastic lamellae present in the ITA samples and a thinner medial layer that are obvious even in an H&E stain. In contrast, RAs and GSVs contain a thick muscular media with well-organized cell nuclei, often folding in histological sections. In RAs and GSVs a single internal elastic lamina was prominent. Despite differences in gene expression, IS cultured vessels were morphologically similar when comparing between acute to 7 d time points for any given vessel (Figure 3.6, middle). The only notable difference was an apparent decrease in endothelial cell continuity.

Overall, the ITA histology appeared insensitive to IS versus LAD culture conditions. RA and GSVs cultured under LAD conditions for 7 days however, showed marked changes in cell and tissue morphology compared to day 0 or 7d IS. Namely, endothelial layers were sparse of nuclei while a gradient in medial cells was apparent with the inner most cells necrotic or pyknotic and the outermost appearing otherwise healthy.

3.5 DISCUSSION

This investigation sought to understand the early remodeling processes occurring in CABG tissues after implantation using tissue perfusion as a tool to evaluate whether the three most common CABG tissues have inherently different abilities to undergo adaptive remodeling. To that end, primary vascular cells were isolated from LAD, ITA, RA, and GSV samples, and an *ex vivo* perfusion bioreactor utilized to culture porcine samples under in situ pressure and flow conditions and conditions representative of the coronary vasculature. Cell cultures demonstrate variable rates of mitotic activity across vessel types and layers. 6 h cultures were utilized to elucidate the acute response of graft tissues after CABG, and 7 d cultures were utilized to elucidate remodeling responses as vessels start to adapt to chronic mechanical changes. Gene expression of seven genes associated with vascular remodeling were evaluated as a proxy for activated remodeling pathways and downstream remodeling outcomes while histological staining provided qualitative evidence of morphological changes due to *ex vivo* culture conditions.

Our previous work quantified the homeostatic mechanics of the LAD, ITA, RA, and GSV under their *in situ* loading environment and demonstrated the amount of mechanical deviation caused by implantation in the coronary circulation to be different for candidate graft vessels [15]. Several other groups have published investigations involving

ex vivo culture relating to CABG [52,83,97,98,100,184,185]. These tissue-level culture studies allow for specific mechanical loading conditions and natural interactions between cell-types that are not possible in flat-plate culture studies. Most tissue cultures studies however, have focused almost exclusively on saphenous veins due to the implication of vein grafts in many CABG failures, and each investigation focused on different aspects of graft remodeling: viability/apoptosis [97], shear stress versus pressure [52], cell proliferation [185], morphometry [99], and oxygenation [100]. However, none have focused on the differential remodeling ability of ITAs, RAs, and GSVs. Whereas GSVs have a historical precedence in CABG grafting, ITAs are the standard-of-care and the RA, an option for second and third bypass graft procedures [113].

The degree towards which coronary-like culture conditions drive pathological remodeling in both the RA and GSV was surprising. Specifically, RAs and GSVs, (to a lesser extent ITAs), exposed to coronary-culture conditions, but not IS conditions, experience a considerable loss of endothelium and limited apoptosis of cells in the inner layer of the media. These vessels would likely reendothelialize rapidly in vivo and mural cells repopulate [186]; however, such processes could be the difference between healthy and pathological remodeling. A functioning endothelium plays a critical role in SMC phenotype modulation and the denudation process is known to cause intimal hyperplasia, adventitial cell proliferation, fibrosis, and constrictive remodeling [187]. Our work supports the theory that many cells of transplanted tissues are lost soon after transplantation and repopulated with host-derived cells [186,188,189]. In contrast, the outer layers of the media retained a normal looking histology remarkably similar to vessels prior to culture.

This observation has important implications with adventitial fibroblasts and progenitor cells playing critical roles in remodeling of vascular grafts [190].

We anticipated that ITA, RA, and GSVs exposed to LAD pressure and flow conditions would experience an acute, pathological deviation in the expression of many of our genes compared to their matched IS culture conditions followed by an eventual restoration of basal levels as tissues restore homeostasis. This effect was observed for *Col3A1* and *FN1* genes for all vessels and to a lesser extent *MMP2* (ITA and GSV only) and *TIMP1* (RA and GSV only). In contrast, *SERPINE1* and *TGFB1* continued a path of decreased expression at 7 d while *VCAM1* only increased. Such findings suggest that homeostasis was still not observed at this time point and such behavior is consistent with prior in vivo remodeling studies that indicate 2-3 weeks are necessary for gross changes in tissue structure [47]. *VCAM1* and *SERPINE1* are both genes expressed predominantly by endothelial cells and thus pathological conditions are likely given the scarcity of ECs in cultures of RA and GSVs under LAD flow conditions. Despite this, sufficient concentrations of RNA were procured from pre- and post-culture cell populations for data analysis. Comparisons between IS and LAD cultures of RA and GSVs also support the approach that long-term ex vivo conditioning in a bioreactor should use a stepwise or ramping approach to transition from in situ to coronary like media dynamics [84,94]. This approach has been shown to generate stable solutions and prevent maladaptation in computational simulations of vein remodeling [191].

For the most part, gene expression profiles were similar across vessels when measured immediately after sacrifice with *COL3A1* found to be the only gene differentially expressed by the ITA compared to the LAD while, *SERPINE1*, *FN1* (RA only), and *TGFB1*

(GSV only) were found to be different in the RA and GSVs compared to the LAD. These powerful finding provides important information regarding basal gene expression from different source tissues irrespective of tissue culture. We further expected that because RA and GSVs experience increased levels of pressure and flow in LAD cultures, they would result in similarly regulated gene profiles. Such behavior however, was observed for most genes except *COL3A1*. In contrast, the ITA IS conditions were most like those of the LAD thus it was supportive to observe modest changes in gene expression at 6 h of LAD culture for this tissue.

In theory, this experimental design should allow for clear identification of early remodeling pathways stimulated by CABG as the bioreactor was designed to perfuse vascular tissue with pressure and flow levels equivalent to the coronary circulation or any other desired loading conditions. However, vessels were unavoidably exposed to random variables, which could confound the results of this investigation. To account for these variables, control cultures were performed under *in situ* loading conditions for each vessel. If environmental stimuli were unchanged for these control groups compared to their basal *in situ* state (i.e., t0 results), then we would not have seen differences in gene expression or histology for these groups. Unsurprisingly that was not the case with 52.4±7.27% of genes different after 7 d of IS culture conditions compared to their basal (freshly harvested) expression levels. This could be due to a number of factors: substitution of blood for culture medium, lack of perivascular tissue, incomplete inflammatory response, or insufficient replication of physiological hemodynamic waveforms. As it stands, attention should be focused on the differential responses as a result of culture under coronary versus *in situ* loading conditions rather than in reference to the freshly harvested tissues.

The results of this investigation indicate that primary intimal, medial, and adventitial cells from selected source tissues exhibit similar morphology but vary in the rates of proliferation when isolated and cultured under the same conditions for 7 d. When tissues were cultured in an ex vivo perfusion bioreactor, molecular pathways associated with vascular remodeling were activated as early as 6 h after implantation in a new environment, and those pathways were sensitive to the specific medial perfusion dynamics to which the vessel was exposed. Some effects appear to be at least partially the result of *ex vivo* culture, but responses occurring differentially between IS and LAD cultures were the result of chronic deviation from homeostasis. Moreover, some but not all of these remodeling-associated pathways were differentially activated across our three graft vessel-types, which, together with differing observed rates of cell proliferation, suggest the possibility of differential propensity for vascular remodeling and adaption when used for CABG. It was therefore intuitive that significantly different outcomes occur for these vessels when used clinically for CABG. In situ, each vessel has a unique homeostatic state of stress and these vessels experiences different changes in loading due to grafting [15]. Thus, using a continuum mechanics framework and prolonged tissue culture (3 weeks), our future investigations seek to isolate the inherent remodeling capacity of potential graft vessels from the mechanical deviation to which they were subjected.

3.6 ACKNOWLEDGEMENTS

The authors would like to acknowledge the experimental contributions of summer medical student Nicole Carey to the current work. This work was supported by the National Institutes of Health (NIH) P20GM103444 and R21EB022131 grants.

3.7 TABLES

Table 3.1 – *Ex vivo* culture conditions for control (*In Situ*) and experimental (coronary –LAD) groups for graft tissues ITA, RA, and GSV.

	In Situ			*Coronary*		
	P (mmHg)	Q (mL/s)	λ	P (mmHg)	Q (mL/s)	λ
LAD	102	0.52	1.33	102	0.52	1.33
ITA	100	0.76	1.22			
RA	94	0.19	1.17			
GSV	15	0.17	1.24			

Table 3.2 – Primer sequences of 7 remodeling-associated genes and *ACTB* housekeeping gene.

		Sequence (5' → 3')
COL3A1	For	GCGGTGACAAAGGTGAAACC
	Rev	GGCTACCTACTGCACCTTGG
FN1	For	TGGGGATACCTGGAGCAAGA
	Rev	GCCTCTCACACTTCCACTCC
SERPINE1	For	CCTAACCAGGCGGACTTCTC
	Rev	CATGCGGGCTGAGACGATAA
VCAM1	For	CGCTGGTCATGAATCCCGTT
	Rev	ATCTCTGGGTCCTTGGGGAA
MMP2	For	CCTGATCTGGACCCCGAAAC
	Rev	TATCCATCTCCGTGCTCCCA
TGFB1	For	CTAATGGTGGAAAGCGGCAA
	Rev	CCCGAGAGAGCAATACAGGTT
TIMP1	For	CACCTGCAGTTTTGTGGCTC
	Rev	GGGATGGATGTGCAGGGAAA
ACTB	For	AGGCCAACCGTGAGAAGATG
	Rev	CCCATCCCCAGAGTCCATGA

3.8 FIGURES

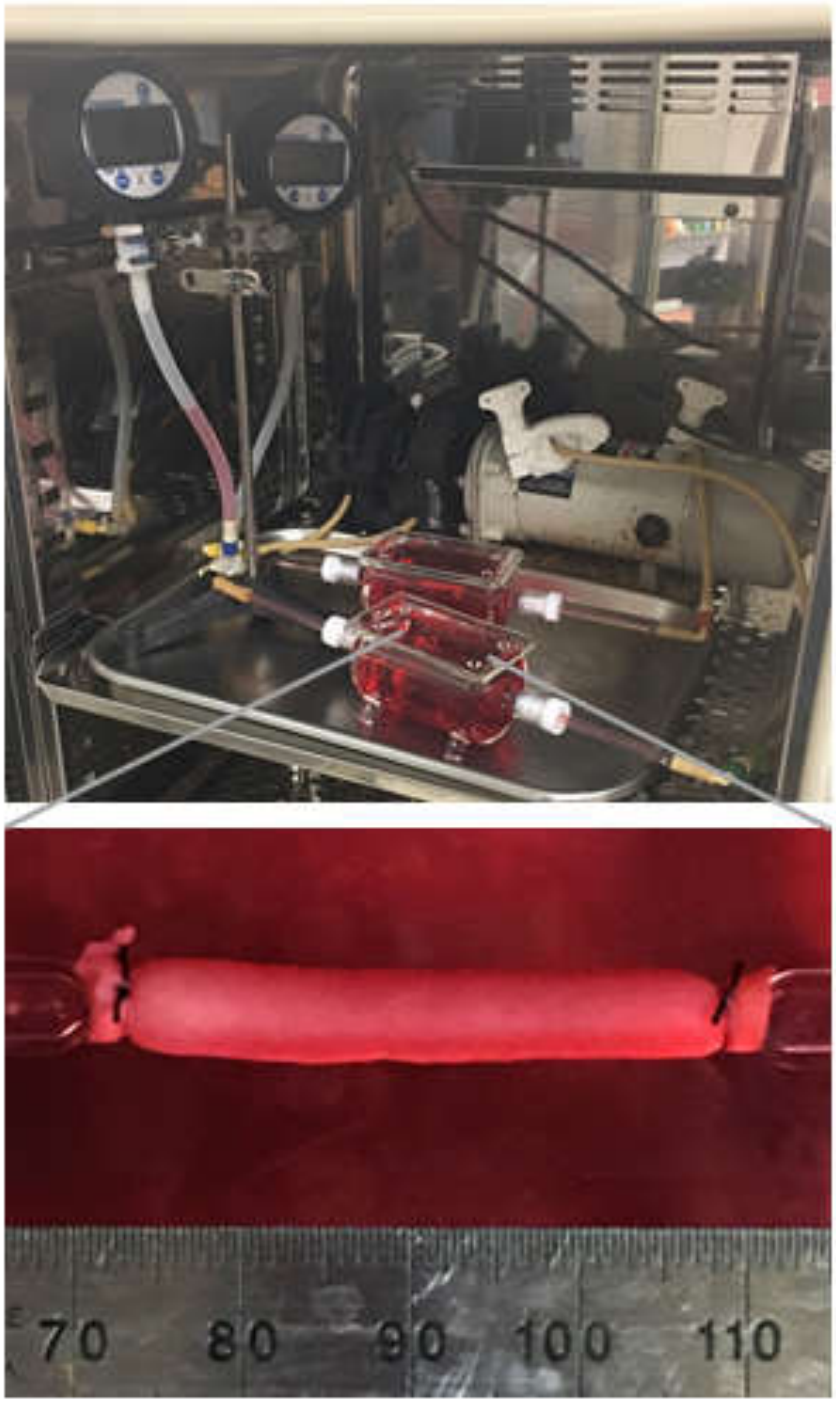

Figure 3.1 – Parallel e*x vivo* pulsatile perfusion bioreactors assembled in incubator (top) with ITA sample in culture (bottom).

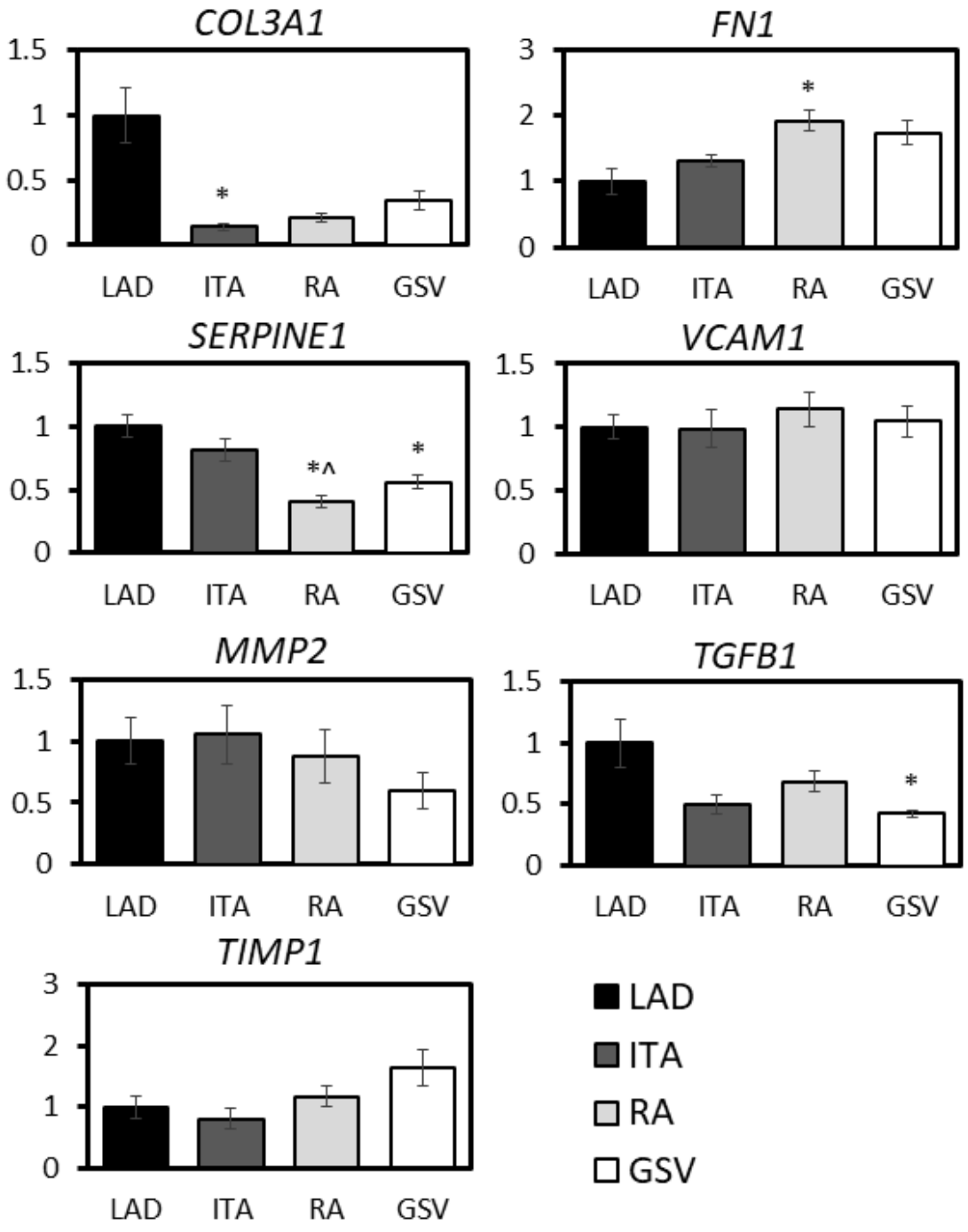

Figure 3.2 – Comparison of remodeling-associated gene expression of freshly isolated (t0) LAD, ITA, RA, and GSV, where * and ^ indicate $p<0.05$ with respect to LAD and ITA respectively using two-tailed, two sample, Student's t-test (n=6). No genes were significantly different between RA and GSV samples.

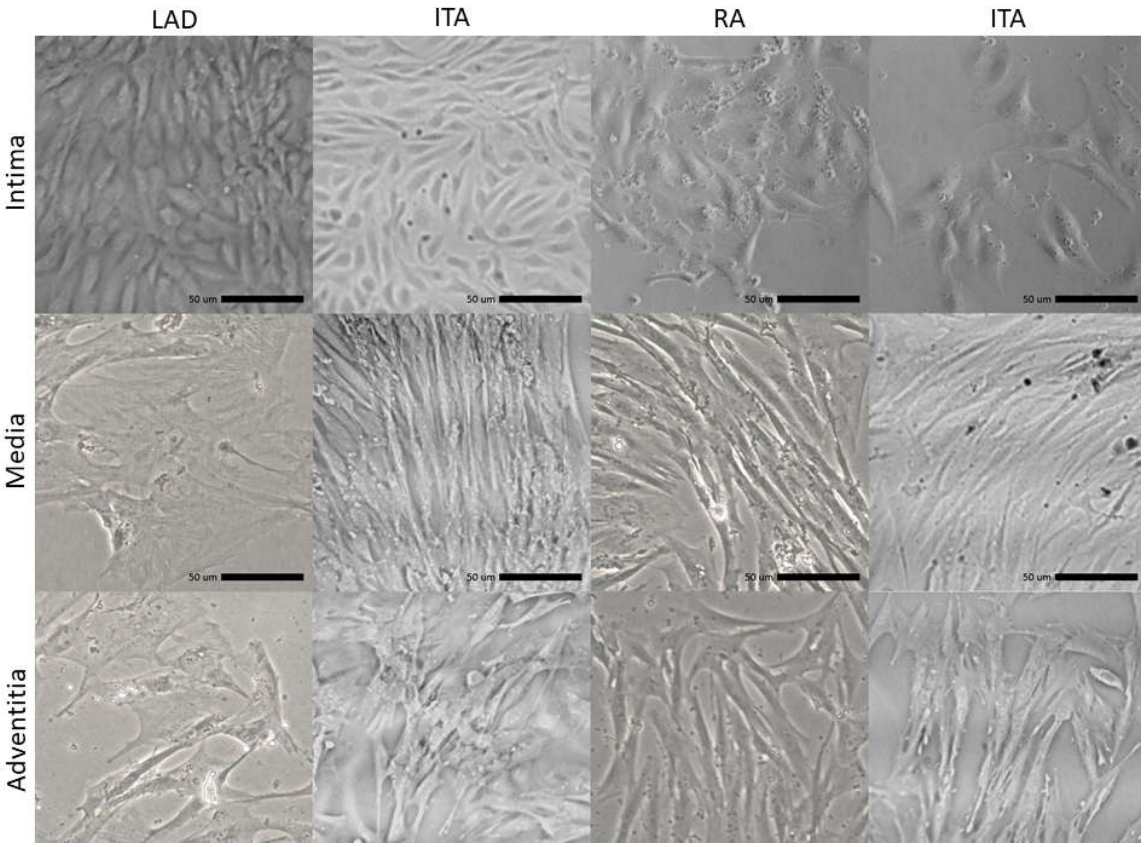

Figure 3.3 – Representative phase contrast images (20x) of isolated cells harvested from the intimal, medial, and adventitial layers of LAD, ITA, RA, and GSVs after 7days in culture plates.

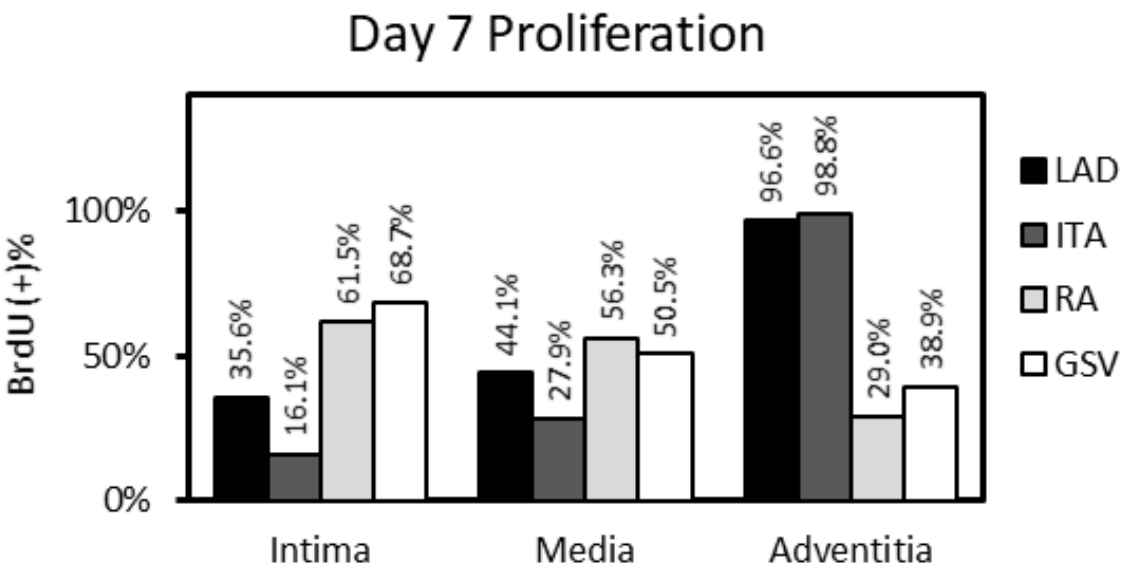

Figure 3.4 – BrdU positive staining of isolated cells harvested from the intimal, medial, and adventitial layers of LAD, ITA, RA, and GSVs after 7 days indicate the % of proliferating cells.

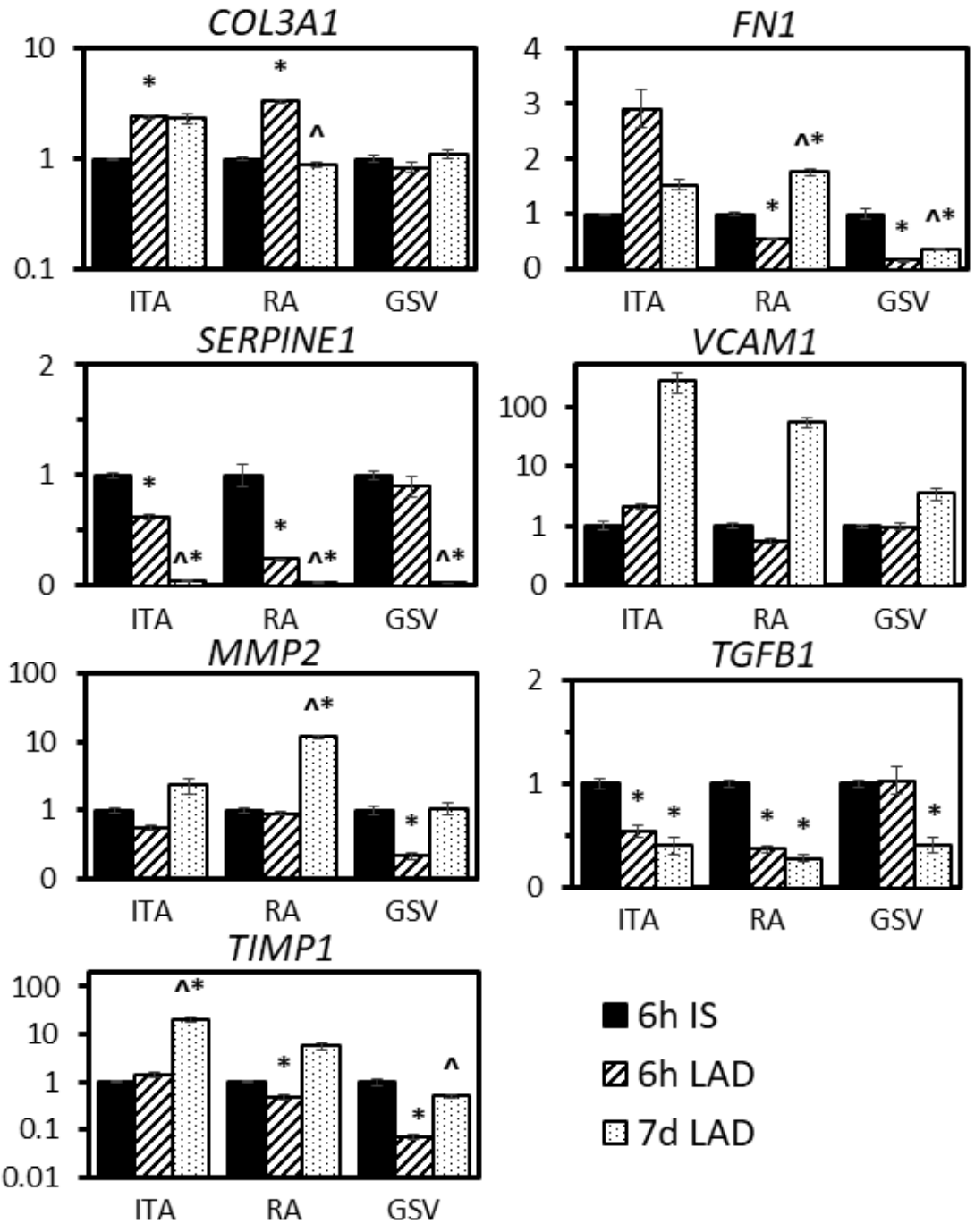

Figure 3.5 – Comparison of remodeling-associated gene expression changes in ITA, RA, and GSV samples as a result of acute (6h) and prolonged (7d) *ex vivo* tissue culture exposed to media perfusion approximating *in situ* (IS) or LAD conditions. * and ^ indicates $p<0.05$ with respect to 6h IS and 6h LAD respectively using two-tailed, two sample, Student's t-test (n=3).

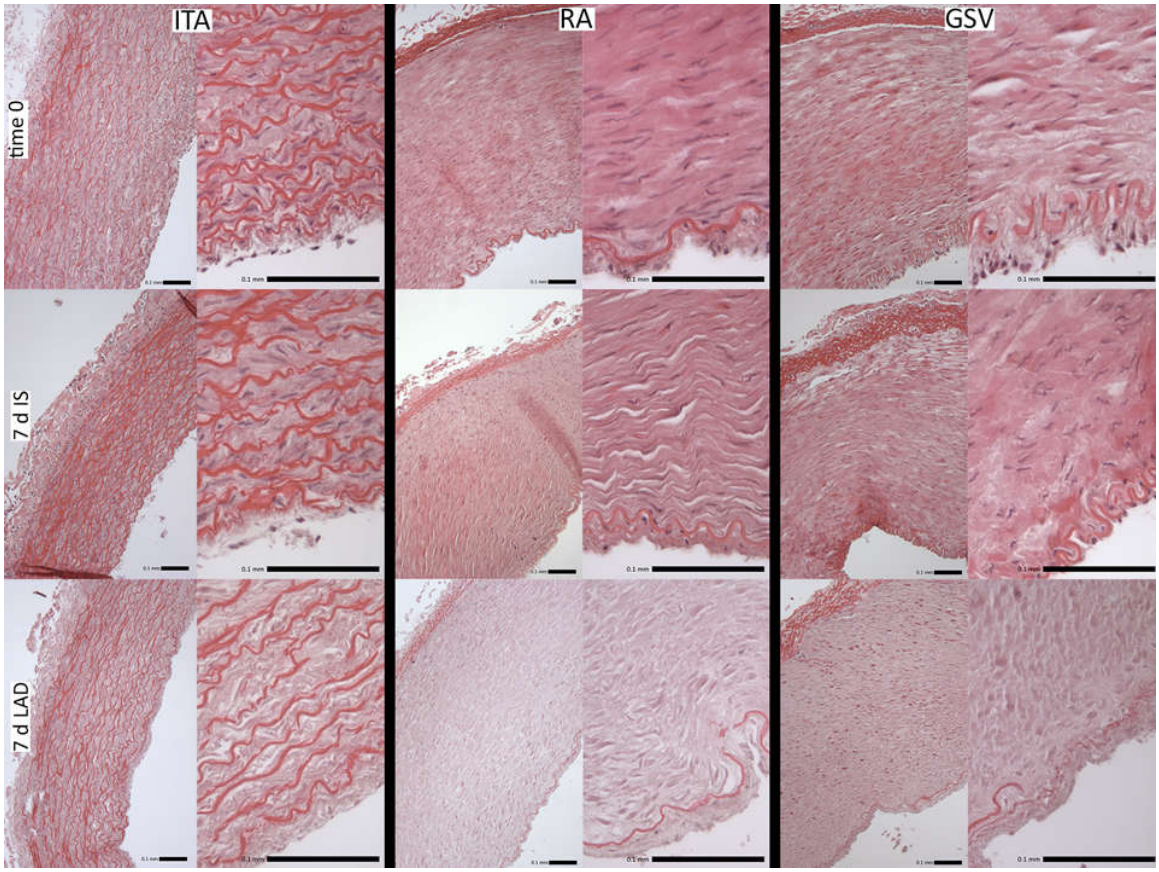

Figure 3.6 – Representative hematoxylin and eosin (H&E) stained cross sections of ITA, RA, and GSVs before (top row) and after (middle and bottom rows) 7 days of *ex vivo* perfusion culture at in situ (IS; middle row) or left anterior descending (LAD; bottom row) culture conditions. All images are paired at 100x (left) and 400x (right) magnifications with 0.1 mm scalebars.

CHAPTER 4

PULSATILE PERFUSION BIOREACTOR FOR BIOMIMETIC VASCULAR IMPEDANCES[3]

[3] Prim, D. A., Potts, J. D., & Eberth, J. F. Submitted to *ASME Journal of Medical Devices*, 1/7/2018

4.1 ABSTRACT

Intricate patterns of blood pressure and flow are generated by the cyclic contraction and relaxation of the heart and the coordinated opening and closing of valves. These pulsatile waves are augmented by the resistance, compliance, and inertance properties of the vasculature resulting in unique hemodynamic characteristics present at distinct anatomically locations. In vivo the hemodynamically generated loads, transduced as physical signals into resident vascular cells, are crucial to the maintenance and preservation of healthy physiology. Failure to recreate biomimetic loading in vitro however, can lead to pathological gene expression and aberrant remodeling. As a generalized approach to improve native and engineered blood vessels, we have designed, built, and tested a pulsatile perfusion bioreactor based on the concept of biomimetic impedances. Here the elements of an incubator-based culture system were formulaically designed to match the vascular impedance of a brachial artery using a 5-element electrohydraulic analog that incorporates both inherent (systemic) and added elements. Using freshly harvested saphenous veins, the relative expression of seven known mechanically sensitive remodeling genes were analyzed using quantitative polymerase chain reaction (qPCR) after 6 h exposure to different arterial or venous-like waveforms. While most genes were sensitive to differences between venous and arterial conditions only Plasminogen Activator Inhibitor (PAI1) was differentially expressed across distinct arterial-like waveforms. Our analytical and experimental results provide a framework towards the design of hemodynamic-mimetic vascular culture systems.

4.2 INTRODUCTION

Pulsatile hemodynamics are a hallmark of the mammalian cardiovascular system,

and a palpable pressure was once considered to be the most fundamental sign of life [192,193]. Pulsatile waves of blood pressure and flow initiate at the heart and travel a circuitous path of compliant and muscular blood vessels so that at each anatomical location [194], and amongst different mammalian species [72], local hemodynamic waveforms are distinct [71]. Hemodynamics influence numerous gene expression pathways resulting in extra cellular matrix turnover and assorted cell-fate processes that are fundamental to a healthy physiology [58,67,195,196]. As a result, inter- and intra-species comparisons of blood vessel histology demonstrate a dramatic variation in composition that enables optimum functionality in their in situ environment [15,124,193]. Perturbations from this homeostatic environment therefore initiate adaptive remodeling responses.

Cyclic pressure induces periodic loading of vascular smooth muscle and fibroblast cells while periodic and oscillatory flow stimulates luminal-lined endothelial cells [8,47]. Normal physiological hemodynamics encourages basal gene expression and protein turnover while pathological hemodynamics can result in serious vascular disease conditions such as atherosclerosis, hemorrhage, dissection, and aneurysm formation [73]. Thus, recreation of biomimetic levels of dynamic pressure and flow in the culture media of an in vitro system are crucial to sustaining a healthy and functional tissue and enabling desirable tissue engineering outcomes. The extent towards which the precise culture media dynamics must be recreated is currently unknown but such knowledge could be used to guide the simplicity of any culture device system.

An ever growing body of evidence suggests that tissue culture can be used as a means to experimentally isolate and test native blood vessels, improve engineered grafts, perform high throughput drug testing, and drive stem cell differentiation

[44,84,96,99,185,197–201]. Paramount to the success of these experiments are the precise regulation of the culture media fluid dynamics and the preservation of a sterile but physiological environment [202]. The latter is aided by a minimalist approach to the hardware design while the former requires a sound theoretical framework with a priori knowledge of native conditions. The electro-hydraulic analogy pioneered by William Henry Preece, provides a convenient methodology enabling a seamless translation of culture media fluid dynamics into electrical circuits [86,88]. Here the voltage, current, resistance, capacitance, and inductance are represented as pressure, volumetric flow rate, hydraulic resistance, compliance, and inertance respectively. Impedances, which are commonplace in AC circuit analysis, can then be used to represent the opposition of a hydraulic circuit to fluid flow [192]. The simplicity of this analogy, and the abundance of analytical techniques developed for AC circuit analysis makes it well suited for the practicality of an incubator system physically represented by pumps, valves, compliance chambers, tubing, and culture media.

While many existing vascular perfusion devices are capable of achieving targeted hemodynamics for a given blood vessel, a general framework for diverse applications and numerous mammalian species is presented here that includes the phasic relationship between blood pressure and flow [44,84,96,99,185,197–201]. Simultaneously recorded brachial artery blood pressure and volumetric flow waveforms were digitized from the classic literature [1–3] and represented as mathematical equations using a Fourier series analysis [85,87,203–205]. The waveforms, initially in the time-domain, were recreated in the frequency domain as impedance magnitudes and phase angles and then used to match a 5-element electrohydraulic analog for an incubator-based hydraulic circuit configuration.

Realistically constrained parameters were then found that provide a basis for the culture system component design in order to match in vivo impedances [86,87,204]. As an input to the system pulsatile volumetric flow was generated using a custom designed, gear-driven, roller pump with each channel providing a phase of volumetric flow that was quantified from the Fourier analysis.

Drawing from the design of biomimetic impedance matching systems [89,92], we used elements created from common biologically-compatible and sterilizable tissue culture materials. Freshly harvested porcine great saphenous veins (GSV) were exposed to brachial artery (BrA), GSV, or left coronary artery-like (LCA) pressure and flow waveforms created using a unique pump configuration with design elements specific for each targeted vascular impedance. Since measurable macroscopic level remodeling (e.g., protein content) involve long-term processes that follow pre-programmed gene expression, we studied select genes after 6h of exposure to different media pressure and flow conditions. This approach permitted comparisons of perturbed media dynamics that could be isolated from the acute effects of surgical procedures. Seven genes expressed by endothelial, smooth muscle, and/or fibroblast cells that are widely accepted to be mechanosensitive and implicated in early vascular remodeling were studied: collagen III (Col 3), matrix metalloprotease II (MMP 2), tissue inhibitor of matrix metalloprotease I (TIMP 1), vascular cell adhesion molecule 1 (VCAM 1), fibronectin I (FN 1), plasminogen activation inhibitor I (PAI 1), and transforming growth factor beta I (TGFβ 1) [176,177,182,206]. Overall results from these studies provide feedback towards the utility of our design.

4.3 METHODS

4.3.1 Fourier Analysis of In Vivo Hemodynamics

A discrete Fourier transform was used to convert synchronous blood pressure and volumetric flow from the time domain into the frequency domain using data published in [1–3] for the GSV, BrA, and LCA. The complex valued spectrum of the flow and pressure signals are [207]

$$Q(\omega_k)=\sum_{n=0}^{N-1} q(t_n)\cdot e^{-j\omega_k t_n}, \qquad P(\omega_k)=\sum_{n=0}^{N-1} p(t_n)\cdot e^{-j\omega_k t_n}, \qquad k=0,\,1,\ldots,\,N-1 \quad [4.1]$$

where $q(t_n)$ and $p(t_n)$ are the pressure (mmHg) and flow (ml/s) at discrete time t_n and $Q(\omega_k)$ and $P(\omega_k)$ the corresponding pressure and flow at a frequency ω_k. Here $\omega_k = 2\pi k/(NT)$, where N are the total number of samples and T the sampling interval.

Likewise, the inverse discrete Fourier transform is

$$q(t_n)=\frac{1}{N}\sum_{k=0}^{N-1} Q(\omega_k)\cdot e^{j\omega_k t_n}, \qquad p(t_n)=\frac{1}{N}\sum_{k=0}^{N-1} P(\omega_k)\cdot e^{j\omega_k t_n}, \qquad n=0,\,1,\ldots,\,N-1 \quad [4.2]$$

and can be used to rebuild the time-domain signal from the frequency domain. Equations [4.1] and [4.2] can be converted from the complex exponential form to trigonometric functions using Euler's identity, $e^{j\omega_k t_n}=\cos(\omega_k t_n)+i\sin(\omega_k t_n)$. This form is also included here as it can be used to provide an intuitive interpretation of media dynamics. Henceforth the subscripts k and n are omitted for brevity.

Equation [4.1] results in a complex number that contains both real $(\Re)$ and imaginary $(\Im)$ parts. For this, the magnitude and phase angle for the flow signal can thus be calculated using

$$|Q(\omega)|=\sqrt{\left(\Re\{Q(\omega)\}\right)^2+\left(\Im\{Q(\omega)\}\right)^2}, \qquad \angle Q(\omega)=\tan^{-1}\left(\frac{\Im\{Q(\omega)\}}{\Re\{Q(\omega)\}}\right) \quad [4.3]$$

and likewise calculated in a similar manner for $|P(\omega)|$ and $\angle P(\omega)$.

4.3.2 Vascular Impedances

Vascular impedance in the vascular system is defined as the measure of the opposition to pulsatile flow when a pulsatile pressure is applied. Stated succinctly it is the ratio of the complex quantities

$$Z(\omega) = P(\omega)/Q(\omega) \qquad [4.4]$$

so that the impedance modulus (mmHg-s/ml) and phase (rad) are found via

$$|Z(\omega)| = \frac{|P(\omega)|}{|Q(\omega)|}, \qquad \angle Z(\omega) = \angle P(\omega) - \angle Q(\omega) \qquad [4.5]$$

In our design [4.5] provides the desired impedance magnitude and phase.

4.3.3 Selection and Evaluation of an Electrohydraulic Analogy

The individual elements of an impedance circuit include resistors, capacitors, and inductors of the form

$$Z_R = R, \qquad Z_C = \frac{1}{j\omega C} = \frac{-j}{\omega C}, \qquad Z_L = j\omega L \qquad [4.6]$$

with R (mmHg·s/ml) is the resistance, C (ml/mmHg) the capacitance or compliance and L (mmHg·s^2 /ml) the inductance or inertance. From [4.6] it is clear that the capacitor and inductor are dependent on frequency while the resistive elements are not. This dependency helps in the calibration of the individual elements.

Plotting the impedance magnitude and phase of a human brachial artery provides a guideline for the general behavior of the desired system. Qualitatively it can be observed that the magnitude of impedance decreases while the phase initially decreases and then approaches zero (Figure 4.1). Although numerous models have been proposed that can

achieve this behavior (see for example [85]), we have selected a system that includes three resistors, two capacitors, and two inductors. Amongst other candidate configurations, this form best represents the impedance spectrum of the brachial artery while presenting a realistic physical incubator-based system with tunable parameters [86,87,204]. An additional advantage is realized when frequency limits are tested analytically in order to reduce the number of variables.

In this circuit design we include both inherent, or systemic, (s) values of components and those added (a) by individual design elements. A pictorial representation of the electrical circuit with corresponding hydraulic elements is shown in Figure 4.2. The systemic and added downstream resistances are in series so that $R_1 = R_s + R_a$. Likewise, the value of the two compliances in parallel are additive so that we can reduce these to a single value $C = C_s + C_a$. Thus, the overall system reduces to only 5-elements.

The equivalent impedances of the resistor-capacitor-inductor and resistor-inductor sub-circuits of the theoretical impedance (denoted with a hat) circuit are

$$\hat{Z}_{eq1} = \frac{Z_C\left(Z_{R1} + Z_{Ls}\right)}{Z_C + \left(Z_{R1} + Z_{Ls}\right)}, \qquad \hat{Z}_{eq2} = \frac{Z_{R2}Z_{La}}{Z_{R2} + Z_{La}} \qquad [4.7]$$

We get from summation of these impedances the total theoretical impedance of the incubator based-system

$$\hat{Z}(\omega) = \frac{-j\left(R_1 + j\omega L_s\right)}{-j + R_1\omega C + j\omega^2 L_s C} + \frac{j\omega L_a R_2}{j\omega L_a + R_2}, \qquad [4.8]$$

with real and imaginary parts

$$\Re\left\{\hat{Z}(\omega)\right\} = \frac{\omega^2 L_s R_1 C}{R_1^2\omega^2 C + \left(\omega^2 L_s C - 1\right)^2} - \frac{R_1\left(\omega^2 L_s C - 1\right)}{R_1^2\omega^2 C^2 + \left(\omega^2 L_s C - 1\right)^2} + \frac{\omega^2 L_a^2 R_2}{R_2^2 + \omega^2 L_a^2}$$
$$\Im\left\{\hat{Z}(\omega)\right\} = -\frac{R_2\omega C}{R_1^2\omega^2 C^2 + \left(\omega^2 L_s C - 1\right)^2} - \frac{\omega L_1\left(\omega^2 L_s C - 1\right)}{R_1^2\omega^2 C^2 + \left(\omega^2 L_s C - 1\right)^2} + \frac{\omega L_a^2 R_2^2}{R_2^2 + \omega^2 L_a^2} \quad . \quad [4.9]$$

In a similar fashion to [4.3]-[4.5] the magnitude and phase at each frequency are calculated from

$$\left|\hat{Z}(\omega)\right| = \sqrt{\left(\Re\left\{\hat{Z}(\omega)\right\}\right)^2 + \left(\Im\left\{\hat{Z}(\omega)\right\}\right)^2}, \qquad \angle\hat{Z}(\omega) = \tan^{-1}\left(\frac{\Im\left\{\hat{Z}(\omega)\right\}}{\Re\left\{\hat{Z}(\omega)\right\}}\right). \quad [4.10]$$

Although the values of R_s, C_s, and L_s were required by the physical demands of the culture hardware configuration (e.g., length/compliance of tubing, fittings, etc), the variables R_1 (by virtue of R_a), R_2, C (by virtue of C_a), and L_a of equation [4.8] were chosen in order to minimize the difference between the desired [4.5] and theoretical [4.10] impedances. A parameter sensitivity study was performed to determine the range of applicable values for these variables that result in a stable solution.

Further restrictions on [4.8] help to simplify the possible values in the design of the system. Here we take the limit as ω approaches steady state and infinity,

$$\lim_{\omega\to 0}\hat{Z}(\omega) = Z(0) = R_1 \quad \text{and} \quad \lim_{\omega\to\infty}\hat{Z}(\omega) = Z(\infty) = R_2, \qquad [4.11]$$

and we see that values of both R_1 and R_2 can be found directly from the measured impedance magnitude leaving only C and L to be determined via regression. We can also see that

$$\lim_{\omega\to 0}\angle\hat{Z}(\omega) = \lim_{\omega\to\infty}\angle\hat{Z}(\omega) = 0 \qquad [4.12]$$

Although [4.12] does not provide any further information towards the value of the design elements, it does suggest that the desired impedance phase (Figure 4.1) can match that illustrated by the 5-element electro-hydraulic analogy (Figure 2 and Figure 3).

A weighted residual sum of squares error between the magnitude and phase of the desired and theoretical impedances results in the fitting of the remaining two parameters (C and L) [85],

$$\Omega = \sum_{k=1}^{N} \left\{ \frac{\left(\left| Z(\omega_k) \right| - \left| \hat{Z}(\omega_k) \right| \right)^2}{\left| Z(\omega_k) \right|^2} + \frac{\left(\angle Z(\omega_k) - \angle \hat{Z}(\omega_k) \right)^2}{\angle Z(\omega_k)^2} \right\} \qquad [4.13]$$

The least-squared minimization is performed in MATLAB where upper and lower bounds were based on the theoretically optimal or realistic physical system suited for prolonged tissue culture as illustrated in the following section.

4.3.4 Calibration and Implementation of the Physical System

The physical system is schematically illustrated in Figure 4.4. Resistance is defined as the pressure drop Δp_R across an element at a given volumetric flow rate q_R ,

$$R = \frac{\Delta p_R}{q_R} \qquad [4.14]$$

The values of the systemic and added resistances of our device were measured in isolation and calculated from [4.14] (Figure 4.5 a-b) noting that $R_s > 0$, $R_a \geq 0$, and $R_2 \geq 0$. Except where otherwise noted, our design used 0.64 cm inner diameter Masterflex PharMed BPT tubing (Cole-Parmer, Vernon Hills IL) and biologically inert tube fittings. Using a Poiseuille relation that assumes a circular cross-sectional area, the steady, laminar flow resistance can be approximated by

$$R = \frac{8\mu_R}{\pi r_R^4} \qquad [4.15]$$

with $_R$ the length of the resistive element, μ, the dynamic viscosity of the media, and r_R the inner radius of the resistor. For the most part, equation [4.15] provided guidance only in the gross design of the system while the accuracy of the equation depends on how closely the physical conditions match the set of assumptions. Maintaining laminar flow, for example, is important to the linearity of R but as a pinch valve closes, the Reynolds number increases towards turbulence thresholds. To overcome this, a custom designed, elongated "plate" (linearized) valve was created to uniformly compress a greater length of tubing (roughly 60 cm) so that resistance can be increased to a while maintaining laminar flow. The results of this custom design are illustrated in Figure 4.5a for the added resistor R_a. In contrast, a standard adjustable tubing pinch valve (Cole-Parmer, Vernon Hills IL) was used for R_2 since its contributions to the total circuit were small. The flow-resistance relationship for a standard pinch valve is also illustrated in Figure 4.5b.

Similarly, the compliance is related to the flow and the pressure gradient via

$$C = \frac{q_C}{dp_C/dt} = \frac{dV_C}{dp_C}, \qquad [4.16]$$

where dV is the change in volume of the compliant element for a given change in pressure. Two compliances in parallel form the total compliance, where $C_s > 0$ due to the elasticity of the PharMed tubing. Furthermore $0 \le C_a \le (\Delta V_a/\Delta p)$ where V_a is the volume of air in the compliance chamber. The relationship between the value of the added compliance and the volume of air initially in the compliance chamber can be calculated from the ideal gas law under isothermal conditions. The compliance chamber consisted of a 60 ml Luer lock

syringe (Becton Dickinson Co., Franklin Lakes, NJ) preloaded with a volume of air that was held in position using standard adjustable lab-stand grips.

From a momentum balance on an element of fluid, the inertance describes the property of a fluid that impedes changes in flowrate so that

$$L = \frac{\Delta p_L}{dq_L/dt} = \rho \frac{L}{\pi r_L^2}, \qquad [4.17]$$

where ρ is the density of the fluid, $_L$ the length of the inductor, and r_L the inner radius. In our initial system L_s 0 and $L_a \geq 0$ (Figure 4.5d) illustrating the importance of including systemic inductances in the overall design. The added inductance L_a was created using a 0.64 cm inner diameter coil of tubing up to 155 cm long.

A 0.32 ml/rev stainless steel gear pump (Micropump Inc., Vancouver WA) with 0-5V DC speed controlled electromagnetic drive provided steady flow of culture media up to 30 ml/s. A custom fabricated pulsatile pump consisting of a Masterflex L/S 600 RPM digital drive was connected to a Masterflex Easy Load pump heads with 3 stainless steel rollers each (Cole-Parmer, Vernon Hills IL) generate flow through a pulse circuit (Figure 4.4). Two additional roller pump heads were connected via 0.2" pitch trapezoidal tooth urethane timing belts (McMaster-Carr, Atlanta GA) and timing belt pulleys with 20, 30, and 40 teeth. The first pulley-gear set resulted in a 2:1 driving-to-driven gear ratio and the second gear set a 3:2 ratio thereby generating frequencies that include the fundamental, first, and second harmonics (Figure 4.6). With three rollers per pump head, the digital pump drive frequency was set to 1/3 the fundamental frequency. Ignoring edge effects and assuming a negligible tube thickness, the pulse volume Ψ from the roller pump and resultant volumetric flow rate magnitude were calculated from

$$\Psi = \frac{\pi d_t^2}{4}\,_t, \qquad |Q| = 2\pi\frac{\Psi}{\omega}, \qquad [4.18]$$

where d_t is the tubing inner diameter and $_t$ the length between rollers (2 cm). Assorted diameters of Masterflex PharMed BPT tubing were used in the roller pump heads to meet the volumetric flow requirements. A camming mechanism, once disengaged, allowed for detensioning of the timing belt permitting free rotation of the harmonic channels. The harmonic channel phases were then set by aligning a single roller of that channel with a roller of the fundamental frequency and advancing, or retarding, the phase to match the desired phase angle. Using this approach phase angles were found to be ±10% of the desired value.

4.3.5 Data Acquisitions

Volumetric flow and pressure were measured using an Atrato 710 series ultrasonic liquid flow meter (Titan Enterprises, Sherborne UK) with 0.18 sec integration window and a PX309 stainless steel amplified pressure transducer (Omega Engineering Inc., Norwalk CT) respectively. Both flow and pressure values were digitized using a NI-DAQ USB 6009 data acquisition system (National Instruments; Austin TX) and recorded using a LabView-based program at a sampling rate of 125 Hz.

4.3.6 Tissue Procurement and Media Perfusion

Great saphenous veins (GSVs) were harvested from freshly slaughtered 200kg, 3 years-old American Yorkshire Pigs at the local abattoir. All animals used in this study were sacrificed for the primary purpose of food consumption and were not subject to Animal Care and Use Committee (IACUC) approval. Tissues were then transported in sterile Moscona's saline solution to the lab where they were immediately attached to the large glass cannula of the bioreactor using sterilized braided silk suture. Dulbecco's Modified

Eagle Media (ThermoFisher Scientific, Waltham MA) with phenyl red was supplemented with 10% fetal bovine serum, 1% penicillin/streptomycin, 1% amphotericin-B, and 1% gentamicin. The bioreactor and media were then maintained at a constant 37 deg C and gas exchange performed at filtered ports. All vascular perfusion experiments were performed for 6 h.

4.3.7 Gene Expression Analysis

Expression of mRNA for seven remodeling-associated genes relative to β-actin (F: AGGCCAACCGTGAGAAGATG, R: CCCATCCCCAGAGTCCATGA) were quantified through quantitative real-time polymerase chain reaction (qPCR): Col 3 (F: GCGGTGACAAAGGTGAAACC, R: GGCTACCTACTGCACCTTGG), FN 1 (F: TGGGGATACCTGGAGCAAGA, R: GCCTCTCACACTTCCACTCC), PAI 1 (F: CCTAACCAGGCGGACTTCTC, R: CATGCGGGCTGAGACGATAA), VCAM 1 (F: CGCTGGTCATGAATCCCGTT, R: ATCTCTGGGTCCTTGGGGAA), MMP 2 (F: CCTGATCTGGACCCCGAAAC, R: TATCCATCTCCGTGCTCCCA), TGFβ 1 (F: CTAATGGTGGAAAGCGGCAA, R: CCCGAGAGAGCAATACAGGTT), TIMP 1 (F: CACCTGCAGTTTTGTGGCTC, R: GGGATGGATGTGCAGGGAAA). Vessels were snap frozen on dry ice and stored at -80 C either immediately after dissection or at the completion of ex vivo culture. Frozen tissues were homogenized using a Qiagen TissueRuptor (Qiagen, Hilden, Germany), immediately followed by total mRNA isolation with a Qiagen RNeasy Fibrous Tissue Mini Kit (Qiagen, Hilden, Germany). After total mRNA quantification using an Implen Nanophotometer Pearl (Implen, Munich, Germany), 500ng mRNA was converted to cDNA via an iScript cDNA Synthesis Kit (Bio-Rad, Hercules, CA). qPCR assays were then run using the genes listed above on a Bio-Rad CFX

Connect Real-Time System (Bio-Rad, Hercules, CA) using Fast SYBR Green Master Mix (Applied Biosystems, Foster City, CA). Wells within plates were triplicated, each plate configuration was run three times, and threshold values were set at a consistent value of 300 RFU. Relative gene expression was calculated using the $\Delta\Delta C_T$ method with GSV flow conditions being the reference samples. All cDNA samples were validated by end-point PCR using PuReTaq Ready-To-Go PCR beads (GE Healthcare, Buckinghamshire, UK) and gel electrophoresis.

4.3.8 Statistical Analysis of Gene Expression

For each combination of gene and experimental condition (e.g., GSV Col 3), reported data represent an average of n=27 data points (n=3 samples, n=3 plates, n=3 wells/plate) except for outliers, which were discarded, for both the gene of interest and β-actin. Error bars reflect the standard error of the mean for all included data points. Two-tailed Student's t-tests ($p < 0.05$) were conducted both between GSV-BrA and GSV-LCA samples.

4.4 RESULTS

The BrA pressure and flow waveforms were digitized using the ImageJ (NIH) "Figure Calibration" plugin and the MATLAB Fast Fourier Transform (FFT) command used to identify the magnitude and phase for the steady, fundamental, and harmonics of the periodic signals (Table 4.1). Figure 4.1 iillustrates the time and frequency domain relationships between pressure and flow in a BrA. The BrA has an impedance magnitude that decreases with frequency and, by virtue of the negative phase angle at low frequencies, flow leads the pressure. LCA and GSV pressure and flow waveforms were also digitized in a similar manner to the BrA.

The decreasing impedance magnitude and negative phase angle of the BrA provided guidance for the form of the elector-hydraulic analogy and bench-top impedance configuration. Here, a 5-element model was found to best represent both the BrA impedance and a realistic incubator-based setup (Figure 4.2). Comparisons to other model configurations are otherwise omitted for brevity. The form of this configuration enables a direct calculation of R_1 and R_2 (equation [4.11]), leaving only C and L to be estimated via regression. However, to determine the breadth of application for this model, a parameter sensitivity study was also performed as illustrated in Figure 4.3.

The physical system, first represented by the electrohydraulic analogy (Figure 4.2), is realized diagrammatically in Figure 4.4. The nominal system resistance was slightly nonlinear (i.e., a line with nonzero slope in the R vs. q plot) with a maximum value of 6.7 mmHg·s/ml for the range of volumetric flows tested during calibration (triangles – Figure 4.5a). The value of R was comparatively low so that the majority of the desired resistance was still generated by the valve and not systemically. The plate (linearized) valve demonstrated a nearly linear resistance that increases with decreasing orifice area (Figure 4.5a). In contrast, the standard pinch valve demonstrates an extensive nonlinearity with decreasing orifice area (Figure 4.5b). The valve's rotational position θ, was used as a qualitative descriptor that relates to the orifice area but this exact relationship was not solved directly.

The systemic compliance was found to be constant at C_s =0.0059 ml/mmHg up to 300 mmHg for the nominal length of tubing, =144 cm (Figure 4.5c) and increases to C_s =0.010 ml/mmHg when the tubing length was doubled (data not shown). Thus system compliance has a nearly linear relationship with the length of tubing. Likewise, the

compliance chamber was capable of generating tunable compliance levels up to C_a=0.07 ml/mmHg for volumes up to 60 ml. The experimentally measured values generated by the compliance chamber (around a 100 mmHg operating point) were similar to those determined using the ideal gas law. Further, the average system inductance was found to be L_s=0.363±0.103 mmHg·s^2/ml for frequencies ranging from 4.73 to 15.8 rad/s. This experimental value was similar to the theoretical value (L_s=0.336 mmHg·s^2/ml) for the systemic length and diameter of tubing ($_L$ =144 cm, r_L=0.32 cm). We note that compliant tubing was used in the estimation of inductances thus the true value may be augmented in a rigid tubing system. Added inertance was achieved through the selection of inertance tubing diameter at lengths up to 155 cm. Furthermore, the pulsatile pump (Figure 4.6) was able to generate fundamental and harmonic frequencies of pulse generation with little drift over the duration of experimentation. Small errors in flow occurred when the difference between the desired and actual tubing diameters were large. Still, volumetric flow rates were near the desired values (Figure 4.7 and Figure 4.8).

All systemic values of the electro-hydraulic analogy, R_s, C_s, L_s, were fixed in the regression model of impedance matching while the added values, R_a, R_2, C_a, L_a, were bound only by the physical limitations of the system as described in the methods section (Table 4.2). These restrictions were necessary to create a practical device aimed at long-term perfusion culture of living tissue. The resulting error between the desired impedance and the theoretical and measured impedance magnitude and phase are illustrated in Figure 4.7 c,d. The error between the desired and theoretical impedances were low in the BrA (RSS=0.012), negligible in the GsV, but high in the LCA (RSS=0.884). The high error was due to the initial positive phase of the impedance function for which the 5-element circuit

was not capable of recreating. That notwithstanding, the circuit recreated well the shape of the pressure waveform once shifted by roughly 0.2 seconds.

Gene expression profiles for freshly isolated GSVs exposed to GSV, LCA, or BrA waveforms for 6 h are illustrated in Figure 4.9. Compared to vessels exposed to GSV-like waveforms, those experiencing BrA conditions had statistically significant expression of all measured genes ($p<0.02$), except VCAM 1. In contrast, differences were only found in MMP 2 ($p=0.036$), FN 1 ($p=0.001$), and TIMP 1 ($p=0.033$) gene expression when comparing vessels exposed to GSV waveforms to those experiencing LCA-like waveforms. PAI 1 was the only gene that was found to be differentially expressed by vessels exposed to BrA-like conditions compared to LCA conditions ($p=0.008$). However, PAI 1 ($p=0.002$), VCAM 1 ($p<0.001$), and TGFB 1 ($p=0.002$) were all found to be statistically significant when comparing acute gene expression levels of freshly isolated tissues to those exposed to in situ loading conditions in the bioreactor (Figure 4.10). Although all samples tested here were studied after 6 h for the purposes of isolating the effects of specific waveforms, perfused vessels have been maintained in our culture system for up to 3 weeks with viability assed using vasoreactants and metabolic assays (data not shown).

4.5 DISCUSSION

Hemodynamic studies of the last 45 years have provided a wealth of information that can be used as a target for the design of modern vascular tissue culture systems. In our present work, a Fourier series representation of simultaneously recorded brachial artery blood pressure and flow waveforms from the classic study of Gault and colleagues was used to guide the design of an in vitro culture system [1]. From this data the desired

impedance magnitude and phase were estimated in the frequency domain and a 5-element electro-hydraulic analogy consisting of resistors, capacitors, and inductors implemented [85]. The chosen configuration represents the data well while serving as a guide towards the design of implementable hardware elements. Our semi-distributed elemental design considers separately the inherent, but significant, contribution of the systemic properties of our culture hardware to the total hydraulic circuit from those desired properties contributed by the added elements. The remaining coefficients of the electro-hydraulic model were then found by minimizing the error between the desired and theoretic impedances. Thus, a biomimetic impedance matching system was developed that takes into consideration real-world hardware configurations. The physical system was built using tissue-culture ready components, and the capacity of this device to recreate physiological waveforms evaluated. As proof of concept, qPCR was performed on freshly harvested saphenous vein segments under the brachial artery conditions and compared to coronary-like, and venous (in situ) media dynamics for 6 h. The relative gene expression for each of these cases were then analyzed and compared for the arterial or venous waveforms.

Vascular impedance is a convenient tool in the analysis of in vivo hemodynamics [192]. The design of a number of pulsatile bioreactors have included resistive, capacitive, and inductive elements in the hydraulic analogy; however, few systems have translated the electro-hydraulic impedance approach into in vitro systems [44,84,96,99,185,197–201]. The work of Kung and Taylor provided a framework for the recreation of the vascular hemodynamics using customized impedance modules in a bench top system [92]. The advantage to their, and thus our, approach is that the analysis can be performed in the frequency domain, facilitating subsequent delineation of the phasic relationships towards

the waveforms desired to effect tissue remodeling. Moreover, the design elements can be bounded within physically obtainable values while incorporating the inherent contribution of systemic elements. Ours however, is the first study of its kind to test gene expression using the impedance matching approach for a brachial artery and to compare vessels exposed to multiple vascular waveforms. This approach permits future investigations to isolate and delineate specific media pressure and flow wave components to ascertain what is fundamental in the design of vascular perfusion studies. Another advantage is the scalability of our system in terms of both size and cardiac frequency. The capacity to include higher biomimetics from species with accelerated heart rates (e.g., rodent models) is readily adaptable into our design approach thus providing an opportunity to study numerous transgenic models of vascular disease while isolating conditions of interest.

Fundamental to the design of our perfusion bioreactor was the seamless transition from the theoretical to physical hardware while maintaining a sterile environment. In general, we sought the fewest possible elements and for those elements to be maintained in the simplest configuration. Clearly a tradeoff exists between the complexity of a culture system and its ability to recreate in vivo conditions. Through the electrohydraulic analogy, 2, 3, and 4 elemental systems, of varying configurations, were also simulated in order to find the best configuration to represent in vivo and in vitro data. An interested reader can refer to Yoshigi et al. for a general description of these models [85]. However, to mimic the desired impedance spectrum while recreating a reasonable incubator-based configuration, the 5-element electrohydraulic analogy described herein was the best fit and a parameter sensitivity study performed around a stable equilibrium point. In fact, our hardware was readily capable of matching the desired BrA and GSV waveforms. On the

other hand, the desired values of LCA waveforms were positive in phase at the fundamental frequency (Figure 4.8c-d). Such behavior is not capable of being replicated with the current setup. Instead we recreated the pressure and flow waveforms that were out of phase with their desired waveforms for the LCA, but precise in both shape and magnitude.

The unique pulsatile pump in our culture system consists of discrete channels of roller heads so that pulsatility can be gradually added without risking contamination (e.g., transitioning from a venous to arterial-like fluid dynamics). The pump design was motivated by a literal interpretation of the Fourier series approach to hemodynamic waveform analysis whereby volumetric flow can be broken down into individual sinusoids. In similar fashion, all resistances were adjustable without exposing the culture media to contamination. Still certain nominal, or "system" properties were created through the connectivity of such a culture system. In many models, such properties would be lumped together. However, we found that distributing the inherent system parameters from the added ones enabled a more realistic approach to the overall system design while allowing for calibration and refinement of these individual elements. In terms of both compliance and inductance the nominal values of these parameters were significant and could not be neglected in the overall design. For example, the system compliance that results from elasticity of the tubing was so high (C_s =0.005 ml/mmHg) that no additional compliance from the compliance chamber was needed. Retrospectively the compliance of the system could be reduced by selection of more rigid tubing and is a consideration of future work. The measured system inertance was also large (L_s =0.363±0.103 mmHg·s^2/ml) even after tubing diameters were increased to keep this value low. Thus the 5-element design that included systemic values of inductance and compliance were instrumental in the

experimental outcome.

The GSV was chosen as a conduit to study gene expression due to its prevalence in coronary and peripheral artery bypass grafting. Although this vessel has similar inner diameters to the coronary and brachial arteries, the pressure and flow was significantly higher in the arterial system while little to no pulsatility present in the saphenous vein under in situ conditions. At similar diameters, the higher flow conditions would proportionally increase luminal shear stress. In fact, we observed an acute vasomotor response, in terms of caliber reduction, when vessels were mounted to our system but prior to the initiation of flow. From the contemporary literature, one would expect altered expression of many mechanically sensitive genes when comparing arterial to venous pressure and flow conditions. In fact, almost all of the genes studied were differentially expressed using arterial-like waveforms when compared to venous ones. Interestingly, only PAI 1 was affected when comparing GSVs exposed to LCA conditions compared to GSVs exposed to BrA waveforms. PA I 1 has been implicated in a variety of remodeling processes [177,206,208] and been shown to increase in response to elevated shear stress and pressure [52,96]. Since the BrA and LCA waveforms were similar, it is not surprising to note that PAI 1, expressed by both endothelial and smooth muscle cells, was the only differentially expressed gene within arterial waveforms.

It was observed, however that when comparing the gene expression of freshly isolated GSVs to those under replicated in situ conditions in 6 h of culture, PAI 1 was the most dramatically affected gene followed by VCAM 1 and TGFβ 1. Various other genes appeared to be different without reaching statistical significance. Collectively this data suggests that gene expression was nominally affected by the culturing processes. The

extent towards which such a condition significantly influences the results remains to be discovered. However, it is important to consider that all of the other gene expression analyses were performed on tissues exposed to similar conditions except altered media fluid dynamics. Although not the subject of the current manuscript, ongoing long-term studies (>3 wks) will be able to report on the resultant protein composition of these studies. Viability of those cultures have been successfully confirmed through administration of endothelial and smooth muscle dependent vasoreactants and a colorimetric metabolic activity assay. Our studies at 6h were sufficiently long so that the effects of dissection and excision under static conditions would be ameliorated by the culture but short enough so that histological morphological changes did not occur.

The contributions of each harmonic of pressure and flow to the overall waveform diminish at higher harmonics with 95% of the energy contained in the first 5 harmonics [209]. While it is clear and widely accepted that pressure and flow exert some effect over blood vessel morphology, the prevailing challenge is determining what extent the subtler characteristics such as higher harmonics, pressure-flow phase differences, and rate of change in these quantities drive remodeling behavior. While this study provides some guidance into the underlying requirements in the design of vascular bioreactors, for the time being significant evidence points, at the least, towards an inclusion of the fundamental frequency components of pressure and flow pulsatility during *in vitro* culture. There exists a need for careful experimentation where these subtle influences can be discovered.

4.6 ACKNOWLEDGMENTS

The authors would like to acknowledge the contributions of undergraduate researcher Shahd Hasanian for her assistance with the gene expression studies. This

research was supported by NIH grant R21EB022131 (JFE)

4.7 TABLES

Table 4.1 – Magnitude and phase of simultaneously recorded blood pressure and flow waveforms from the literature [1–3], which illustrates the desired steady, fundamental, and first two harmonics of the Brachial Artery (BrA), Greater Saphenous Vein (GSV), and Left Coronary Artery (LCA).

	k	ω (rad/s)	$\lvert P \rvert$ (mmHg)	$\angle P$ (rad)	$\lvert Q \rvert$ (ml/s)	$\angle Q$ (rad)
BrA (Human)	0	0	90.1	0	1.68	0
	1	6.21	19.9	-1.52	0.74	-0.91
	2	12.4	13.6	-2.26	0.62	-1.07
	3	18.6	6.26	-3.05	0.56	-1.84
GSV (Human)	0	-	15.0	-	0.17	-
	1	-	-	-	-	-
	2	-	-	-	-	-
	3	-	-	-	-	-
LCA (Human)	0	0	101	0	0.94	0
	1	8.94	16.1	2.64	0.43	3.04
	2	17.9	5.66	-0.18	0.18	0.12
	3	26.8	5.65	-2.97	0.17	-2.05

Table 4.2 – Parameters of the 5-element electro-hydraulic model when bounded by practical values and the cumulative fitting error.

	$R_1\left(\frac{mmHg \cdot s}{ml}\right)$	$R_2\left(\frac{mmHg \cdot s}{ml}\right)$	$C\left(\frac{ml}{mmHg}\right)$	$L_s\left(\frac{mmHg \cdot s^2}{ml}\right)$	$L_a\left(\frac{mmHg \cdot s^2}{ml}\right)$	RSS
BrA	53.59	9.370	0.005	0.331	0.126	0.012
GSV	88.23	-	-	-	-	-
LCA	106.8	3.944	0.005	0.331	0.361	0.884

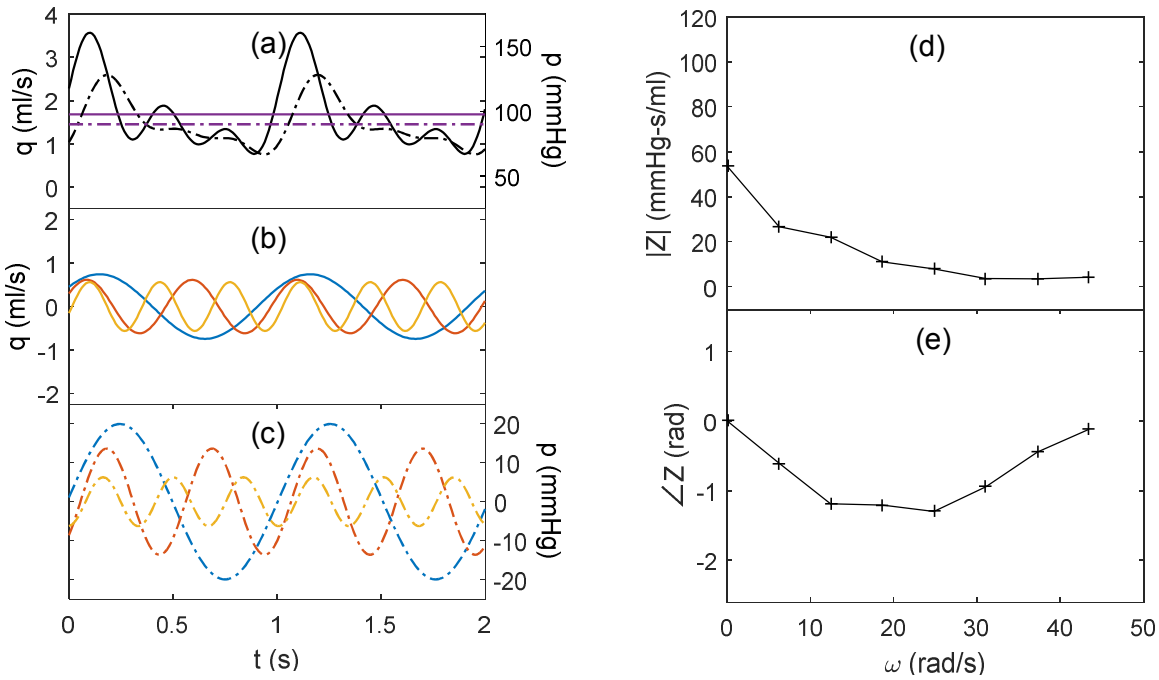

Figure 4.1 – Visualization of Fourier analysis illustrating (a) the steady (purple) and composite (black) waveforms of volumetric blood flow (solid) and blood pressure (dash-dot) of the Brachial Artery (BrA). The fundamental (blue) and first two harmonics (orange; red) are shown for the (b) volumetric blood flow rate and (c) blood pressure while. The impedance (d) magnitude and (e) phase for the BrA.

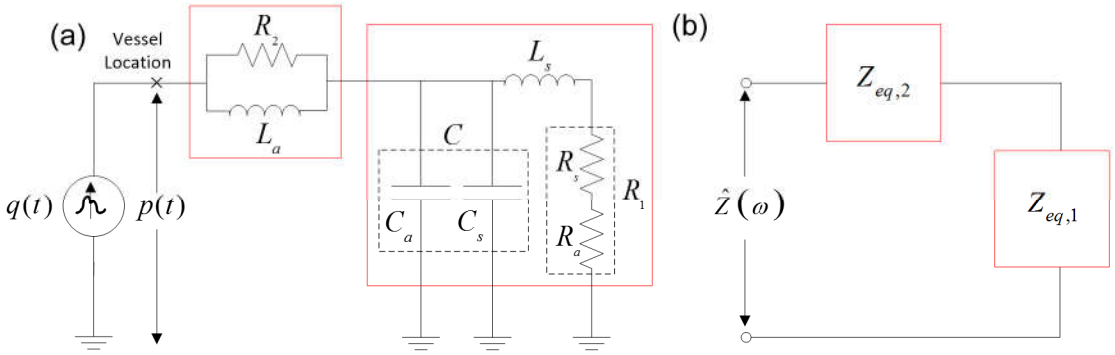

Figure 4.2 – (a) Electro-hydraulic analog of the cardiovascular system and bench top schematic with (b) equivalent impedances.

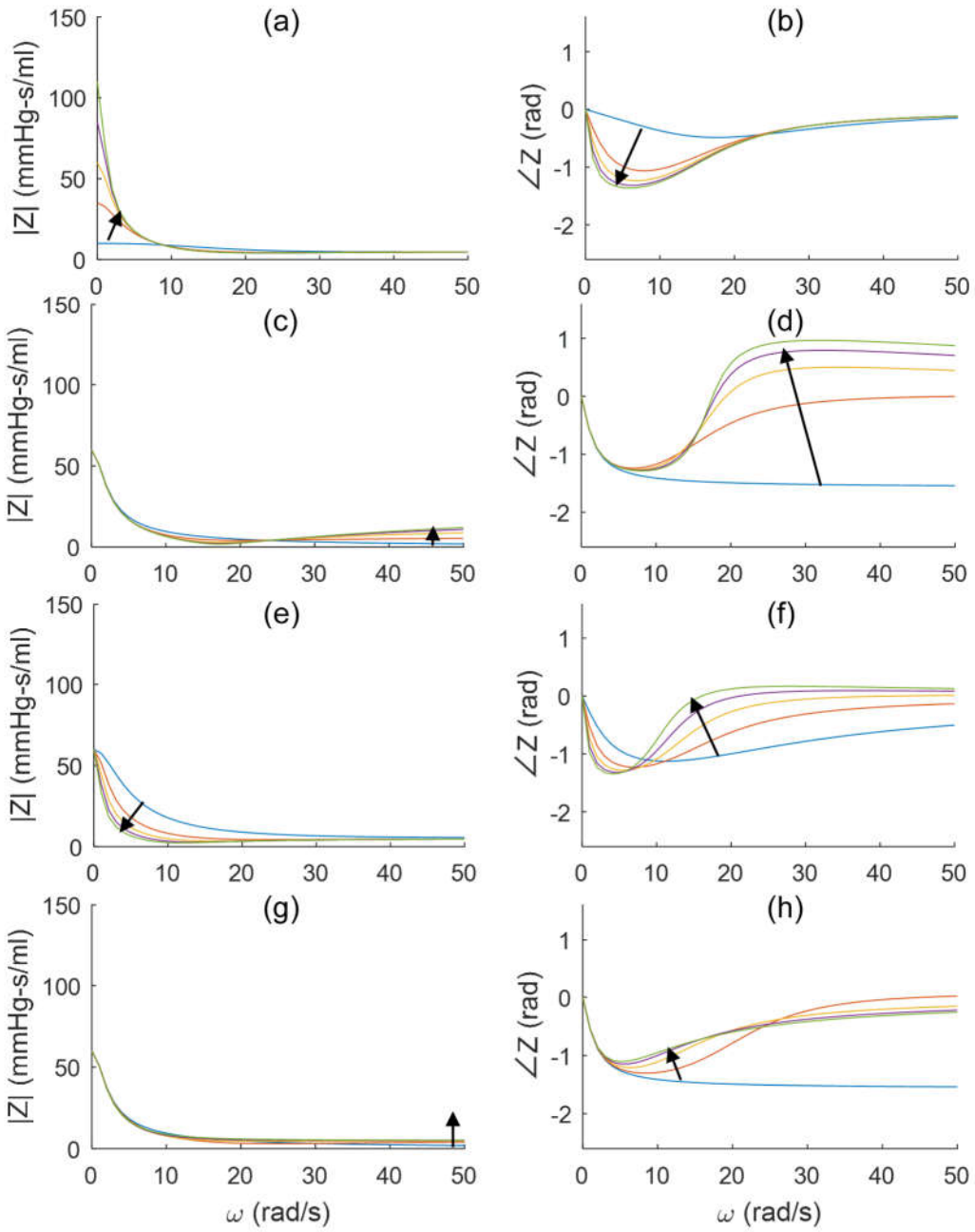

Figure 4.3 – . Parameter sensitivity of the 5-element electrohydraulic analog demonstrating impedance magnitude (left) and phase (right). (a-b) $R_1 \in [10,110]$ (mmHg·s/ml), (c-d) $R_2 \in [0,24]$, (e-f) $C \in [0.005, 0.025]$ (ml/mmHg), and (g-h) $L_a \in [0, 0.8]$ (mmHg·s^2/ml). Default values of R_1 =60 (mmHg·s/ml), R_2 =5 (mmHg·s/ml), C =0.01 (ml/mmHg), L_a =0.33 (mmHg·s^2/ml), and L_s =0.33 (mmHg·s^2/ml). Arrows indicate the direction of increasing values of the given parameter.

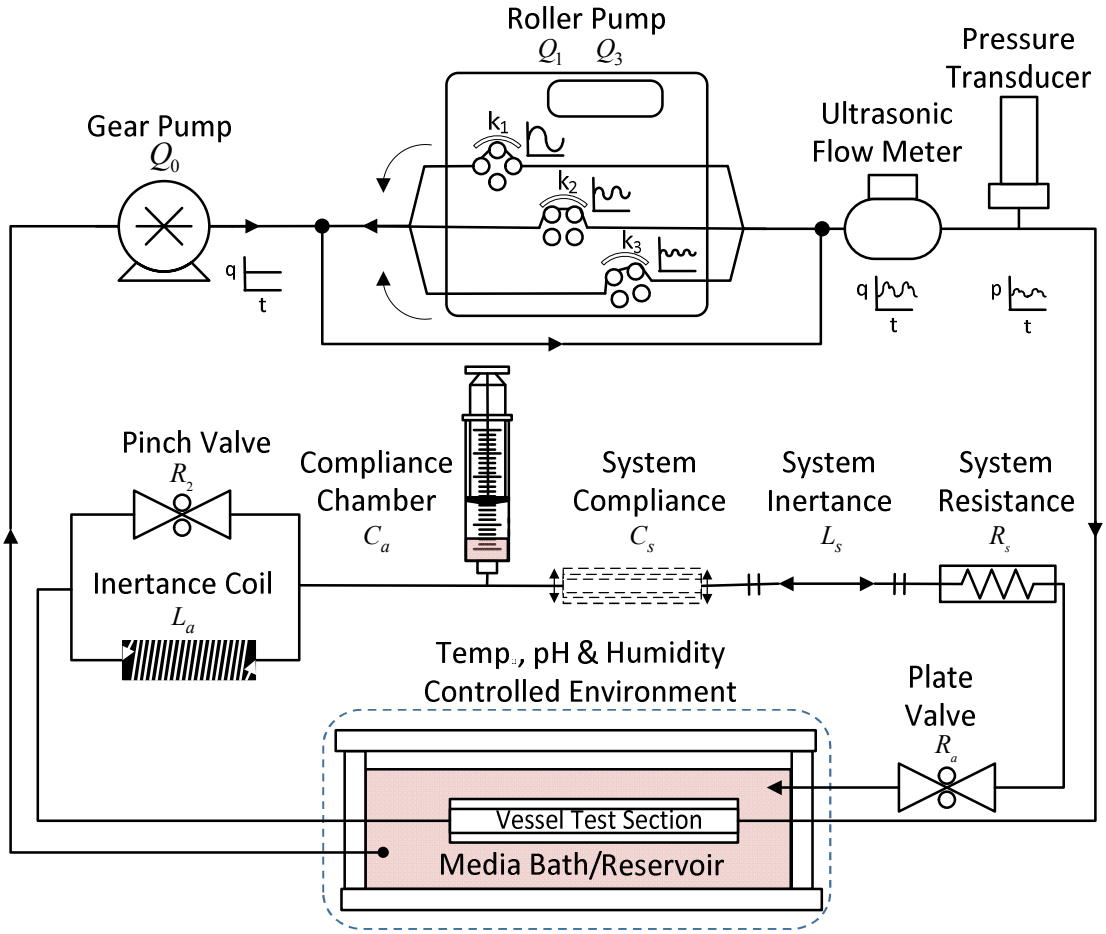

Figure 4.4 – Hardware schematic for the pulsatile perfusion bioreactor.

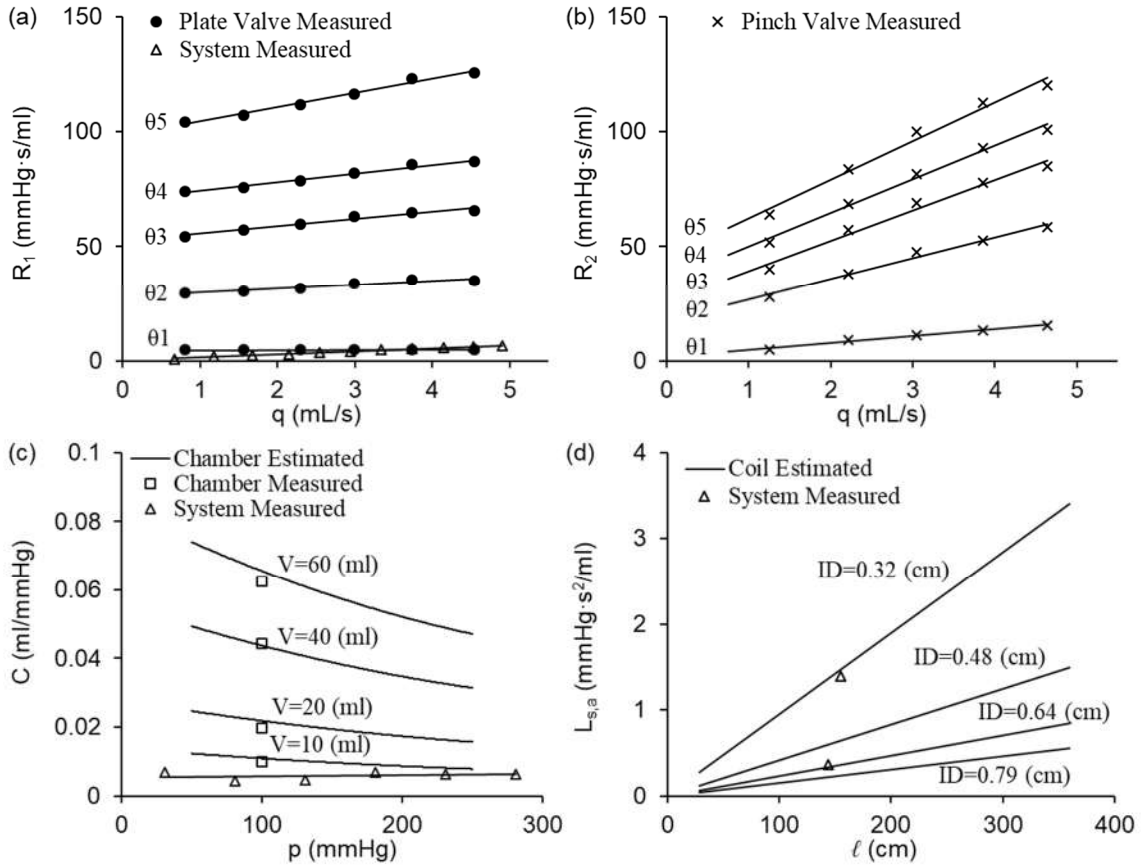

Figure 4.5 – Values of isolated design elements in the pulsatile perfusion bioreactor: (a) measured systemic resistance and the resistances at discrete positions of a custom designed plate (linearized) valve and (b) resistances at discrete positions of the tubing pinch valve, (c) measured systemic compliance and measured versus estimated added compliance using chamber with different preload volumes of air. (d) Measured systemic inductance and added inductances from a coil of tubing using different tubing diameters.

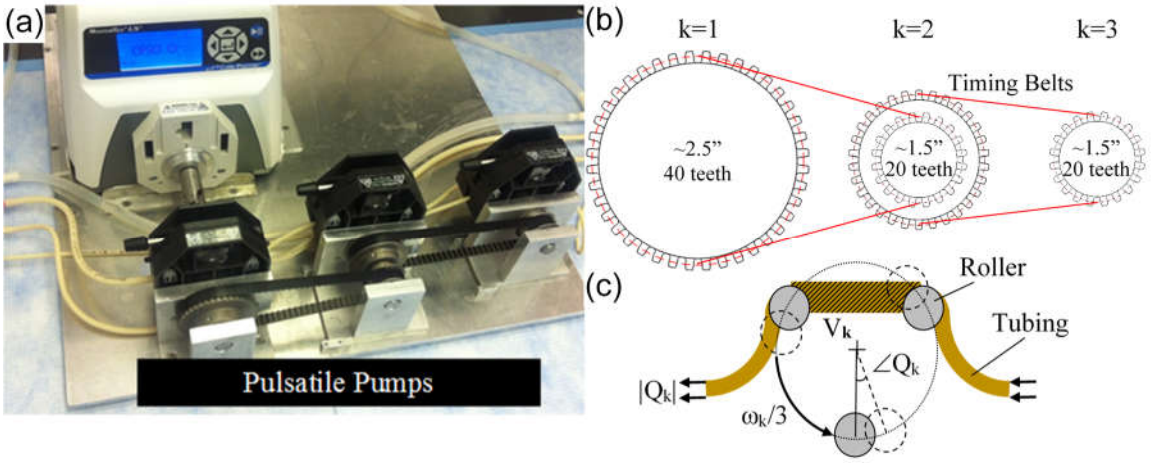

Figure 4.6 – (a) Customized three channel peristaltic pump with (b) synchronous gearing system and timing belts that generate the fundamental (k=1) and first two harmonics (k=2, 3) of the frequency. (c) Illustration of a single roller pump head containing three rollers where the volumetric flow phase angle is set using a cam mechanism and the displaced volume adjusted by using tubing with different lumen diameters.

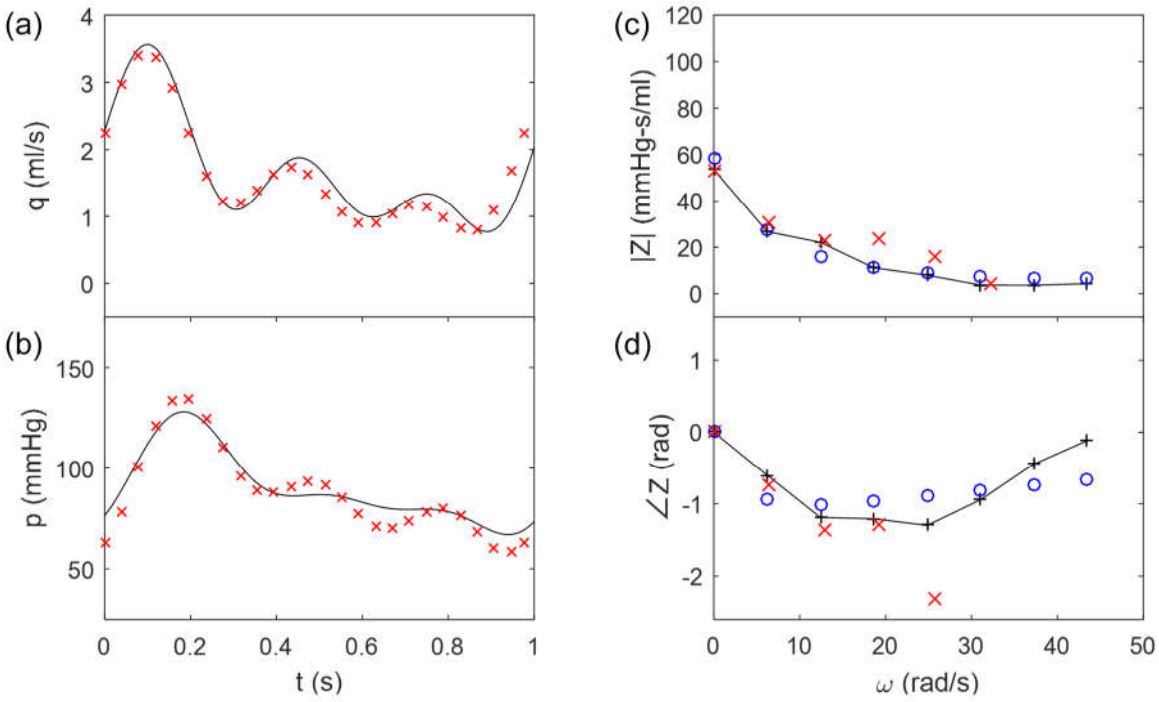

Figure 4.7 – Simultaneous brachial artery (BrA) (a) volumetric blood flow rate and (b) blood pressure for one cardiac cycle. Solid lines indicate the desired waveform and (×) the values recorded in our bioreactor system. (c) The impedance modulus and (d) phase for the desired (+), theoretical (○), and measured response (×).

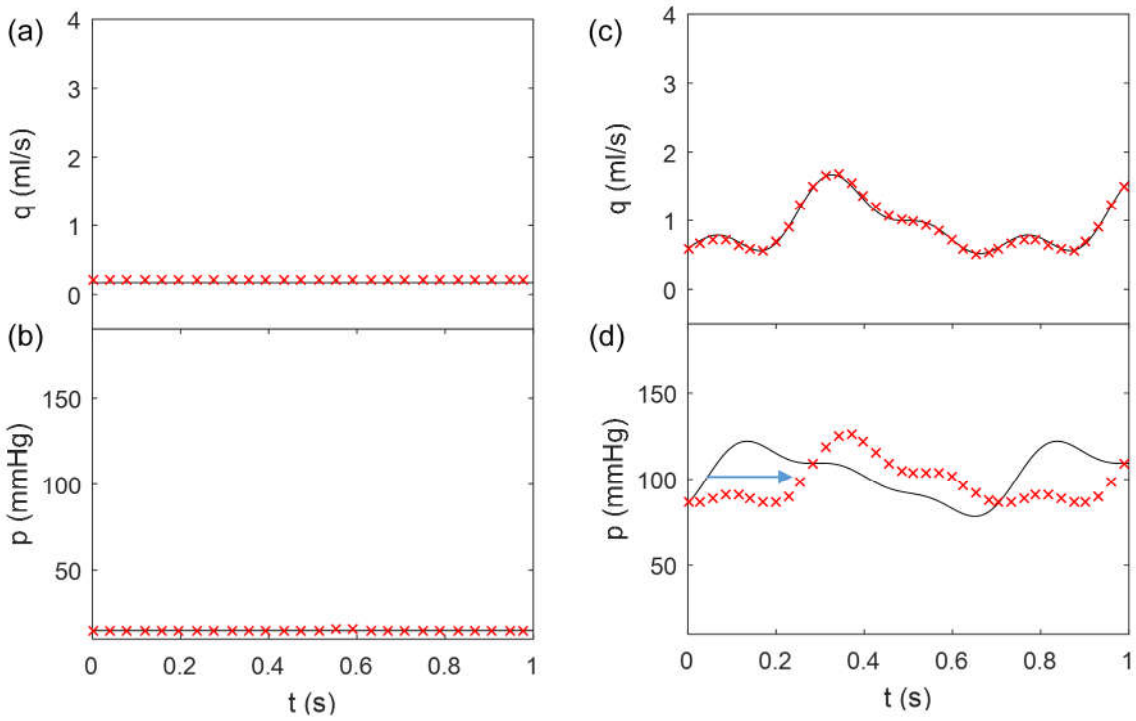

Figure 4.8 – Simultaneous (a-b) greater saphenous vein (GSV) and left anterior descending coronary artery (LCA) (c-d) volumetric blood flow rate and pressure for one cardiac cycle. Solid lines indicate the desired waveform and (×) the values recorded in our bioreactor system. The arrow indicates the shifted coronary artery blood pressure from the desired value.

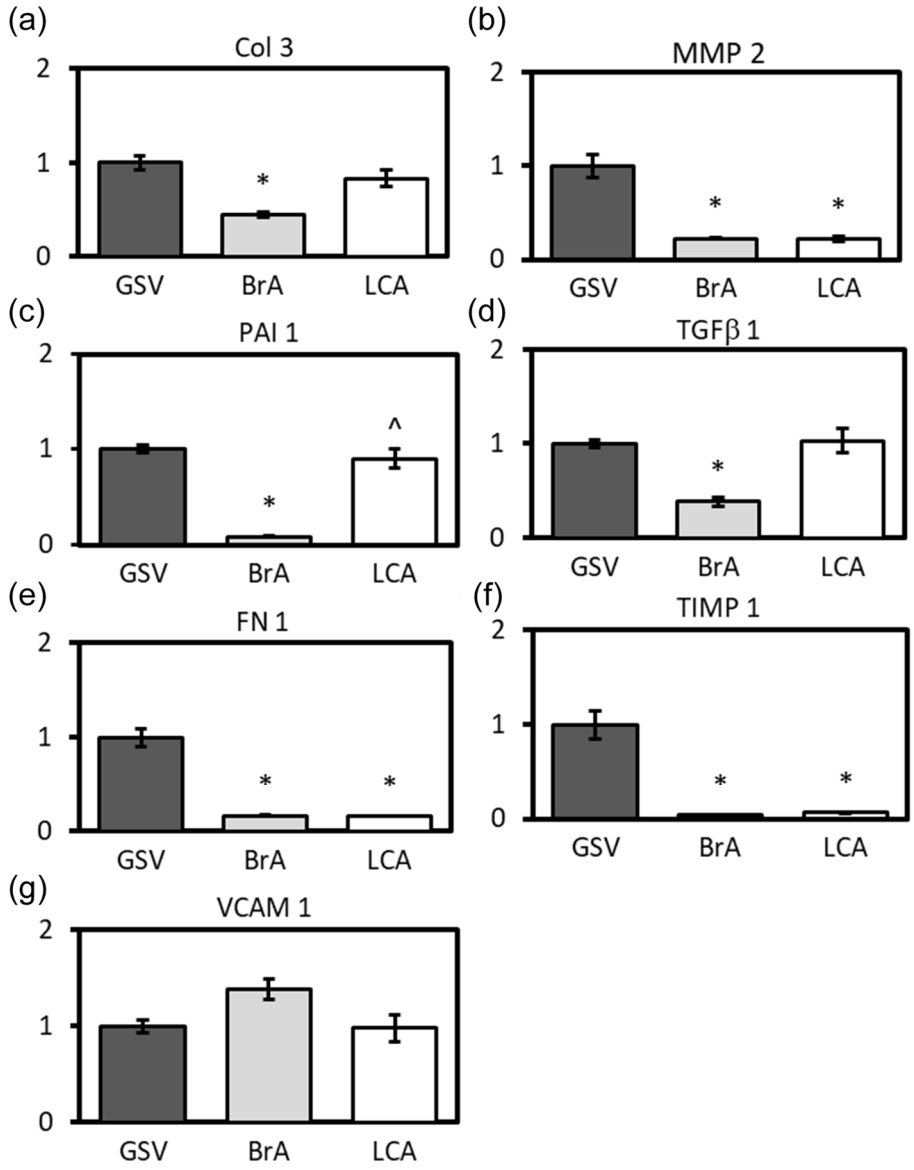

Figure 4.9 – Gene expression profiles for GSVs exposed to GSV, BrA, or LCA-like pulsatile media pressure and flow waveforms for 6 h. Data are reported as fold change relative to the GSV conditions. Error bars indicate ± standard error of the mean. (*) denotes differences between GSVs exposed to LCA or BrA conditions and the GSV at IS conditions. (^) Denotes differences between GSVs exposed to BrA and GSVs exposed to LCA. Statistical significance is considered at $p<0.05$.

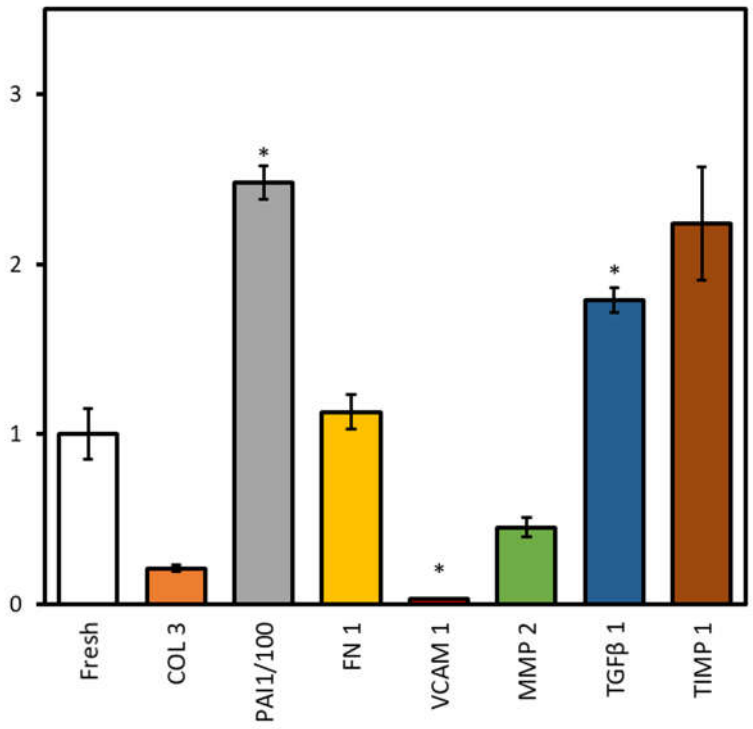

Figure 4.10 – Relative expression profiles of select vascular remodeling genes for the GSV after 6 h of in vitro culture at in situ pressure, flow and axial loading conditions represented as fold change from freshly harvested vessels. (*) Denotes significant differences between the measured gene after 6 h of culture and freshly harvested

CHAPTER 5

COMPARATIVE BIAXIAL MECHANICS OF MAMMALIAN CAROTID ARTERIES[4]

[4] Prim, D. A., Mohamed, M. A., Lane, B. A., Poblete, K., Wierzbicki, M. A., Lessner, S. M., Shazly, T., Eberth, J. F.. Submitted to *PLoS ONE*, 12/22/2017

5.1 ABSTRACT

The prevalence of diverse animal models as surrogates for human vascular pathologies necessitate a comprehensive understanding of the differences that exist between species. Comparative passive mechanics are presented here for the common carotid arteries taken from bovine, porcine, ovine, leporine, murine-rat, and murine-mouse specimens. Data is generated using a scalable biaxial mechanical testing device following consistent protocols and fit to two common constitutive models of arterial behavior: the phenomenological Fung-type exponential and the structurally-motivated 4-fiber Holzapfel-Gasser-Ogden (HGO) model. Both models fit experimental data well across all examined species. The structural mechanical response of carotids under equivalent loading, quantified by the deformed inner radius, deformed wall thickness, lumen area compliance and axial force, varies significantly among species but generally follows allometric scaling. Conversely, descriptors of the local mechanical response within the deformed arterial wall, including mean circumferential stress, mid-wall circumferential stretch, and mean axial stress, are relatively consistent across species. Taken together, our results provide baseline structural and mechanical information for carotid arteries across a broad range of common animal models.

5.2 INTRODUCTION

In humans and all other mammals, common carotid arteries (CCAs) supply oxygenated blood to critical cognitive and masticatory structures. Atherosclerosis of the CCAs, otherwise known as carotid artery disease, begins as an asymptomatic pathology and can lead to stenosis, plaque embolism, and ischemic stroke [210]. Of approximately 800,000 strokes in the U.S. each year as many as 15% can be attributed to carotid artery

disease [211,212]. According to a recent clinical investigation, over 30% of asymptomatic patients age 40-54 exhibit subclinical CCA atherosclerosis [213], suggesting a very large aging population at future risk of stroke and motivating further study into disease progression, diagnosis, and treatment.

Mechanical changes in carotid arteries can occur as a result of surgical intervention, device implantation, local and systemic disease progression, and tissue remodeling in response to altered hemodynamic stimuli. For example, carotid arteries from patients with dyslipidemia and type II diabetes were shown to be stiffer than paired noninjured arteries [214], which is commonly acknowledged as a predictor of increased risk of mortality [215]. Carotid artery stenting and carotid endarterectomy on the other hand, are the two most common interventions for severe carotid artery disease [216]. In either case understanding the baseline CCA mechanics can be fundamental to characterizing both healthy remodeling and undesirable pathologies [217,218].

Quantification of passive arterial mechanical properties requires freshly excised tissue tested in a biaxial configuration, with diverse mammalian tissue used in many preliminary investigations to test hypotheses that would be impractical, if not impossible, to test on human tissue [15,28,46,139,218–221]. For the case of studies involving CCA mechanics, it may be prudent to select an animal model with specific baseline values of structural or mechanical properties under physiological loading that may scale with mammalian weight. It is likely that some, but not all, CCA properties follow allometric scaling laws among mammals, but such relationships have not yet been established [222–225].

In this study, we investigate and compare the passive biaxial mechanical properties of CCAs freshly harvested from bovine, porcine, ovine, leporine, and two murine animals, the laboratory rat and the laboratory mouse. A unique yet modular biaxial testing device is used to measure the passive mechanical properties through inflation-extension testing using similar protocols and procedures for each vessel. All experimental data is then fit to two widely accepted constitutive models: the phenomenological Fung-exponential, and the structurally motivated 4-fiber family Holzapfel-Gasser-Ogden (HGO) model [4,5]. Once identified, model parameters can be implemented into diverse boundary value problems and computational models. Obtained results therefor provide a catalog of information that can be used to guide the selection of animal models for future CCA studies.

5.3 MATERIALS AND METHODS

5.3.1 Vessel Isolation and Preparation

Male bovine (Angus cow; 500 kg), porcine (American Yorkshire pig; 108 kg), ovine (Suffolk-Rambouillet sheep; 35.1 kg), and leporine (New Zealand White rabbit; 4.03 kg) carotid specimens (n=6; each) were obtained from local abattoirs at roughly 18, 6, 10, and 3 months old respectively. Specimens from bovine, porcine, and ovine animals were designated for consumption and considered to be mature at the time of slaughter. Murine-rat (Sprague-Dawley rat; 0.49 kg) and murine-mouse (C57BL/6J mouse; 0.028 kg) were laboratory animals sacrificed at 8 and 3 months of age respectively and were subject to Animal Care and Use Committee (IACUC) approval at the University of Houston and the University of South Carolina.

Vessels were harvested immediately after slaughter/sacrifice and transported in sterile Moscona's saline solution at 4° C to the laboratory where perivascular and loose

adventitial tissue was removed from each sample. The perivascular tissue was notably more difficult to remove from the larger vessels. To minimize edge effects, vessels were trimmed so that the length was at least 10-times greater than the diameter but fit within the 25cm long tissue bath of the biaxial testing device at 2-times its unloaded length. Vessels were then secured to appropriately-sized barbed fittings, syringe needles, or glass cannulas (mouse only) with braided silk suture. Prior to and throughout testing, Krebs-Henseleit solution at pH 7.4 and containing 10^{-5} M sodium nitroprusside was perfused through, and around, the sample and then continuously circulated in the adventitial bath in order to guarantee a fully relaxed smooth muscle state. Once mounted within the test chamber samples were maintained at 37.2 ^{o}C using a 15W submersion heater within the adventitial bath.

5.3.2 Biaxial Mechanical Testing

All mechanical testing was performed on a modular, custom-designed, biaxial mechanical testing device with LabView-based data acquisition (National Instruments; Austin TX). Reference [226] provides much of the general layout of a similar testing apparatus with hardware in that publication specific to the mouse carotid arteries and ours designed to accommodate larger specimens. Other differences in hardware or configuration are described here. Luminal inflation was initiated with a feedback controlled syringe pump (World Precision Instruments; Sarasota, FL) and pressure measured using an amplified 0-300 mmHg USB pressure transducer (Omega Engineering, Norwalk, CT). To accommodate large variations in vessel size, the objective lenses for a CMOS Monochrome 1280x1024 USB camera (Edmund Optics; Barrington, NJ) were selected to yield 580 pixels/mm, 287 pixels/mm, 144 pixels/mm, or 52.0 pixels/mm. Likewise force transducers

(Omega Engineering) capable of measuring up to 0.1 N, 1.1 N, or 44 N were interchanged once a preliminary force range was determined for each species. The force transducer was connected to the blood vessel using a pivoting L-shaped arm allowing the transducer to be isolated from the liquid media. Stepper motor micrometer-driven translation stages (Thorlabs; Newton, NJ) were also chosen with 10 mm, 25 mm, or 100 mm of travel to provide adequate axial extensions. Each piece of hardware was extensively calibrated prior to data collection.

Initial measurements were made of the unloaded length and diameter with the specimen mounted in the biaxial testing device, but prior to pressurization or axial extension. To ensure repeatable loading curves, all vessels underwent three cycles of preconditioning of inflation/deflation pressurization from 0-160 mmHg (1 mmHg/s) at 1.50±10% axial extension ratio. Following preconditioning, vessels were axially extended to 1.5 and pressurized step-wise from 0-160 mmHg in 10 mmHg increments. A 10 second equilibrium period was allowed at each step then diameter measurements were collected via the calibrated CMOS camera (Figure 5.1, left) and axial force measurements recorded. Next, luminal pressure was adjusted to 100 mmHg, and the axial stretch λ_z set so that vessels experienced a very small tensile force. This stretch was recorded as $\lambda_z^{\min}$. Then vessels were extended axially in stretch increments corresponding to a 0.05 increase in extension ratio while recording outer diameter and axial force at each step following a 10 second equilibrium period.

5.3.3 Data Analysis

Vessels were removed from the device and centrally located ring sections cut from the samples. Images of rings were collected using a microscope mounted DSLR camera

(Canon USA, Long Island NY) and the magnification set to maximize the field of view using the millimeter scale of a ruler (Figure 5.1, right). The unloaded inner and outer circumference of each section were quantified using ImageJ software (NIH), and the inner R_i and outer R_o radii calculated. From this, the cross-sectional tissue area was calculated via

$$A = \pi\left(R_o^2 - R_i^2\right) \qquad [5.1]$$

Unlike prior work (see [15,227]), we chose not to induce a stress relieving cut. Although straightforward with large vessels, prior experience with mouse carotid arteries suggested that the stress relieving cut would introduce considerable error (laboratory observations).

Through real time measurements of outer diameter and assuming vessel incompressibility, the deformed inner radius r_i is calculated from

$$r_i = \sqrt{r_o^2 - \frac{A}{\pi\lambda_z}}\,, \qquad [5.2]$$

where $r_o = OD/2$ is the deformed outer radius and λ_z the axial stretch ratio. The lumen area compliance is then calculated from

$$C_A = \pi\frac{\Delta r_i^2}{\Delta P}, \qquad [5.3]$$

where P is the transmural pressure. For consistency, ΔP is measured around 100 mmHg and Δr_i the change in radius about this point. Mean circumferential and axial stresses are calculated as

$$\sigma_\theta = \frac{Pr_i}{h} \quad , \quad \sigma_z = \frac{F + P\pi r_i^2}{\pi\left(r_o^2 - r_i^2\right)}, \qquad [5.4]$$

with F, the axial force, and $h = r_o - r_i$ the wall thickness. The pressure contribution on the right-hand-side of equation [5.4] is consistent with a force balance of a pressurized, closed tube [137].

The circumferential, axial, and radial stretches are calculated by

$$\lambda_\theta = \frac{r_i + r_o}{R_i + R_o}, \quad \lambda_z = \frac{l}{L} \quad , \quad \lambda_r = \frac{1}{\lambda_\theta \lambda_z} \quad , \qquad [5.5]$$

where we note the radial stretch is found via incompressibility and circumferential stretch represents the mid-wall value.

5.3.4 Theoretical Framework

All vessels are modeled within a continuum mechanics framework. Here the radial, circumferential, and axial Cauchy stresses can be found via

$$\sigma_\theta = -p + \lambda_\theta^2 \frac{\partial W}{\partial E_{\theta\theta}} \quad , \quad \sigma_z = -p + \lambda_z^2 \frac{\partial W}{\partial E_{zz}} \quad , \quad \sigma_r = -p + \lambda_r^2 \frac{\partial W}{\partial E_{rr}} \quad , \qquad [5.6]$$

where p is the Lagrange multiplier used to enforce incompressibility and E_{rr}, $E_{\theta\theta}$, and E_{zz}, are components of the Green strain tensor and relate to the stretch ratios by:

$$E_{\theta\theta} = \frac{1}{2}\left(\lambda_\theta^2 - 1\right) \quad , \quad E_{zz} = \frac{1}{2}\left(\lambda_z^2 - 1\right) \quad , \quad E_{rr} = \frac{1}{2}\left(\lambda_r^2 - 1\right), \qquad [5.7]$$

assuming $\sigma_\theta \ \ \sigma_r \ \ \sigma_z$, then $\sigma_r \approx 0$, and from the right hand side of [5.6],

$$p = \lambda_r^2 \left(\partial W / \partial E_{rr}\right) \qquad [5.8]$$

Thus, a two-dimensional approximation of [5.6] is found such that

$$\sigma_\theta = \lambda_\theta^2 \frac{\partial W}{\partial E_{\theta\theta}} - \lambda_r^2 \frac{\partial W}{\partial E_{rr}} \quad , \quad \sigma_z = \lambda_z^2 \frac{\partial W}{\partial E_{zz}} - \lambda_r^2 \frac{\partial W}{\partial E_{rr}} . \qquad [5.9]$$

For this investigation we consider two popular forms of W. First, we utilize a formulation of the phenomenological Fung-type exponential model described by Chuong and Fung [4]. In the absence of shear terms, the equation for strain energy is

$$W = c_0\left(e^Q - 1\right), Q = c_1E_{rr}^2 + c_2E_{\theta\theta}^2 + c_3E_{zz}^2 + 2c_4E_{rr}E_{\theta\theta} + 2c_5E_{\theta\theta}E_{zz} + 2c_6E_{rr}E_{zz}, \quad [5.10]$$

where c_0 is a stress-like material parameter and c_i, $i = 1-6$ are non-dimensional parameters. To ensure convexity $c_i > 0$ and $c_1c_2 > c_4^2$, $c_2c_3 > c_5^2$, and $c_1c_3 > c_6^2$ [5,228].

Next, we utilize a structurally motivated model initially proposed by Holzapfel, Gasser, and Ogden (HGO), and later modified to include additional fiber families [5,6]. This particular model separates the isotropic from the anisotropic contribution to the strain energy

$$W = \frac{c}{2}\left(\lambda_\theta^2 + \lambda_z^2 + \frac{1}{\lambda_\theta^2\lambda_z^2} - 3\right) + \sum_{k=1,2,3,4}\frac{c_{1,k}}{4c_{2,k}}\left\{\exp\left[c_{2,k}\left(\lambda_k^2 - 1\right)^2\right] - 1\right\} \quad [5.11]$$

Here a total of four fiber families $k = 1, 2, 3, 4$ are considered with $\lambda_k = \sqrt{\lambda_\theta^2\sin^2\alpha_k + \lambda_z^2\cos^2\alpha_k}$ the stretch of the k^{th} fiber family, and α_k is the angle that family makes with respect to the longitudinal axis. c is a material parameter for the isotropic contribution, and $c_{1,k}$ and $c_{2,k}$ material parameters for the anisotropic contributions. We assume that α_1 =90 deg represents circumferentially oriented fibers and α_2 =0 deg represents those that are oriented axially. We further consider two of the families to be symmetric and helically arranged so that $\alpha_3 = -\alpha_4$, $c_{13} = c_{14}$, and $c_{2,3} = c_{2,4}$ [5,15,139].

Equations [5.4] and [5.9] yield expression for the modeled pressure and force, namely

$$P = \frac{h}{r_i}\left[\lambda_\theta^2 \frac{\partial W}{\partial E_\theta} - \lambda_r^2 \frac{\partial W}{\partial E_r}\right],\ F = \pi h\left(2r_i + h\right)\left[\lambda_z^2 \frac{\partial W}{\partial E_z} - \lambda_r^2 \frac{\partial W}{\partial E_r}\right] - P\pi r_i^2\ , \qquad [5.12]$$

from which the only unknown values are the material parameters in each strain energy function. These best-fit values are found by minimizing an objective function between the experimentally (exp) measured and modeled (mod) pressure and force. An objective function is then postulated of the form

$$e = \sum_{n=1}^{N}\left[\left(\frac{P^{mod} - P^{exp}}{\bar{P}^{exp}}\right)_i^2 + \left(\frac{F^{mod} - F^{exp}}{\bar{F}^{exp}}\right)_i^2\right] \qquad [5.13]$$

which was found to best fit to biaxial data at both high and low loads [142,145]. Here the over-bar denotes the mean value. A multivariate regression analysis is performed on this objective function using MATLAB (MathWorks; Natick, MA).

5.3.5 Statistical Analysis

Figures demonstrating continuous data (Figures 5.2 and 5.5) are expressed as the mean ± the standard error of the mean while discrete data (Figures 5.3 and 5.4) are presented as the mean ± the standard deviation. Paired comparisons were performed using two-tailed student t-tests with a value of $p < 0.05$ considered to be significant.

5.4 RESULTS

Data is displayed for bovine, porcine, ovine, leporine, murine-rat, and murine-mouse groups in the order of decreasing body weight with values representing the mean of n=6 samples. Most measured structural quantities are shown to increase with animal weight. Notably, ovine carotids present axial force, outer diameter, and wall thickness values that break the pattern of scaling, as ovine specimens have lower body mass than porcine specimens. Leporine lumen area compliance was also found to be less than that of

the murine-mouse. The pressure-outer diameter graph shows similar patterns within physiological ranges across the six species tested (Figure 5.2, top). Notable differences include the murine carotid samples that have a concave pattern at pressures below 80mmHg but transitions to a convex relationship at higher pressures, while porcine, ovine, leporine, and bovine samples display a convex relationship at all tested pressures.

When compared at 100 mmHg and 1.5 axial stretch ratios (Figure 5.3) the inner radius and wall thickness, of bovine (r_i=3.35±0.30 mm, p<0.001; h=1.06±0.14 mm, p<0.001), porcine (r_i =2.24±0.31 mm, p<0.001; h =0.37±0.10 mm, p<0.001), and ovine (r_i=2.15±0.42 mm, p<0.004; h =0.48±0.17 mm, p<0.016) arteries were significantly different than those of leporine (r_i=1.08±0.16 mm; h=0.22±0.07 mm), murine-rat (r_i =0.484±0.070 mm; h=0.087±0.031 mm), or murine-mouse (r_i=0.290±0.070 mm; h =0.035±0.001 mm). Despite a high standard deviation in lumen area compliance, differences were still significant for bovine (C_A=1.5x10^{-3} ± 8.1x10^{-4} mm^2/mmHg, p<0.004) compared to leporine (C_A=6.1x10^{-5} ± 3.9x10^{-5} mm^2/mmHg; p=0.022), murine-rat (C_A=3.2x10^{-4} ± 1.3x10^{-4} mm^2/mmHg, p=0.040), or murine-mouse (C_A=2.6x10^{-5} ± 1.9x10^{-5} mm^2/mmHg, p=0.021). Significant area compliance differences were also found between porcine (C_A=6.8x10^{-4} ± 5.6x10^{-4} mm^2/mmHg) and murine-mouse (p=0.047), and between the leporine and murine-rat (C_A=3.2x10^{-4} ± 1.3x10^{-4} mm^2/mmHg, p=0.004). Average values of axial force and axial stretch also display similar, but highly nonlinear relationships across species that are more evident on a non-logarithmic scale. The axial force for the bovine specimens (F =4,890 ± 3,132 mN, p<0.019) was different than porcine (F =213.1 ± 179.8 mN), ovine (F =576.3 ± 276.7 mN), leporine (F =6.430 ± 3.73 mN),

murine-rat (F =3.610 ± 2.62 mN) or murine-mouse (F =0.804 ± 0.414 mN). The porcine and ovine specimens were also different from the leporine and murine specimens ($p<0.049$).

While vessel geometry varies widely between species, the stress and stretch metrics facilitate comparisons that are independent of length scale (Figure 5.4 and Figure 5.5). Circumferential stress was found to be lower in the bovine (σ_θ=42.9±6.88 kPa) than porcine (σ_θ=86.8±31.4 kPa, p=0.025), leporine (σ_θ=74.0±25.7, p=0.041), and murine-mouse (σ_θ=111±34.1 kPa, p=0.015) counterparts while ovine specimens σ_θ=57.6±13.5 kPa, p=0.032) had significantly lower circumferential stress only in comparison to murine-mouse (p=0.032). Likewise, bovine axial stress (σ_z =184 ± 42.2 kPa) was higher than in porcine (σ_z =74.1 ± 27.4 kPa, p=0.049), leporine (σ_z =32.4 ± 9.56 kPa, p=0.031), and murine-rat (σ_z =54.3 ± 34.3 kPa, p=0.029) arteries, while the porcine (p=0.009) and murine-mouse (p=0.005) groups were lower than the leporine group. The porcine circumferential and minimum axial stretches (λ_θ =1.49 ± 0.16; $\lambda_{z,\min}$ =1.29 ± 0.06) were found to be lower than leporine (λ_θ =1.93 ± 0.25, p=0.044; $\lambda_{z,\min}$ =1.43 ± 0.02, p=0.039) and murine-mouse (λ_θ =1.81 ± 0.22, p=0.030; $\lambda_{z,\min}$ =1.37 ± 0.02, p=0.039) while the minimum ovine axial stretch ratios ($\lambda_{z,\min}$ =1.40 ± 0.03, p=0.009) were also lower than in the porcine specimens. The minimum axial stretch ratio was also found to be lower in the bovine ($\lambda_{z,\min}$ =1.30 ± 0.10, p=0.030) and the murine-mouse ($\lambda_{z,\min}$ =1.37 ± 0.02, p=0.032) compared to the leporine.

Biaxial mechanical data from all six species fit well to each of the two constitutive models (Tables 5.1 and 5.2). The 4-fiber family HGO model had a lower average error

across all species (RMSE=0.16±0.08) than the phenomenological Fung-type model (RMSE=0.23±0.09). A plot of the strain energy for both models can be seen in Figure 5.6 for λ_θ = [1.00,1.85], λ_z = [1.00,1.85]. For each species, both models with the reported parameters are convex but demonstrate slightly different responses in terms of strain energy.

5.5 DISCUSSION

The current work reports on the biaxial mechanical properties of common carotid arteries from 6 distinct but common mammalian species. Due to the long, unbranched, and paired anatomy, CCAs, especially canine models, are well studied in the literature. Although collectively many datasets are available from a wide-variety of sources, challenges in scalability have previously been a limitation on such a wide range of being reported in a single published work. An exception to this is the experimentation performed by RH Cox (1978) who studied the mechanics of the canine, leporine, and murine-rat carotid arteries [225]. That investigation demonstrated similar outer diameter and circumferential stress to ours but no axial forces were reported. Cox, as in our study, reported a concave pattern in the pressure-diameter curves at low levels of pressure in the smaller animals but not in the larger ones. Similar patterns and diameter ranges were also reported in the work of Weizsäcker et al. (1983) who investigated biaxial properties of murine-rat carotid arteries [229]. Chuong and Fung (1983), and later Takamizawa (2015), experimented on leporine arteries and fit their results to constitutive models [4,230]. Although deformed inner radii in that study is similar to our current work and that of Weizsäcker et al., our reported axial forces are lower in the leporine and murine-rat models. This could be attributed to variations in an animal's genetic background or age [47,231].

Despite the abundance of canine data, and to a lesser extent porcine, (e.g., [225,227]), there are surprisingly few biaxial tests of bovine carotid mechanics. Von Maltzahn (1984) conveniently performed biaxial testing on carotids samples at the same pressures and axial extensions used in our study. Although the diameters were slightly larger than those reported here, axial forces were lower [232]. These differences may be due to the breed and/or the age of animal, but that specific information was not reported in their work. To our knowledge, Blondel and colleagues (2001) present the only published biaxial mechanics data to date on sheep (ovine) carotid arteries [233]. Their animals and corresponding structural parameters appear to be slightly larger than those presented here, and again, the axial force and stress data were not reported. Nevertheless, other comparable mechanical parameters appear to be consistent with the ovine results reported herein. The lack of information for bovine and ovine models is surprising considering the growing importance of these animals to the field of decellularized vascular grafts and implant models [234,235]. Of further note, all vessels appear to be less stiff than the limited existing data on human biaxial CCA mechanics [236,237].

An abundance of biaxial data from control, surgically altered, and genetically modified murine-mouse models have been reported in our prior work [29,47,137,142,221]. Of note, the carotid arteries studied in the current investigation are comparable in mechanical properties to many of the controls of those prior studies. One notable exception is that the axial stretch ratio is lower here and actually represents a sub-physiological level for the murine-mouse. In fact, it is likely that the leporine and both murine models are compared at sub-physiological levels of axial extension while the bovine models are at supra-physiological levels. Since axial extension affects virtually all our quantified metrics

(see for example, equations [5.2], [5.5] , and [5.12]), this condition would help to explain the high measured force (and axial stress) in bovine specimens. To eliminate additional confounding variables however, we chose to compare these species at a common axial stretch ratio while recording the minimum axial stretch required to achieve tension while pressurized. An axial stretch of 1.5 appeared to be the most common reference point from the literature for diverse mammalian species [227,229,230,238].

Allometric scaling is applied to the results (Figure 5.7, see [239]) using a power law equation [240] of the form

$$y = k \cdot w^a \qquad [5.14]$$

that relates the dependent variable y to the independent variable w (in this case animal weight) using a coefficient k and scaling exponent a. When plotted against body weight, the inner radius (R^2=0.982), wall thickness (R^2=0968), area compliance (R^2=0.742), and axial force (R^2=0.900) were all well represented by [5.14]. In contrast, no obvious scaling existed for the circumferential and axial stresses and stretches. These values however, were closely grouped amongst many of the animals tested. Likewise, Wolinsky and Glagov compared aortas from diverse mammalian species to demonstrate that lamellar units – a major contributor of mechanical properties in arteries – remain relatively consistent across species. These authors observed ranges in deformed outer diameter from 1.2 to 23.0 mm and body weight from 0.028 to 200 kg; despite this, aortas across all species exhibit medial lamellar units of similar size (0.006 to 0.018 mm) that experience similar tension per lamellar unit (1,090 to 3,010 dynes/cm) [239]. Moreover, the endothelial, smooth muscle, and fibroblasts cells which serve as both sensor and effector in the assembly of wall constituents, remains the same size even in a vessel wall that can be 15-fold larger. We

also consider that proteins (e.g., collagen and elastin) can vary in fractional mass but their structure is preserved across species. While this investigation focuses primarily on biomechanical analysis, future work would benefit from more thorough comparison of CCA microstructure across species to complement the mechanical comparison herein. Still, a priori knowledge of scalable (e.g., geometric) versus non-scalable (e.g., stress/stretch) metrics are important in guiding the selection of animal models and their anticipated biological response.

Both of the chosen constitutive models effectively captured the biaxial data from all six species. While the Fung-type exponential model exhibited a reasonable fit for these data, only one of the fitted variables is a stress-like parameter. Moreover, the constraints placed on the formulation to ensure a convex solution are considerable [5,241]. Despite this, a historical precedent exists for using this model, including the reference citation – Chuong and Fung – that describes experiments using the leporine animal model, one of our six mammalian species; therefore, it is a logical benchmark for comparison [4]. Nevertheless, the 4-fiber HGO model exhibited a better fit and has added utility in being a structurally motivated model where parameters have a more direct physical interpretation. However, the inherent value of both models lies in their ease of translation into other studies.

Comparing the biaxial mechanical properties of CCAs across mammalian species supports two discrete research directions. First, animal studies are a critical tool in elucidating disease progression, evaluating novel treatment options, and developing implantable devices for a wide range of diseases, including carotid artery disease. As discussed previously, the mechanical properties of the vasculature are subject to change as

a result of both disease and treatment, and quantifying these changes requires a thorough characterization of baseline mechanical properties. Therefore, this investigation provides preliminary mechanical data that can be used to guide the selection of animal models for carotid artery research and to provide comparative data from healthy vessels to compare with treatments and disease states.

Next, as demand continues to increase for vascular grafts as treatment options for severe cardiovascular disease, significant research has begun to explore options beyond traditional autologous grafts. Artificially engineered vascular grafts have proven difficult to adequately match necessary material properties while maintaining long-term patency [242], so recent efforts have explored the use of decellularized blood vessels as a scaffold for vascular graft procedures [243–247]. Since decellularization nominally ameliorates immunogenicity by removing all cellular material, leaving only the ECM components responsible for passive mechanical properties, graft options need not be limited to human vessels. The most pressing need for improved graft options lies in small-diameter artery grafts, so decellularized conduit arteries of smaller mammals represent a potential avenue of research for graft options in humans. In theory, given basic information about a graft destination – e.g., pressure, deformed inner radius, and compliance – a clinician could reference a catalog of mechanically characterized non-human vessels, such as the investigation herein, to identify the most mechanically compatible scaffold for that particular situation.

While we support the scientific merit of this investigation, we must also acknowledge certain limitations. First, we chose not to quantify residual strains via opening angles of fresh cross-sectional slices. Residual strains are known to normalize the

transmural stress distribution in a given vessel but can be difficult to measure reliably at smaller length scales. Further, due to the range of tissues used herein, animal ages could not be standardized to a single relative maturity in each species; however, within a given species, all tested samples came from adult specimens of approximately equal age and size. Furthermore, due to large variations in measured variables across species (e.g., axial force, vessel diameter), several hardware configurations were required to maintain fidelity of the collected data. Nevertheless, testing was consistent within a given species, all hardware was calibrated prior to testing, and protocols were consistent regardless of species or hardware.

5.6 ACKNOWLEDGEMENTS

The authors would like to acknowledge the contributions of undergraduate researcher Hannah Gore.

5.7 TABLES

Table 5.1 – Fitted parameters for six mammalian species using the Fung-type [4] material model.

		c_0(kPa)	c_1	c_2	c_3	c_4	c_5	c_6	Error RMSE
Bovine	avg	10.7	2.79	1.10	1.95	0.89	0.37	0.08	0.28
	std	22.7	2.04	0.15	0.62	0.28	0.34	0.16	0.04
Porcine	avg	25.7	1.68	1.43	1.00	0.78	0.52	0.87	0.23
	std	19.5	0.80	0.85	0.01	0.37	0.44	0.21	0.13
Ovine	avg	20.9	1.87	1.09	1.63	0.61	0.19	0.15	0.17
	std	28.5	0.83	0.17	0.46	0.53	0.23	0.33	0.03
Leporine	avg	5.98	1.00	1.01	1.00	2.E-05	0.17	0.99	0.30
	std	2.16	6.E-03	5.E-03	4.E-04	0.48	0.21	0.44	0.10
Murine-rat	avg	2.30	12.27	1.00	1.00	0.85	0.35	0.83	0.32
	std	3.61	15.39	3.E-04	2.E-04	0.21	0.48	0.31	0.14
Murine-mouse	avg	2.98	11.0	1.10	1.08	0.88	0.48	0.48	0.34
	std	5.09	18.9	0.26	0.15	0.33	0.38	0.50	0.17
								avg	0.23
								std	0.09

Table 5.2 – Fitted parameters for six mammalian species using the 4-fiber family HGO material model [5,6].

		c (kPa)	$c_{1,1}$ (kPa)	$c_{1,2}$	$c_{2,1}$ (kPa)	$c_{2,2}$	$c_{3,1} = c_{4,1}$(kPa)	$c_{3,2} = c_{4,2}$	$\alpha_3 = -\alpha_4$ (deg)	Error RMSE
Bovine	avg	3.44	5.81	0.52	1.03	0.86	7.59	0.86	27.6	0.23
	std	6.65	12.9	0.78	2.24	1.00	17.0	0.57	18.1	0.08
Porcine	avg	14.6	0.76	3.83	0.77	0.37	2.40	3.19	52.6	0.20
	std	13.0	0.75	3.76	0.71	0.29	3.46	4.83	20.5	0.11
Ovine	avg	9.92	0.26	3.91	1.29	0.98	0.80	2.11	47.4	0.22
	std	7.56	0.46	6.28	1.30	0.77	0.75	1.46	8.4	0.06
Leporine	avg	6.77	0.11	0.57	0.52	0.34	2.13	0.26	39.1	0.09
	std	6.04	0.12	0.38	0.65	0.58	1.49	0.53	30.0	0.05
Murine-rat	avg	9.48	2.58	1.14	0.63	0.68	5.87	0.32	42.4	0.18
	std	8.97	4.25	1.16	1.03	0.78	8.95	0.30	31.8	0.15
Murine-mouse	avg	8.49	1.16	0.62	1.11	0.44	2.56	1.16	46.0	0.19
	std	6.33	2.19	0.62	1.01	0.14	3.79	1.12	13.4	0.12
									avg	0.16
									std	0.08

5.8 FIGURES

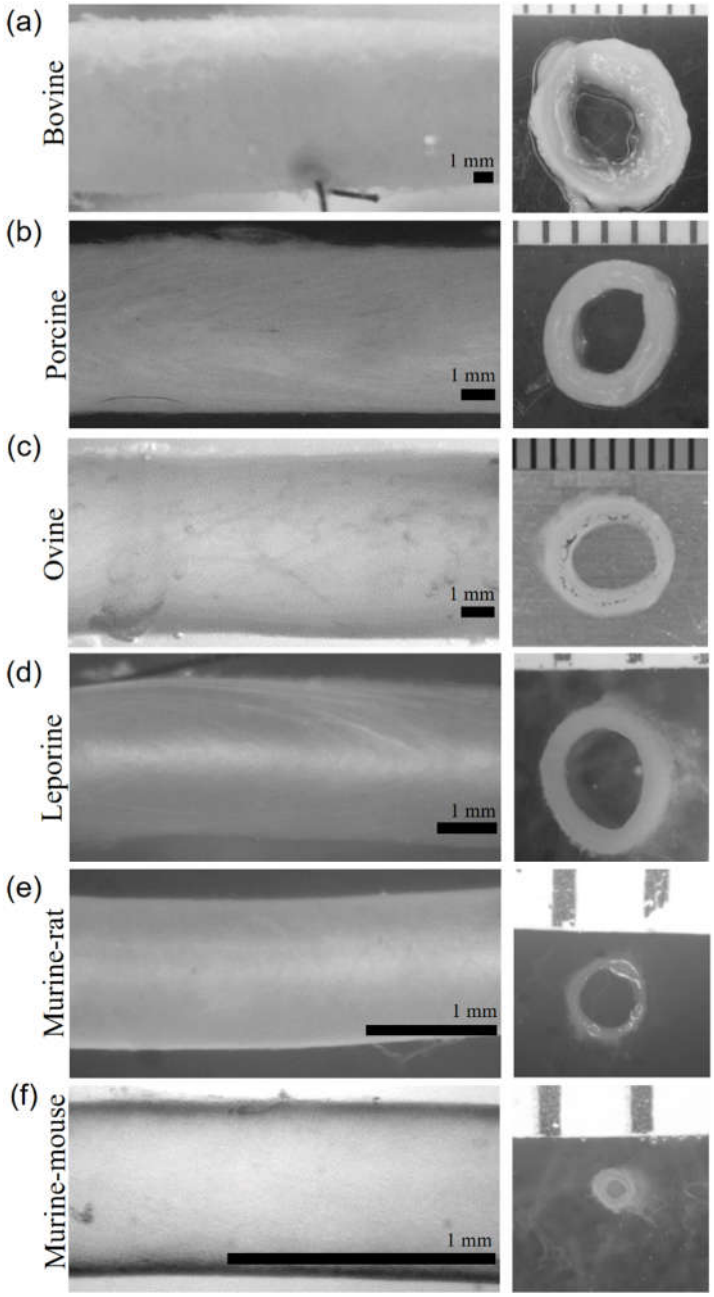

Figure 5.1 – Images of common carotid arteries. (left) Vessels mounted within the biaxial testing device at λ_z=1.5 and P=100 mmHg. (a) Bovine: OD = 8.82 mm, (b) porcine: OD = 4.96 mm, (c) ovine: OD = 5.49 mm, (d) leporine: OD = 2.60 mm, (e) murine-rat: OD = 1.14, and (f) murine-mouse: OD = 0.65 mm vessels shown. Scale bars are 1 mm. (right) Unloaded ring sectors of each vessel with 1 mm ruler.

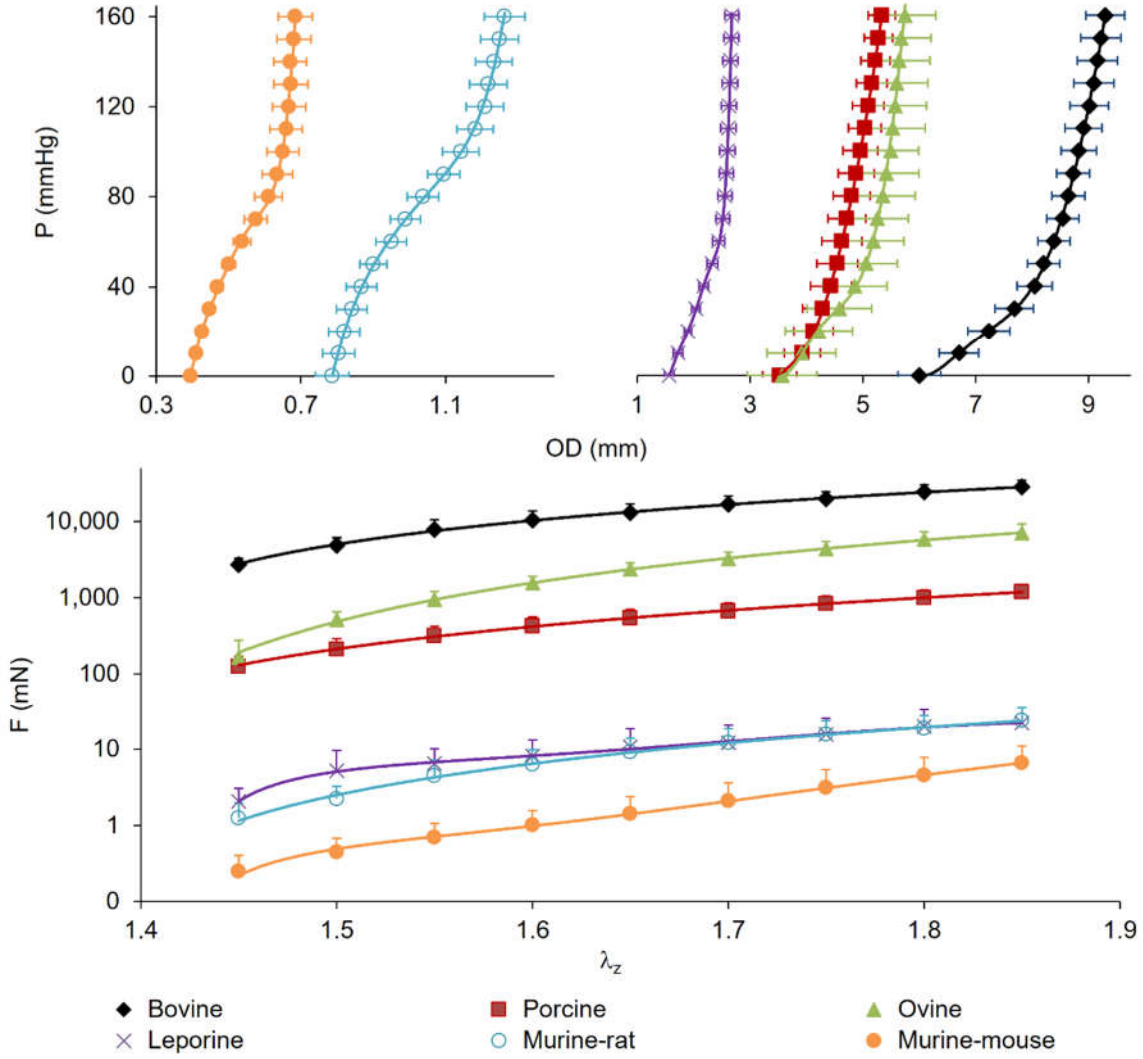

Figure 5.2 – Full range of common carotid arteries subjected to passive biaxial mechanical testing. (top) Pressure-diameter at λ_z=1.5, (bottom) axial force-stretch on a logarithmic scale at P=100 mmHg for Bovine, porcine, ovine, leporine, murine-rat, and murine-mouse. All values are mean (n=6) ± SEM.

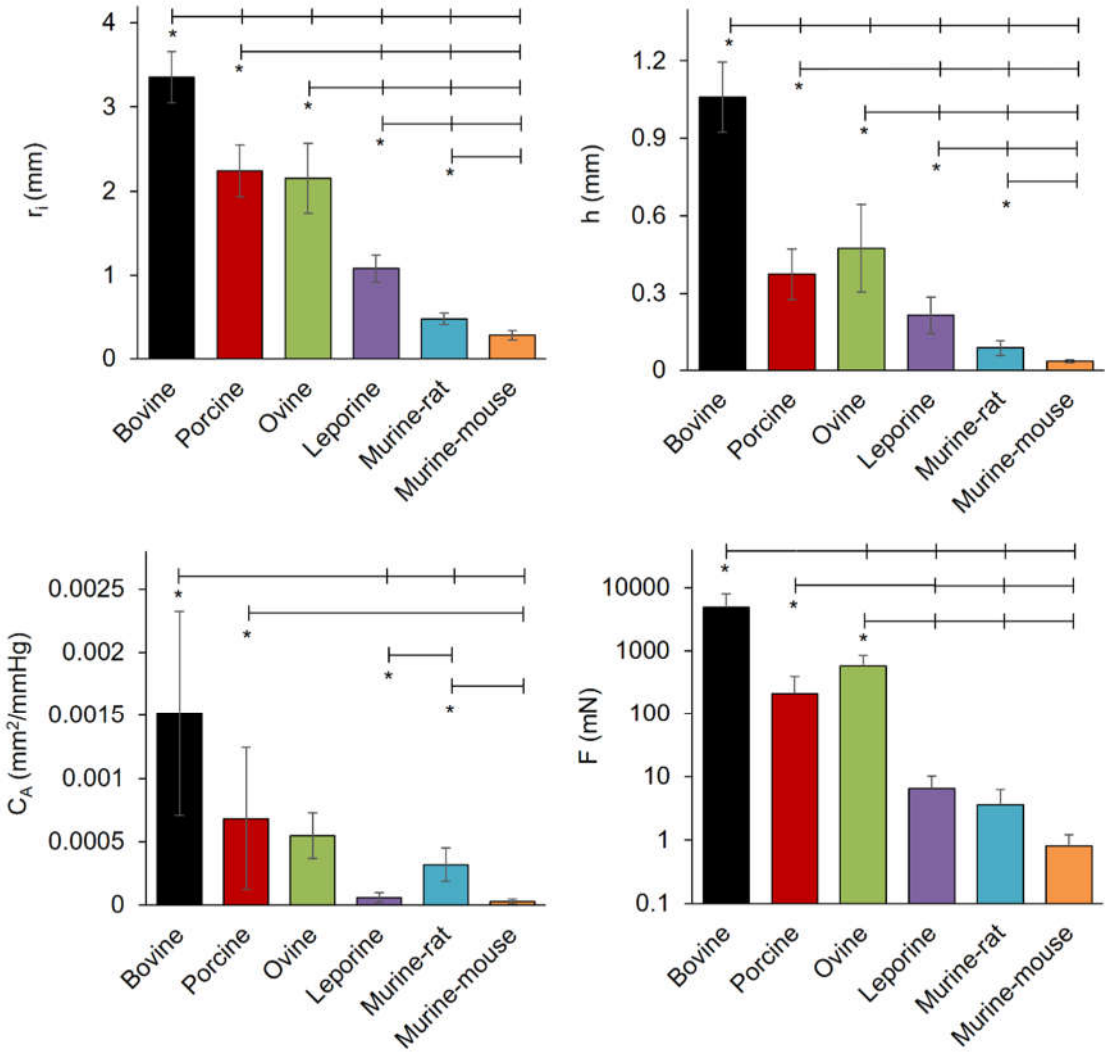

Figure 5.3 – Comparative structural and force values for common carotid arteries subjected to passive biaxial mechanical testing at 100 mmHg and 1.5 axial stretch ratio. (a) Inner radius, (b) wall thickness, (c) area compliance, and (d) axial force from bovine, porcine, ovine, leporine, murine-rat, and murine-mouse carotid arteries. All values are mean ± standard deviation. (*) denotes statistical significance at $p<0.05$ between the leftmost group and the corresponding hash-mark.

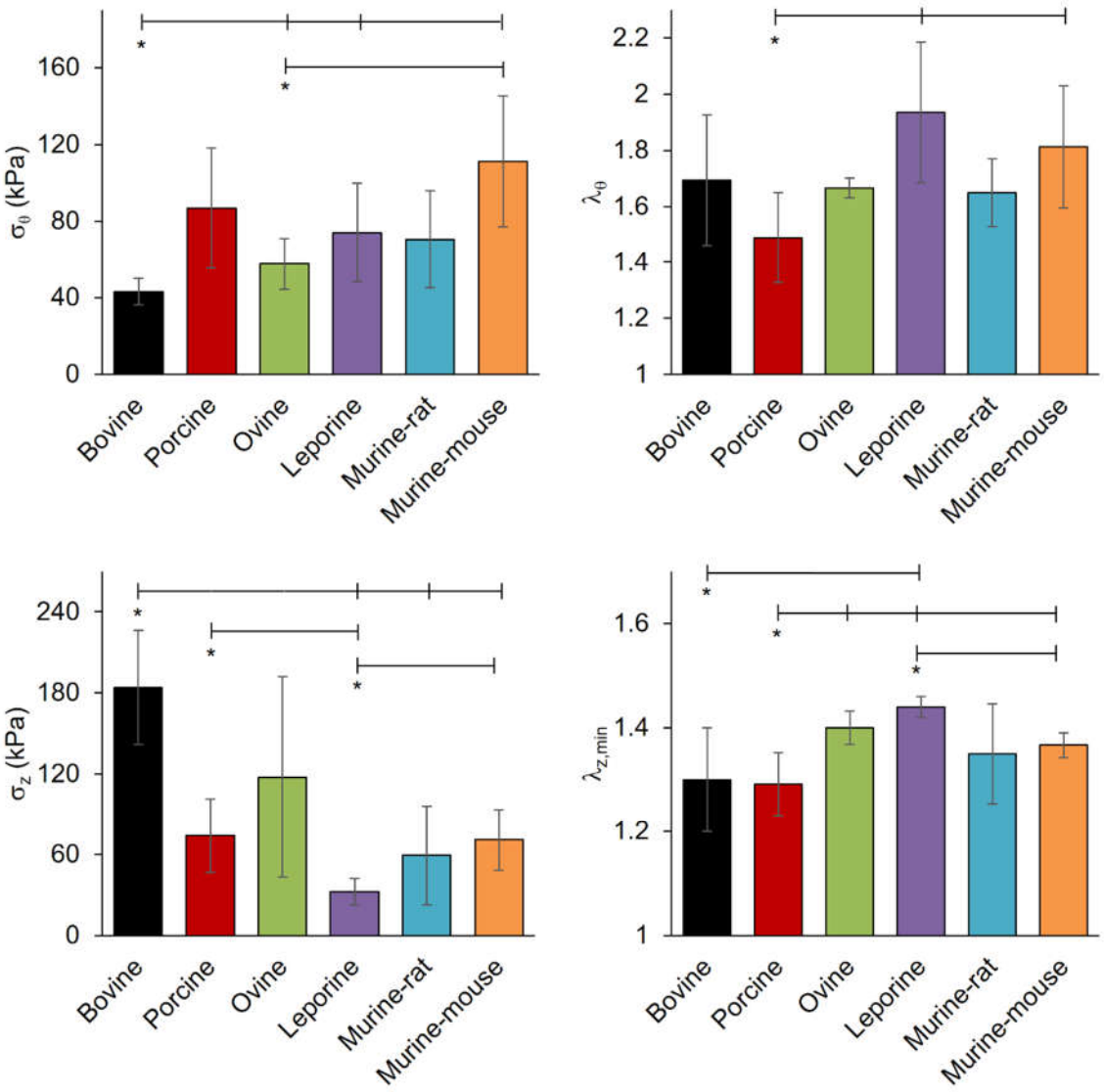

Figure 5.4 – Comparative stress and strain values for common carotid arteries subjected to passive biaxial mechanical testing at 100 mmHg. (a) Circumferential stress, (b) circumferential stretch, and (c) axial stress for bovine, porcine, ovine, leporine, murine-rat, and murine-mouse carotid arteries at 1.5 axial stretch ratio. Figure (d) illustrates the minimal axial stretch ratio to maintain vessels in tension at 100 mmHg. (*) denotes statistical significance at $p<0.05$ between the leftmost group and the corresponding hash-mark.

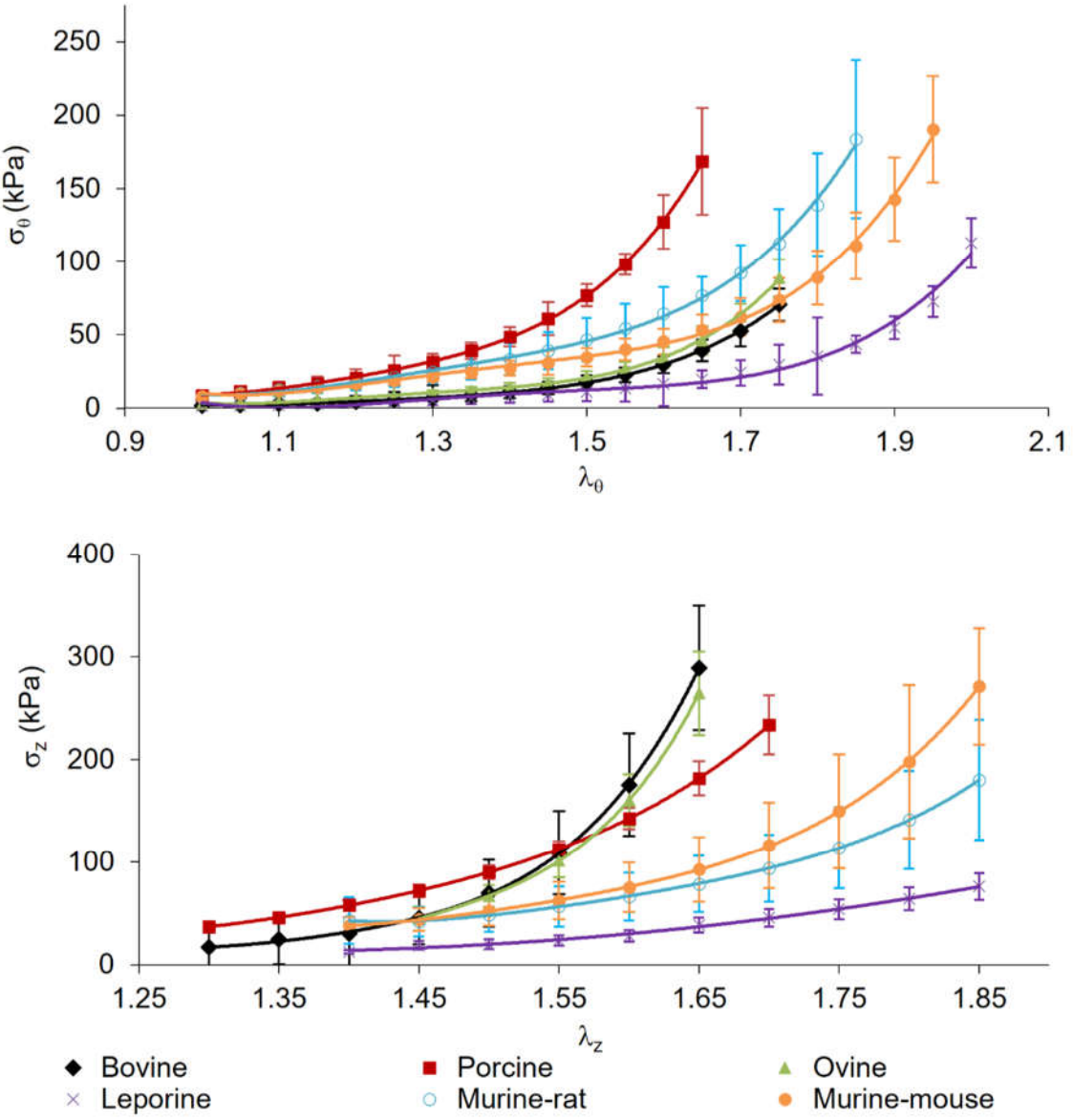

Figure 5.5 – Full range of stress and stretch for common carotid arteries subjected to passive biaxial mechanical testing. (top) Circumferential stress-stretch at λ_z=1.5, and (bottom) axial stress-stretch at 100 mmHg for bovine, porcine, ovine, leporine, murine-rat, and murine-mouse common carotid arteries fitted using the 4-fiber family HGO model. All values are mean (n=6) ± SEM.

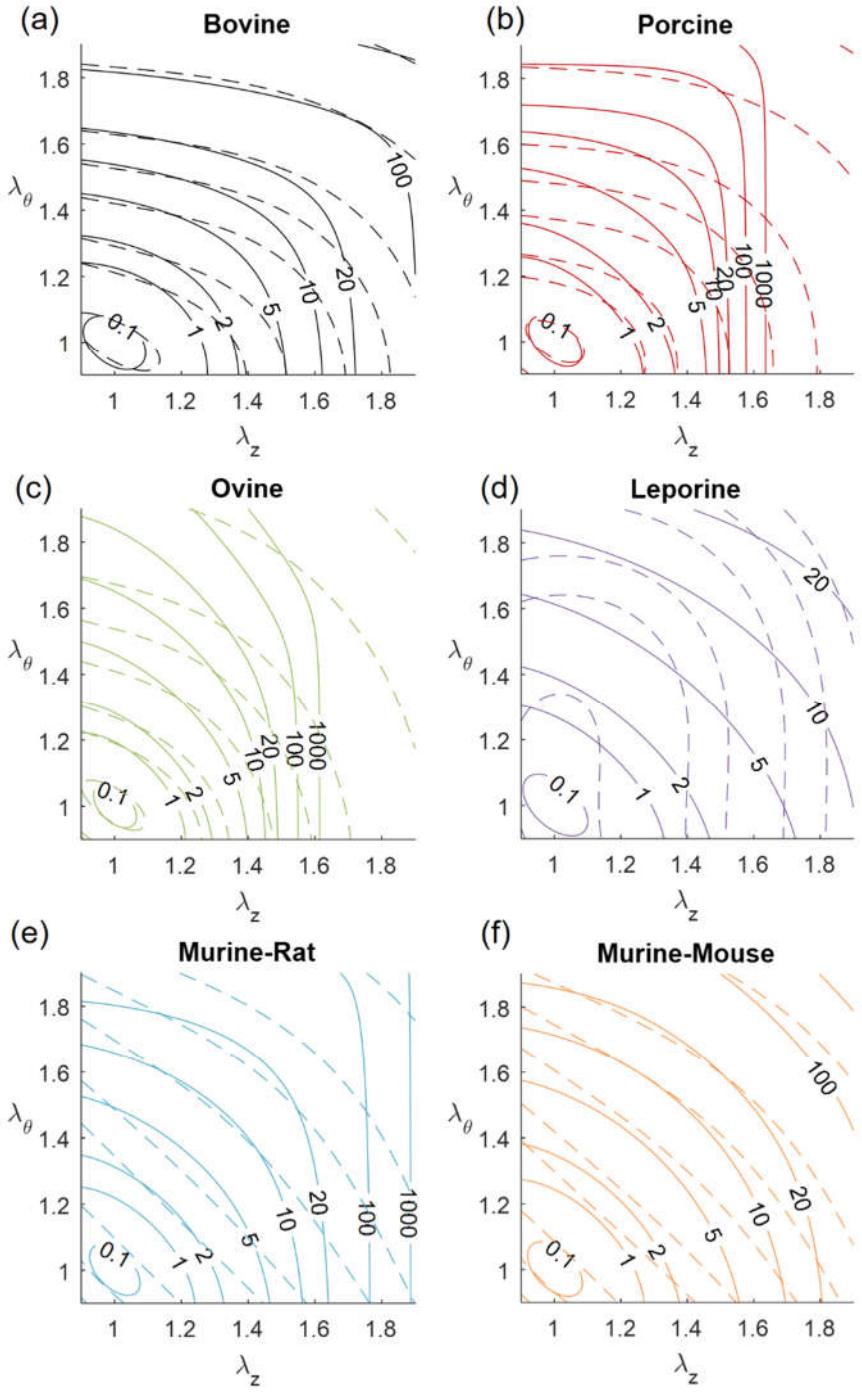

Figure 5.6 – Contour plots of total strain energy W (kPa or kJ/m^3). (a) Bovine, (b) porcine, (c) ovine, (d) leporine, (e) murine-rat, and (f) murine-mouse models as a function of biaxial stretches λ_θ=[1.00,1.85], λ_z=[1.00,1.85] using the Fung-type model (dashed lines) and 4-fiber HGO model (solid lines). Labels are provided for the 4-fiber HGO model only.

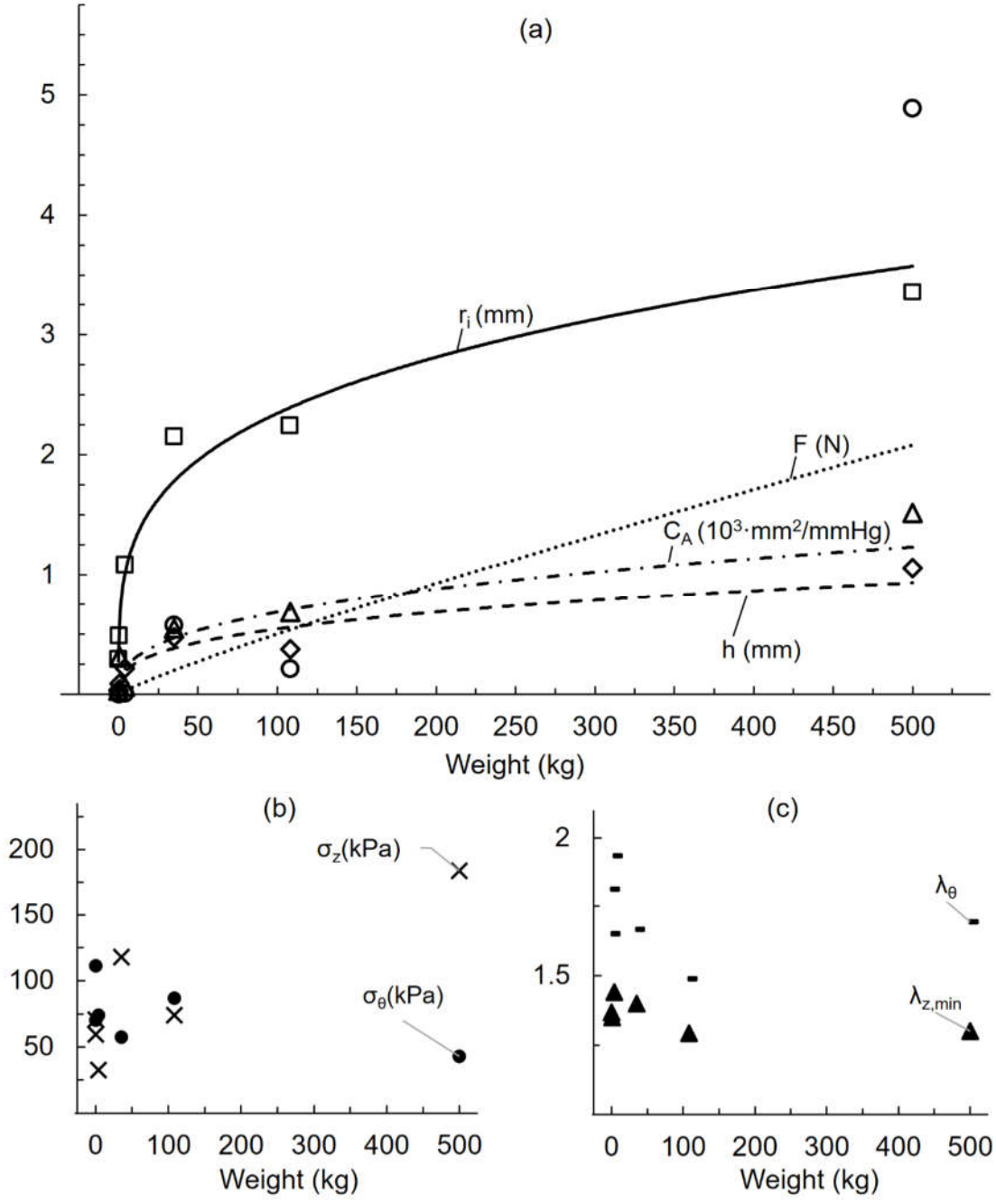

Figure 5.7 – Allometric scaling of mechanical quantities with weight. (a) Inner radius ($r_i = 0.702 \cdot w^{0.262}$, $R^2 = 0.982$), wall thickness ($h = 0.117 \cdot w^{0.3338}$, $R^2 = 0.968$), area compliance ($C_A = 0.129 \cdot w^{0.3633}$, $R^2 = 0.742$), and axial force ($F = 0.009 \cdot w^{0.8824}$, $R^2 = 0.900$) fit to the power law allometric scaling relationship. (b) Circumferential stress, axial stress, (c) circumferential stretch, and minimum axial stretch did not scale with weight.

CHAPTER 6

TRANSITION FROM VENOUS TO ARTERIAL LOADING IMPROVES SAPHENOUS VEIN REMODELING FOR CORONARY ARTERY GRAFTING[5]

[5] Prim, D. A., & Eberth, J. F. To be submitted to *Tissue Engineering Part A*.

6.1 ABSTRACT

When exposed to chronically altered mechanical stimuli, such as those resulting from coronary artery bypass grafting (CABG), remodeling process are activated that include cellular proliferation, migration, and differentiation and extracellular matrix protein deposition, degradation, and reorganization. These remodeling processes may be guided by an innate programming of resident vascular cell to regain some homeostatic state. Great saphenous veins (GSVs), one of the most common CABG conduits, fail more often than arterial conduits while also experiencing larger deviations from their homeostatic stress state, and an inability to effectively remodel in response to acute mechanical mismatch in the coronary circulation is thought to be a primary cause underlying pathologies leading to graft failure. These CABG failures often exhibit maladaptive remodeling, whereby nominally adaptive remodeling processes effect structural changes that result in the pathological occlusion of the graft lumen, called intimal hyperplasia, instead of restoration of mechanical homeostasis. We hypothesize that prolonged gradual transition from native GSV to CABG conditions might facilitate adaptive remodeling while preventing deleterious pathologies associated with acute changes to the mechanical loading environment. To test this hypothesis, we use an ex vivo perfusion bioreactor to guide remodeling of GSVs using stepwise incremental increases in pressure and volumetric flow every 3 days over the course of 21 day cultures. This approach will improve overall adaptation to the coronary environment by allowing for partial restoration of homeostatic stress states at each time point. Biaxial mechanical testing, gene expression, and histology are used to evaluate graft adaptation over the culture period. Preliminary results suggest this technique is capable of stimulating desirable

remodeling outcomes including increased inner radius and wall thickness, which lowers wall shear and circumferential stress towards native values.

6.2 INTRODUCTION

Stenosis and eventual failure of coronary artery bypass grafts (CABGs) generally follows a well characterized pattern of cell infiltration, proliferation, and ECM deposition that forms a new layer between the intima and media, narrowing the lumen and obstructing perfusion of the myocardium [248]. This process, known as intimal hyperplasia, is a primary cause of the 6% of CABGs that fail within the first year [14]. Moreover, multivessel disease and a lack of suitable autologous candidates leads to frequent use of great saphenous veins (GSVs) for CABG that fail at significantly higher rates in the near, mid and long term [13,14,16]. While this phenomenon is hardly controversial, researchers continue to work towards methods of remediation with little clinical success [247,249].

Experts widely accept that mechanical incompatibility plays a significant role in vein graft failure [250]. A classical and generally accepted theory in vascular mechanics contends that blood vessels are structured to optimally distribute loads in their local hemodynamic environment [120]. Resident vascular cells seek to maintain this configuration of optimal loading, which can be referred to as the homeostatic stress state. When changes to the local mechanical environment cause sustained deviation from this homeostatic stress state, vascular cells enact remodeling processes to restore homeostasis [8]. Indeed, previous investigations have demonstrated the capacity of vessels to restore homeostatic values of stress following perturbations to both wall shear [33,36] and circumferential stress [28,40] due to changes in blood flow and pressure respectively.

The use of GSVs for CABG results in transplantation from a relatively steady, low pressure, low flow environment to higher pressure, higher flow, and higher pulsatility of the coronary circulation. The acute mechanical deviations between autologous grafts and the coronary circulation can be very large, including increased circumferential stress, axial stress, and wall shear stress [15], which may be beyond the capacity of adaptive remodeling. Others have proposed a gradual approach to guiding the vein to artery adaptation, whereby the difference between native in situ loads and desired grafted loads would be divided into smaller steps or a continuous gradual increase [251]. Thus, each step would perturb the vessel's mechanical homeostasis enough to initiate remodeling but not so much that maladaptive remodeling or vessel injury is triggered. The vessel to be grafted would then be allowed to regain homeostasis before the next step change, and this process repeated until the graft vessel is at mechanical homeostasis at target loads [251]. Similarly, a constrained mixture model of vascular growth and remodeling has been proposed, with which simulations predict gradual loading would increase a vein's likelihood of successful adaptation [191].

In this investigation, we build upon our previous ex vivo culture experiments and apparatus to assess the effects of stepwise transition from venous to arterial hemodynamics on adaptive remodeling using a pulsatile perfusion bioreactor. As an approximation for circumferential stress and wall shear stress, pressure and flow are gradually increased at 3 day intervals over the course of 21 day cultures. We hypothesize that vessels experiencing gradual transition to coronary loading conditions, and in the absence of a systemic inflammatory system, should demonstrate adaptive growth and remodeling to be more mechanically suited to the coronary circulation, while avoiding intimal hyperplasia and

maladaptive remodeling. This adaptive remodeling, in theory, should include increased deformed inner radius, increased wall thickness, and increased compliance at arterial pressures without the thickened intima and denuded endothelium characteristic of early intimal hyperplasia.

6.3 MATERIALS AND METHODS

6.3.1 Tissue Harvesting and Preparation

GSVs were isolated from freshly slaughtered American Yorkshire sows (200 ± 20 kg; 36 ± 6 mo old) at a local abattoir and stored for transport on ice in Moscona's saline solution supplemented with 20 U/mL heparin, 1% penicillin/streptomycin, 1% amphotericin-B, and 1% gentamycin. All tissue used in this investigation originated from animals raised for consumption. As such, this investigation does not fall under IACUC protocol.

Under sterile conditions in a biological hood, excess perivascular tissue was removed with forceps and spring scissors, and branches were ligated with sterile 6-0 silk suture. For each vessel, one section approximately 40 mm in length was mounted to custom barbed glass cannulae within a glass bioreactor (Adams & Chittenden Scientific Glass, Berkeley, CA) and the sample was extended to 1.4x its unstretched (suture-to-suture) length to approximate in situ axial stretch, with this stretch ratio determined from preliminary mechanical testing of GSVs prior to culture. A second section 10-mm in length was mounted to barbed female luer lock fittings for day 0 biaxial mechanical testing.

6.3.2 Ex Vivo Vessel Culture

Detailed description of the bioreactor can be found in Chapter 3. Briefly, the glass vessel chamber was incorporated into a flow loop containing a roller pump, pressure

transducer, downstream resistor, and media reservoir, all contained within a sterile incubator at 37 C and 5% CO_2. Culture medium in the vessel chamber (150 mL) and reservoir/flow loop (300mL) was DMEM supplemented with 10% fetal bovine serum, 1% penicillin/streptomycin, 1% amphotericin-B, and 1% gentamycin, which was replaced every 7 days. GSVs were cultured for 21 days under either in situ loading conditions (Q = 0.17 mL/s; P = 15 mmHg) or stepwise loading from in situ to coronary loading conditions (Q = 0.52 mL/s; P = 102 mmHg). For each 3 day interval (21 days, 7 total), flow and pressure were calculated to achieve an equal percent increase at each step (Δ_Q = 17.3% and Δ_P = 31.5%) (Figure 6.1).

At the end of each culture, one section (15 mm) was cut from the middle of the sample and mounted to female barbed luer lock fittings for biaxial mechanical testing; one section (1 mm) was cut for tissue viability assessment; and one section (3 mm) was cut and immediately snap frozen on dry ice for gene expression analysis.

6.3.3 Biaxial Mechanical Testing

Biaxial inflation-extension testing was performed on sections of each sample vessel before (day 0: d0) and after (day 21: d21) culture under stepwise or venous perfusion, in similar fashion to our previous work using a customized Bose BioDynamic 5270 device [15,138]. Samples were secured to female barbed luer lock fittings using 3-0 braided silk suture, and unstretched suture-to-suture length was recorded. Samples were then mounted in the testing chamber of the device, taking care to avoid twisting or overstretching of the sample, and length of the axial control arms was adjusted to the previously recorded unstretched value. Axial force and luminal pressure gauges were tared after mounting but before data acquisition. The testing chamber and flow loop were filled with PBS

supplemented with 10^{-5} M sodium nitroprusside warmed to 37 C to ensure complete SMC relaxation.

After clearing all air bubbles from the flow loop, pressure was increased from 0-200 mmHg at increasing axial stretch ratios while taking note of the corresponding axial force values, and the axial stretch ratio at which axial force remained constant through pressurization was noted as the approximate in vivo stretch. Axial extension and pressurization and preconditioning protocols were performed prior to collecting data. For these, pressure was set to 100 mmHg, and samples were extended at 0.05 mm/s to the previously noted in vivo stretch ratio plus 10 percent for 8 cycles. Next axial displacement was set at the approximate in vivo ratio, and pressure was increased from 0-200 mmHg at 1 mmHg/s for 8 cycles. To calculate a more accurate in vivo stretch ratio, in consecutive trials vessels were pressurized to 60, 100, and 140 mmHg, axial stretch was increased from 1 to the approximate in vivo value plus 10%, and axial force was recorded throughout. When plotted together with axial extension versus axial force, the point at which the three curves intersected was assumed to be the true in vivo axial stretch ratio [136,137].

For data collection, samples were tested at three axial stretch ratios: the in vivo value, ~10% above in vivo, and ~10% below in vivo. At each stretch ratio, pressure was increased from 0-200 mmHg at 1 mmHg/s, and pressure, outer diameter, and axial force were recorded at 20 mmHg increments. This was repeated for 3 trials at each of the 3 stretch ratios.

6.3.4 Zero Stress Configuration

Following mechanical testing, ring sections 1 mm thick were cut from the center of tested samples, placed in a shallow dish of PBS, and images were collected using a DSLR

camera (Canon USA, Long Island, NY) mounted to a dissecting microscope (Carl Zeiss Microscopy GmbH, Jena, Germany) using an adapter lens (Micro Tech Lab, Graz, Austria). A radial stress-relieving cut was made in each ring, and the cut sectors were allowed to equilibrate for 20 minutes before images were collected of the stress-free configuration. ImageJ (NIH) was used to measure inner arc length L_i, outer arc length L_o, cross sectional area A, and opening angle Φ. From these data, stress-free thickness H could be calculated using

$$H = \frac{2A}{L_i + L_o} \ . \qquad [6.1]$$

6.3.5 Viability and Histological Analysis

At the termination of 21 day cultures, 1 mm ring sections were cut from perfused samples and incubated in 0.5 mg/ml methylthiazol tetrazolium (MTT; Sigma-Aldrich, Munich, Germany) in sterile Moscona's saline at 37 C for 1 hour. Images were collected using the microscope-mounted DSLR described above. Yellow MTT solution is reduced to an insoluble purple formazan product in the presence of metabolically active and viable cells, so relative tissue viability was quantified via threshold analysis of purple pixels to total cross-section area in ImageJ (National Institutes of Health).

Following biaxial mechanical testing at d0 and d21, sections were fixed in 4% paraformaldehyde. Fixed samples were embedded in paraffin, sectioned at 5 μm with a microtome and stained with hematoxylin/eosin. To assess apoptotic cells in the vessel wall via TUNEL staining, the In Situ Apoptosis Detection Kit (DAB) (Abcam, Cambridge, MA) was used in accordance the manufacturer's directions. A Nikon E600 microscope (Nikon Instruments, Melville, NY) with CCD camera and QCapture imaging software (QImaging, Surrey, BC) was used to collect digital images of stained slides.

ImageJ threshold analysis (NIH) of digital images was used to quantify the relative prevalence of apoptotic nuclei in TUNEL stained sections as a ratio of brown TUNEL positives regions to all nuclei stained blue with methyl green. Apoptotic nuclei were identified using the Threshold_Colour plugin as all brown regions greater than 20 pix^2 (hue: bandstop 126-211, saturation: bandpass 25-255, brightness: bandpass 0-220), and healthy nuclei were identified as all blue regions greater than 20 pix^2 (hue: bandpass 126-211, saturation: bandpass 25-255, brightness: bandpass 0-220) [147].

6.3.6 Data Analysis

We assume that vessels experience axisymmetric finite elastic deformation due to applied pressure and longitudinal extension and are 3-D thick-walled cylindrical tubes. By deactivating smooth muscle activity with sodium nitroprusside, we consider only the passive mechanical properties of the vessels resulting from extracellular matrix components – primarily collagen and elastin. Assuming tissue incompressibility, we calculate deformed inner radius r_i as

$$r_i = \sqrt{r_o^2 - \frac{A}{\pi \lambda_z}} \ , \qquad [6.2]$$

where outer radius r_o is measured and axial stretch λ_z is prescribed through biaxial testing. Using this data, mean circumferential σ_θ and axial σ_z wall stresses are calculated as

$$\sigma_\theta = \frac{P r_i}{r_o - r_i} \ , \quad \sigma_z = \frac{F}{\pi \left(r_o^2 - r_i^2 \right)} \ , \qquad [6.3]$$

where luminal pressure P is prescribed and axial force F is measured during testing. Mean circumferential λ_θ and axial λ_z stretch ratios are used as metrics of strain and are calculated as

$$\lambda_\theta = \frac{2\pi\left(r_i + r_o\right)}{L_i + L_o} \quad , \quad \lambda_z = \frac{l}{L} \quad , \qquad [6.4]$$

where l is the deformed length of the vessel segment and L the undeformed. Lumen area compliance was calculated as

$$C_A = \pi \frac{\Delta r_i^2}{\Delta P} \ , \qquad [6.5]$$

where Δr_i and ΔP are the change in deformed inner radius and pressure about approximate in vivo coronary pressure of 100 mmHg.

Ongoing work will quantify the changes across samples before and after culture through continuum mechanics analysis using a structure-based constitutive model.

6.4 RESULTS

As preliminary data leading to a desired sample size of six successful cultures, five GSVs were cultured to completion at 21 days following stepwise increases in pressure and volumetric flow (Figure 6.1). Of these five vessels, two (S2, S7) demonstrate substantial viability through MTT assay and vasoreactivity, while three (S5, S6, S8) demonstrate limited viability (Figure 6.2). Similar results are found for H&E and TUNEL staining (Figure 6.3). Samples that remained viable throughout the duration of testing show little histological difference in the media and adventitia (Figure 6.3 A-B), but cultured samples do show endothelial loss ranging from partial to complete denudation as well as disruption of the internal elastic lamina (Figure 6.3B). In the same viable sample, 6.79% of nuclei stain are positive for TUNEL staining at day 0 versus 21.04% positive at day 21 (Figure 6.3 C-D). Ongoing experiments will also include control samples cultured under unchanged venous flow and pressure for 21 days, but none have been completed successfully at this time.

Geometric measurements of zero stress configuration suggest increases in all metrics from day 0 to day 21: inner arc L_i, outer arc L_o, opening angle OA, cross sectional area A, and wall thickness H. However, these increases are not significant owing to large variations, especially in the cultured group (Table 6.1). Increased L_i and L_o suggest increases in inner and outer diameter in the closed configuration, which is borne out in the pressure diameter relationships between day 0 and day 21 (Figure 6.4). As the sample sizes increase, we hope to reach statistical significance in this metric.

Biaxial inflation-extension data is presented for all paired cultures (Figure 6.4) and for the two paired cultures demonstrating the best viability (Figure 6.5). Some qualitative differences appear between cultured and uncultured vessels when all samples are compared; however, no clear patterns are immediately apparent. For the vessels identified as viable at 21 days, circumferential and axial stress versus stretch curves show a noticeable shift, with vessels experiencing less circumferential deformation and also lower values of stress at similar applied pressure values, suggesting both a thickening and stiffening of the vessel wall. Axially, calculated "in vivo" stretch ratios increase after stepwise culture, meaning unstretched length decreases (Figure 6.5 D). Concurrently, axial force values generated at in vivo stretches increases dramatically (Figure 6.5 C).

To facilitate comparison under similar conditions, structural and mechanical values were plotted for each sample before and after culture under 100 mmHg applied pressure and calculated in vivo axial stretch (Figure 6.6). Notably, several metrics show opposite temporal patterns for the samples that did (S2, S7) and did not (S5, S6, S8) maintain viability through day 21. Deformed wall thickness (h) nearly doubles from day 0 to day 21 for viable samples, while not changing or decreasing in non-viable samples. Similarly,

axial force (F) and axial stress (σ_z) increase dramatically in viable samples but decrease or remain relatively unchanged in non-viable samples. Conversely, circumferential stress (σ_θ) and circumferential stretch (λ_θ) decrease significantly in viable samples but remain unchanged or increases in non-viable samples. Deformed inner radius (r_i) and lumen area compliance (C_A) do not show a clear pattern between viable and non-viable cultures from day 0 to day 21; samples S2 follows a similar pattern to nonviable cultures, with r_i slightly increasing and C_A decreasing. Conversely sample S7 shows a large decrease in r_i and large increase in C_A.

6.5 DISCUSSION

In this investigation, we build upon previous observational studies of ex vivo CABG perfusion in an attempt to guide adaptive remodeling through stepwise increases in mean media pressure and volumetric flow rate from native GSV to grafted LAD hemodynamic-replicated values over 21 day cultures. The primary indicator of success herein is restoration of native homeostatic stress values while maintaining viable tissue through 21 days of culture. We have previously quantified the amount of mechanical deviation between GSVs in their native conditions and under acute coronary loads representative of standard grafting procedures, specifically quantifying differences in deformed inner radius, compliance, circumferential stress, and axial stress between venous and arterial conditions [15]. Not surprisingly, each of these metrics show large deviations between native and grafted loading conditions, which were quantified by the normalized metrics Ω and Ξ. Thus when applied to the present study, reductions in post-culture Ω and Ξ compared to fresh GSVs or controls would suggest remodeling towards adaptation to the

coronary circulation. Secondary analyses that support mechanical changes include quantification of apoptosis, expression of remodeling-associated genes, and histological changes in vessels

These experiments are ongoing, so the results included herein should be considered preliminary and inconclusive at this time. Of 8 attempts to date, 5 samples were cultured for 21 days and subjected to mechanical testing at the culmination of the experiment. Of those 5 samples, 2 indicated largely viable tissue at day 21, while the other 3 indicated significantly less viability through the use of the MTT assay. This viability also correlated with significant remodeling towards restoration of homeostatic stress levels as quantified by increased r_i and h, leading to reduction in τ_w and σ_θ under coronary loads when compared to uncultured vessels. In the present data, no significant changes are seen in opening angle because of ex vivo culture. Nonetheless, ongoing studies will continue to evaluate whether patterns arise, as decreases in opening angle suggest outward remodeling which would be a positive indicator of success, while increases in opening angle suggests inward remodeling that may be considered maladaptive.

Ongoing experiments and future investigations should seek to understand and improve upon the differential viability across cultures. Intuitively, diminished viability – even if it is eventually restored – mitigates vessels' ability to restore mechanical homeostasis, as resident vascular cells are the mediators of remodeling processes. Potential factors that could affect viability may include injury from dissection and experimental setup, inappropriate gas or nutrient exchange, and bioreactor contamination. Each must be addressed to improve experimental results and enable further translational applications.

In this investigation we focus on a single experimental approach to guided remodeling using increments of equal percentage increase in luminal pressure and volumetric flow at 3 day intervals over 21 days of culture. While collagen generally has a half-life of weeks to months in quiescent tissues, some have found evidence of much higher rates in cardiovascular and other tissues [47,252,253]. Further, in vivo experiments have shown wall thickening over 80% within 21 days [254], so it is reasonable to suspect significant structural remodeling even if homeostasis is not fully regained under coronary conditions. While we believe this investigation represents a useful starting point and proof of concept for guided remodeling in ex vivo culture, one could imagine virtually infinite permutations of time intervals, step size, and individual adjustment of pressure and flow rate.

Further, while flow rate and pressure directly correlate to τ_w and σ_θ, we do not calculate stresses in real time, requiring a direct measure of inner diameter. The most widely accepted view of mechanical homeostasis and remodeling is that stresses correlate most closely with tissue homeostasis and deviations in stresses from homeostasis drive remodeling [255]. While we can directly estimate stresses (τ_w and σ_θ) from applied loads (Q and P) at the beginning of the study, if we assume that remodeling occurs over the course of the 21 day cultures, then we cannot calculate stresses in real time and thus do not know whether samples have restored homeostatic stress values. Conversely, some believe that structural remodeling occurs over weeks as opposed to days; if that hypothesis is true then morphological changes may be limited enough through 21 days to make reasonable stress approximations. Thus, another potential improvement on this study design may be to add hardware to measure inner radius in culture, use those values to calculate stresses in

real time, and base step timing and magnitude on restoration of homeostasis versus set time points, which has been theorized previously [251].

If the ongoing results of this study validate ex vivo conditioning of GSVs towards desired mechanical outcomes for CABG, this technique can be adapted for other graft tissues and procedures such as a modulated arteriovenous fistulae and peripheral artery bypass. Hypothetically, the methods described herein could be applied to any graft loading environment. Given any source tissue and its native loading conditions (i.e., P and Q) and loading conditions in the targeted graft environment, the source tissue could be conditioned in a gradual manner until homeostasis is reached under the target loading conditions. Success in this area would expand the number of vessels that could be used as grafts, as theoretically any viable blood vessel could be adapted to any loading environment given sufficient ex vivo conditioning. Additionally, vascular grafts could be utilized for previously "ungraftable" situations where no autologous source vessel has been available that matches the target graft environment.

Similar techniques could be utilized as a tool in developing tissue engineered vascular grafts by stimulating seeded cells to organize themselves and extracellular matrix towards desired mechanical properties. Many tissue engineered blood vessel designs have been proposed that involve cells seeded to both biological and artificial scaffolds [126,247,256–258], and our technique for ex vivo vascular conditioning could be applied to any of these designs to ensure that the graft is ideally suited to the mechanical loads of its target environment. One application of particular interest involves the combination of ex vivo conditioning with decellularized scaffolds seeded with human vascular cells. In this case, a scaffold could be obtained from an animal model, allowing for a nearly

unlimited supply and selection of geometries and native mechanical properties based on the eventual graft location. After decellularization, scaffolds could be seeded with cells from the patient requiring surgery and cultured under loading conditions that exactly match the patient's circulation until the cells remodel the scaffold sufficiently to reach homeostasis before implantation. Although we are yet to test this technique, based on preliminary results and others' investigations, we believe this type of application has the potential to drive significant changes to the field of vascular grafting.

6.6 TABLES

Table 6.1 – Stress-free configuration comparison between fresh GSVs (n=8) and those cultured for 21 (n=5) days under stepwise guided remodeling.

	L_i (mm)	L_o (mm)	OA (°)	A (mm^2)	H (mm)
Day 0	8.15 ± 0.90	10.96 ± 0.94	64.70 ± 33.75	7.73 ± 2.08	0.80 ± 0.17
Day 21	9.51 ± 1.82	12.67 ± 2.13	77.11 ± 50.71	11.17 ±6.95	0.95 ± 0.44

6.7 FIGURES

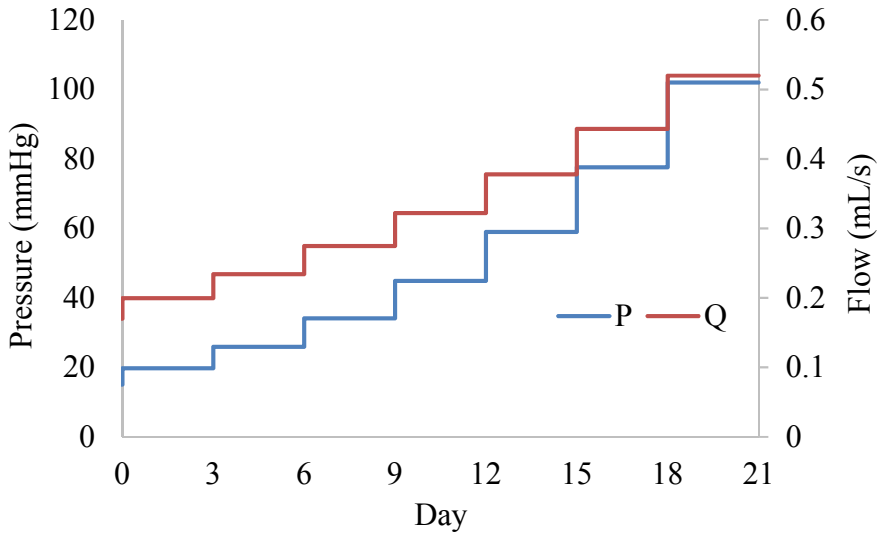

Figure 6.1 – Stepwise increases in pressure (P) and volumetric flow (Q) at 3 day intervals over 21 days of culture. Flow increases by 17.3% each step and pressure by 31.5%

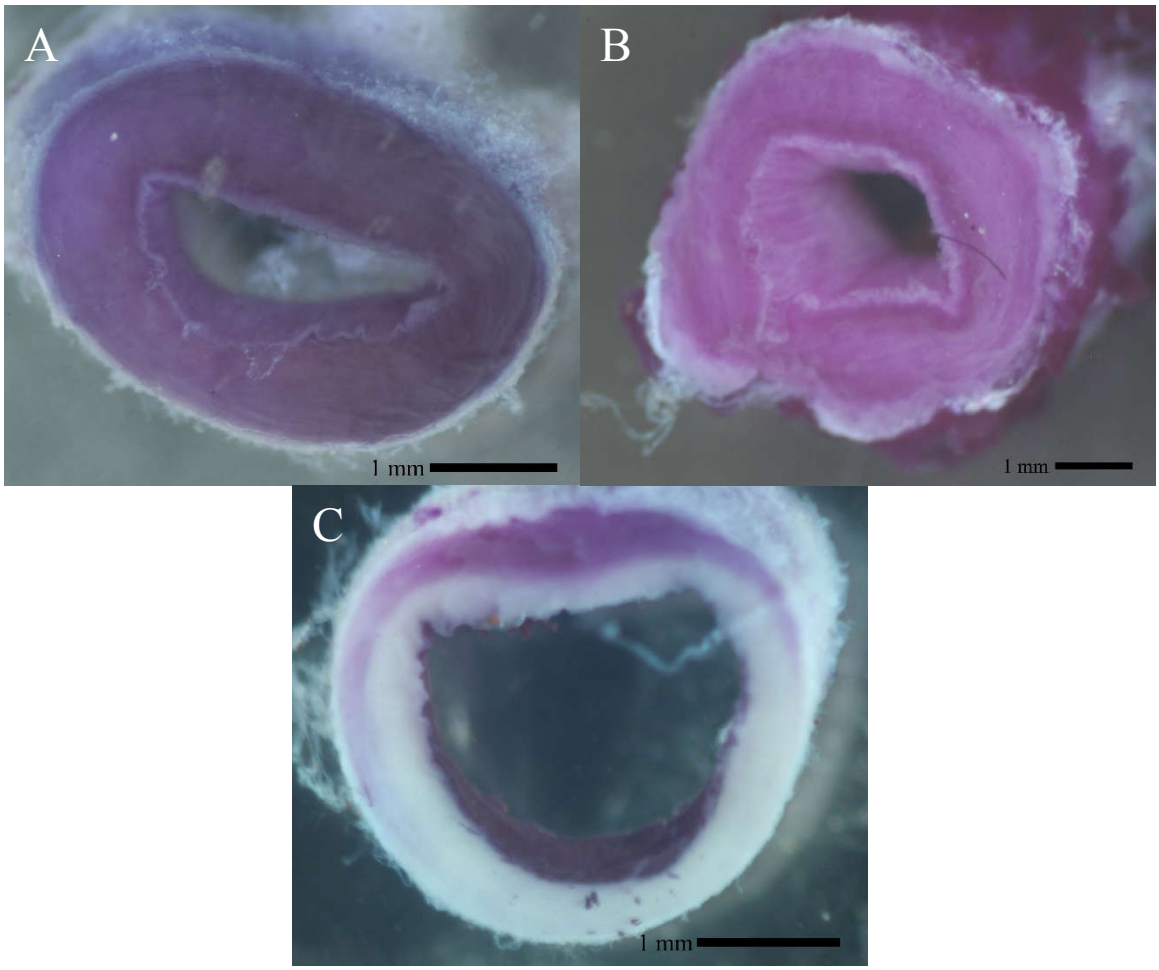

Figure 6.2 – Representative MTT stained rings of (A) fresh GSV, (B) viable 21 day stepwise culture, and (C) 21 day stepwise culture with limited viability.

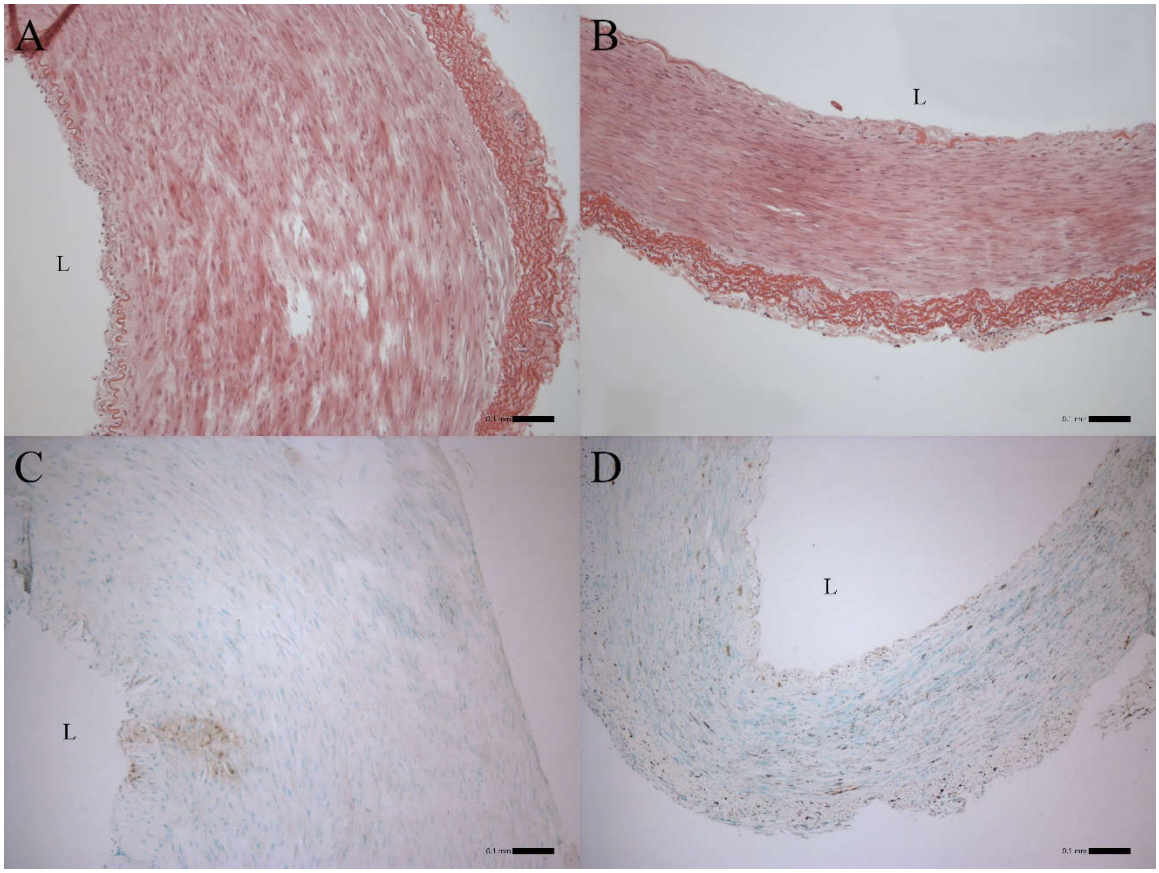

Figure 6.3 – Top: H&E staining of GSV sample (A) prior to culture and (B) after 21 day stepwise remodeling culture; Bottom: TUNEL apoptosis assay with DAB conjugation and methyl green counterstain (C) prior to culture and (D) after 21 day stepwise remodeling culture. In each image, lumen marked with L and scale bar = 1mm.

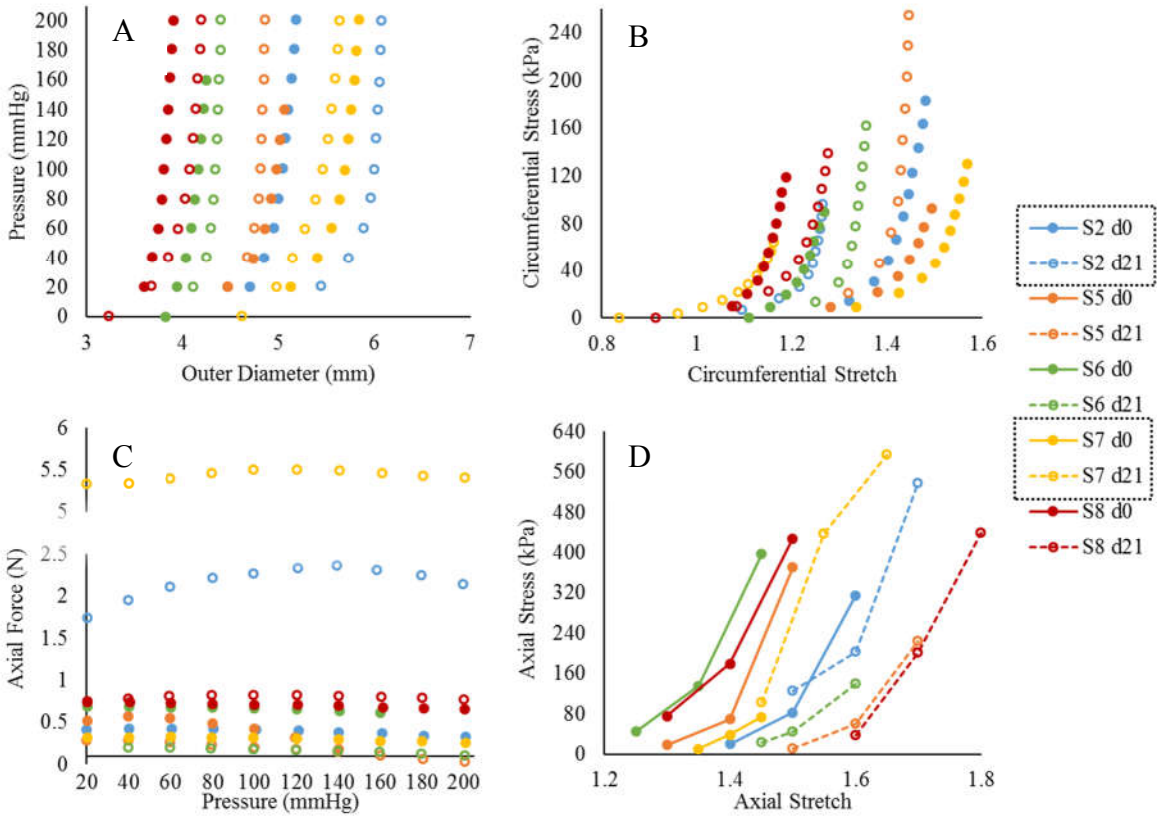

Figure 6.4 – Biaxial mechanical data from inflation-extension testing of 5 vessels before and after 21 day stepwise remodeling culture: (A) pressure vs. diameter relationship at each vessel's in vivo axial stretch (λ_z), (B) circumferential stretch (λ_θ) vs. circumferential stress (σ_θ) at each vessel's in vivo axial stretch, (C) pressure vs. axial force at each vessel's in vivo axial stretch, (D) axial stretch vs. axial stress at 100 mmHg. Closed circles – day 0, open circles – day 21; hashed boxes around legend denote vessels that remained viable through day 21.

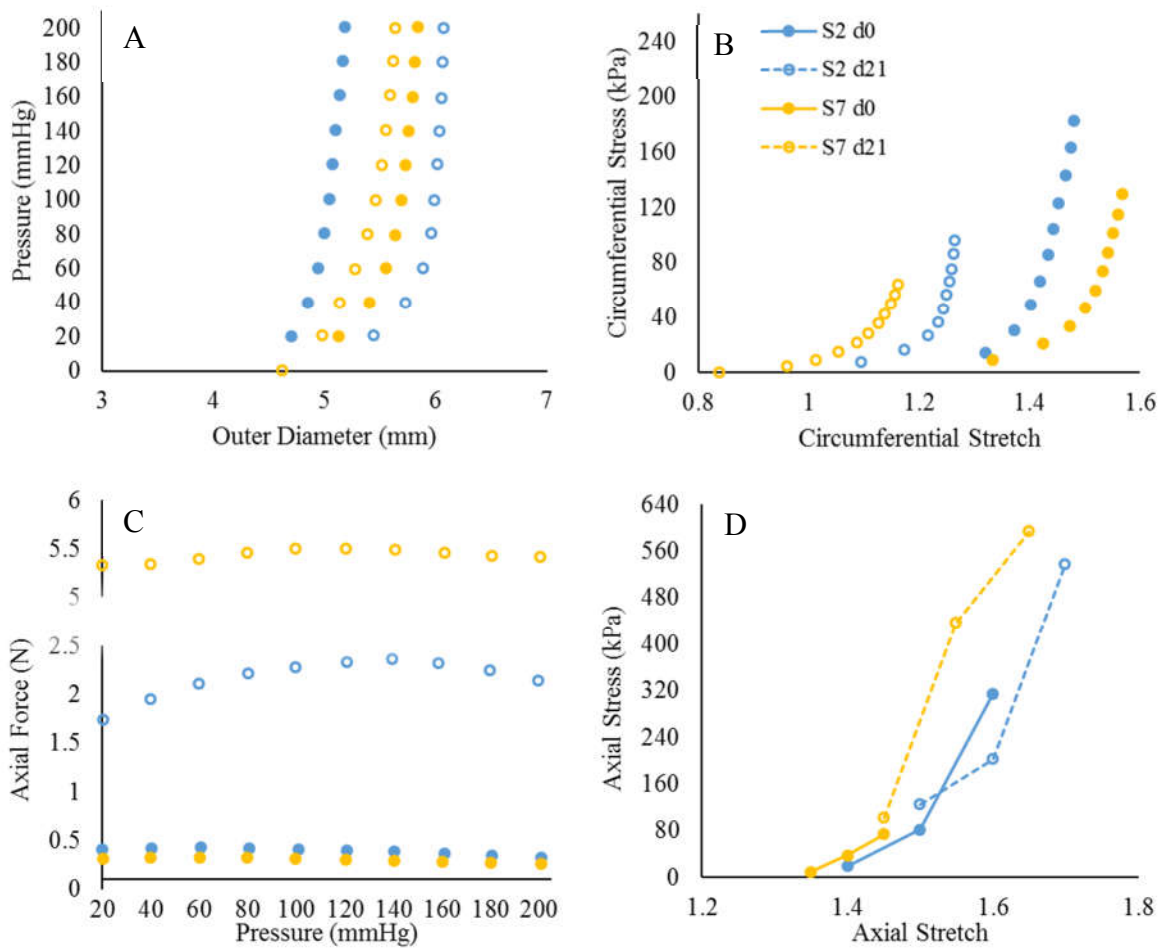

Figure 6.5 Biaxial mechanical data from inflation-extension testing of 2 vessels that maintained viability after 21 day stepwise remodeling culture: (A) pressure vs. diameter relationship at each vessel's in vivo axial stretch (λ_z), (B) circumferential stretch (λ_θ) vs. circumferential stress (σ_θ) at each vessel's in vivo axial stretch, (C) pressure vs. axial force at each vessel's in vivo axial stretch, (D) axial stretch vs. axial stress at 100 mmHg. . Closed circles – day 0, open circles – day 21

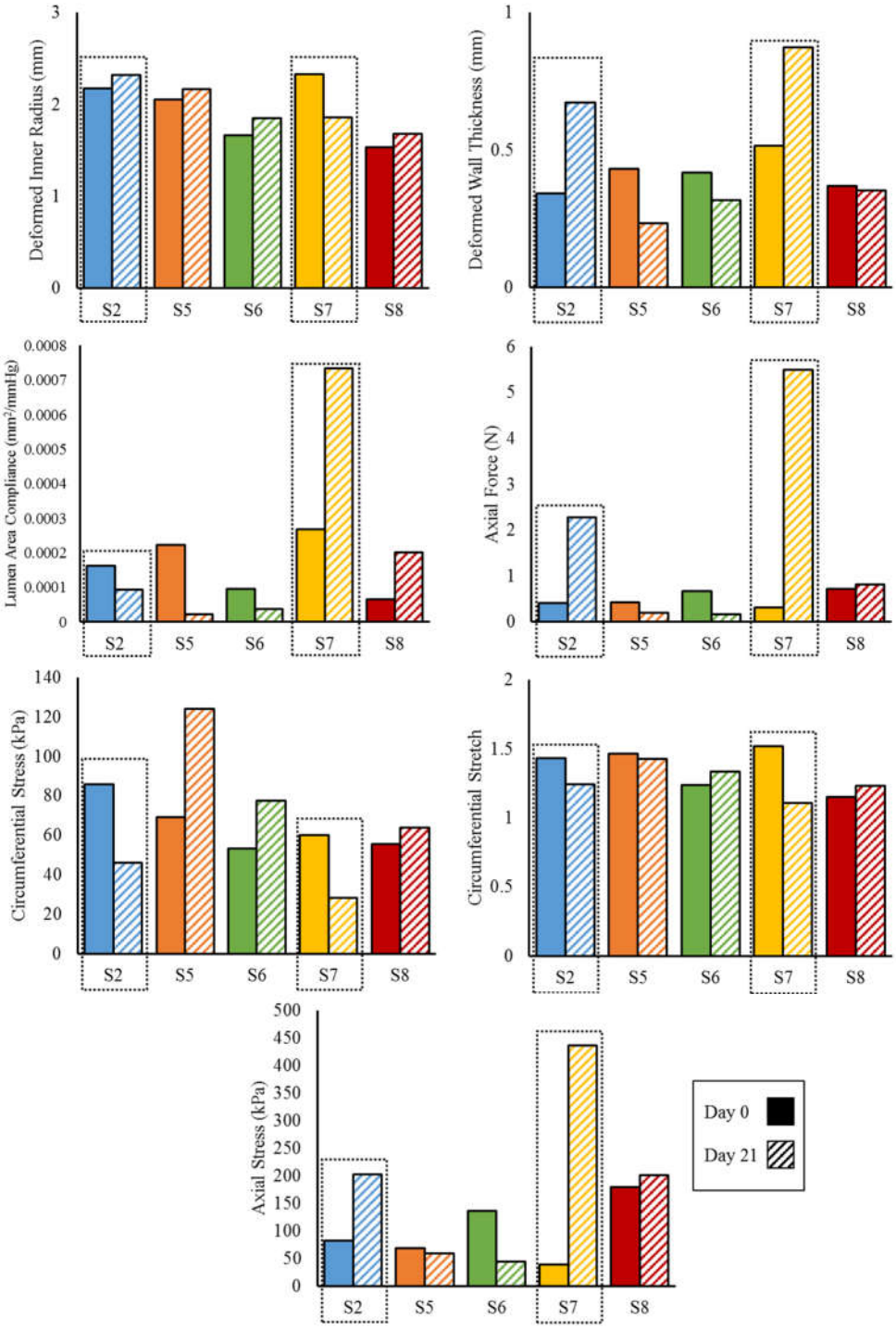

Figure 6.6 – Comparison of changing structural and mechanical properties before and after 21 day remodeling culture in individual samples at in vivo stretch ratio and 100 mmHg pressure. Hashed boxes denote samples that maintained viability through day 21.

CHAPTER 7

CONCLUSIONS AND FUTURE DIRECTIONS

Vascular mechanics and remodeling are an important yet under-investigated aspect of coronary artery bypass grafting. Blood vessels, like other tissues, sense and respond to the mechanical and biochemical stimuli imposed upon them through growth and development, which guides the mature structure of the vessel. This creates a relationship between structure and function whereby blood vessels at any location in the vascular tree are uniquely suited to mechanical loads and physiological demands of that particular microenvironment. Thus, the vessel exists at homeostasis with its mechanical environment. When the local mechanical environment is disturbed, resident vascular smooth muscle cells sense these changes through cell-cell and cell-matrix junctions and respond by contracting or relaxing to alter vessel tone and redistribute the altered loads. When mechanical disturbances persist for days, weeks, and months, these and other resident vascular cells respond by enacting remodeling process to alter the geometry and composition of the vessel to restore its homeostatic state and function effectively in the new loading environment.

Clinicians have long speculated that differences in local mechanics between source tissues and their grafted environment could be a factor in graft efficacy, as early observations – later confirmed through experimentation – often showed differences in important graft characteristics like compliance, inner radius, and vessel histology, which correlate with decreased patency in many grafts. In Chapter 2 of this dissertation, we quantified the passive biaxial mechanics of one coronary artery – the LAD – and three

common CABG vessels – the ITA, RA, and GSV. By utilizing a continuum mechanics approach, we directly compared the mechanical properties of each tissue under native and grafted conditions and findings suggested that the magnitude of mechanical deviation from the native to grafted state of important graft parameters – circumferential stress, axial stress, compliance, and deformed inner radius – directly correlates with observed clinical failure rates across these vessels.

As grafting inherently disturbs the local mechanical environment of source tissues, remodeling processes must act to restore homeostasis and maximize functionality of grafts in their new environment. Overall processes that can result from remodeling – diameter changes, wall thickening, protein deposition, etc. – are relatively well established, but it is unclear whether discrete individual vessels and resident vascular cells therein are equally capable of adaptive remodeling. Thus, in Chapter 3 we compared the cells of the ITA, RA, and GSV, as well as the overall tissue response ex vivo to coronary loading to find that differences exist in cell proliferation and tissue level gene expression across source tissues. Chapter 6 builds upon these findings by seeking to stimulate adaptive remodeling in the GSV through prolonged ex vivo tissue culture, and preliminary results suggest an ability to promote remodeling and improved compatibility with the coronary circulation without triggering maladaptive processes.

An often-overlooked aspect of ex vivo vascular culture has been the sensitivity of resident vascular cells to hemodynamics with respect to remodeling. Others have demonstrated cellular sensitivity to harmonic frequencies beyond the primary pulse pressure, but very few investigations have taken this into account for ex vivo tissue culture. In Chapter 4, we designed and validated a novel perfusion bioreactor capable of recreating

physiological flows across different vessels and species. From this work, we noticed that the cultured vessels, in this case GSVs, were sensitive to arterial waveforms. We also noticed that tissues were highly sensitive to the culture process alone. In ongoing work in our lab and future investigations, this bioreactor is being used to determine if accurate hemodynamic replication is necessary to guide adaptive remodeling. Further, we are currently using this biomimetic perfusion bioreactor in concert with next generation sequencing to evaluate the biochemical pathways that are sensitive to hemodynamic intricacies. This approach should inform improved experimental design by knowing to what extent physiological flow and pressure waves should be replicated to effect desired remodeling outcomes. By understanding the molecular pathways that are sensitive to specific aspects of flow and pressure waves, we can identify therapeutic targets to enhance desired remodeling outcomes and inhibit maladaptive pathways.

Traditional CABG procedures – and other small diameter graft applications – are constrained by the limited availability of suitable autologous conduits, with GSVs being the most used but not necessarily most effective source, while tissue engineered vascular grafts to date have not demonstrated sufficient efficacy in small diameter applications. As more people require more grafts – multiple CABGs, peripheral artery bypass, etc. – reliable engineered options would be a valuable tool to clinicians. An ongoing area of research in our lab and others involves the use of decellularized animal tissues as a xenograft scaffold that could then be seeded and treated to function as a vascular graft in man. In the process of decellularization, biological antigens are removed, opening the possibility of using non-human decellularized vessels as scaffolds to be seeded with human cells. In this scenario, a donor scaffold could be selected across multiple vessel types from multiple species based

on patient-specific geometry and desired mechanical properties. In Chapter 5, we evaluate the passive biaxial mechanical properties of carotid arteries across six species of mammals to show that some but not all mechanical properties scale allometrically and provide a framework for a future catalog of decellularized graft scaffolds. The implications for the current research project are that the biophysical properties of these grafts could actually be enhanced prior to implantation. For example, a decellularized scaffold from any desired source could be seeded with progenitor or mature vascular cells and cultured under the exact mechanical and hemodynamic environment for which it is intended, allowing the cells to remodel the scaffold as necessary to reach homeostasis prior to implantation and, in theory, requiring little to no adaptation once grafted.

Future investigations can synthesize the knowledge generated herein with respect to autologous graft tissues to better design and characterize engineered blood vessels. Cardiovascular disease continues to be a leading cause of mortality and morbidity in the developed world, reducing the quality of life for millions of people and resulting in billions of dollars in direct and indirect monetary burden. Healthy vasculature is imperative to the optimal function of every tissue in the body, and hopefully the knowledge presented in this dissertation will be used to create better vascular grafts that restore health to those in need.

REFERENCES

1. Gault JH, Ross J, Mason DT. Patterns of brachial arterial blood flow in conscious human subjects with and without cardiac dysfunction. Circulation. Am Heart Assoc; 1966;34: 833–848.
2. Berne RM, Levy MN. Cardiovascular physiology [Internet]. Mosby; 2001. Available: http://books.google.com/books?id=CNlqAAAAMAAJ
3. Abraham P, Leftheriotis G, Desvaux B, Saumet M, Saumet L, Saumet JL. Diameter and blood velocity changes in the saphenous vein during thermal stress. Eur J Appl Physiol Occup Physiol. 1994/01/01. 1994;69: 305–308.
4. Chuong CJ, Fung YC. Three-dimensional stress distribution in arteries. J Biomech Eng. American Society of Mechanical Engineers; 1983;105: 268–274.
5. Holzapfel GA, Gasser TC, Ogden RW. A new constitutive framework for arterial wall mechanics and a comparative study of material models. J Elast. Kluwer Academic Publishers; 2000;61: 1–48. doi:10.1023/A:1010835316564
6. Baek S, Gleason RL, Rajagopal KR, Humphrey JD. Theory of small on large: potential utility in computations of fluid–solid interactions in arteries . Comput Methods Appl Mech Eng. 2007;196: 3070–3078.
7. Gaudino M, Taggart D, Suma H, Puskas JD, Crea F, Massetti M. The Choice of Conduits in Coronary Artery Bypass Surgery. J Am Coll Cardiol. Journal of the American College of Cardiology; 2015;66: 1729–1737. doi:10.1016/j.jacc.2015.08.395

8. Humphrey JD. Cardiovascular Solid Mechanics: Cells, Tissues, and Organs [Internet]. Springer; 2002. doi:10.1007/978-0-387-21576-1

9. Majesky MW. Adventitia and perivascular cells. Arterioscler Thromb Vasc Biol. American Heart Association, Inc.; 2015;35: e31-5. doi:10.1161/ATVBAHA.115.306088

10. Mueller RL, Rosengart TK, Isom OW. The History of Surgery for Ischemic Heart Disease. Ann Thorac Surg. Elsevier; 1997;63: 869–878. doi:10.1016/S0003-4975(96)01375-6

11. Benjamin EJ, Blaha MJ, Chiuve SE, Cushman M, Das SR, Deo R, et al. Heart Disease and Stroke Statistics—2017 Update: A Report From the American Heart Association. Circulation. 2017;135: e146 LP-e603. Available: http://circ.ahajournals.org/content/135/10/e146.abstract

12. Al-Sabti HA, Al Kindi A, Al-Rasadi K, Banerjee Y, Al-Hashmi K, Al-Hinai A. Saphenous vein graft vs. radial artery graft searching for the best second coronary artery bypass graft. J Saudi Hear Assoc. 2013/11/08. 2013;25: 247–254. doi:10.1016/j.jsha.2013.06.001

13. Benedetto U, Raja SG, Albanese A, Amrani M, Biondi-Zoccai G, Frati G. Searching for the second best graft for coronary artery bypass surgery: a network meta-analysis of randomized controlled trials. Eur J Cardiothorac Surg. 2014/03/30. 2015;47: 59–65. doi:10.1093/ejcts/ezu111

14. Carey JS, Danielsen B, Milliken J, Li Z, Stabile BE. Narrowing the gap: Early and intermediate outcomes after percutaneous coronary intervention and coronary artery bypass graft procedures in California, 1997 to 2006. J Thorac Cardiovasc Surg.

Elsevier; 2009;138: 1100–1107. doi:10.1016/j.jtcvs.2009.03.069

15. Prim DA, Zhou B, Hartstone-Rose A, Uline MJ, Shazly T, Eberth JF. A mechanical argument for the differential performance of coronary artery grafts. J Mech Behav Biomed Mater. 2016;54: 93–105. doi:10.1016/j.jmbbm.2015.09.017

16. Goldman S, Zadina K, Moritz T, Ovitt T, Sethi G, Copeland JG, et al. Long-term patency of saphenous vein and left internal mammary artery grafts after coronary artery bypass surgery: Results from a Department of Veterans Affairs Cooperative Study. J Am Coll Cardiol. Elsevier; 2004;44: 2149–2156. doi:10.1016/J.JACC.2004.08.064

17. Samano N, Geijer H, Liden M, Fremes S, Bodin L, Souza D. The no-touch saphenous vein for coronary artery bypass grafting maintains a patency, after 16 years, comparable to the left internal thoracic artery: A randomized trial. J Thorac Cardiovasc Surg. Elsevier; 2015;150: 880–888. doi:10.1016/j.jtcvs.2015.07.027

18. Athanasiou T, Saso S, Rao C, Vecht J, Grapsa J, Dunning J, et al. Radial artery versus saphenous vein conduits for coronary artery bypass surgery: forty years of competition--which conduit offers better patency? A systematic review and meta-analysis. Eur J Cardiothorac Surg. 2010/12/21. 2011;40: 208–220. doi:10.1016/j.ejcts.2010.11.012

19. Davies MG, Hagen PO. Pathobiology of intimal hyperplasia. Br J Surg. 1994/09/01. 1994;81: 1254–1269.

20. Tennant M, Dilley RJ, McGeachie JK, Prendergast FJ. Histogenesis of arterial intimal hyperplasia and atherosclerosis. Aust N Z J Surg. 1990;60: 79–85.

21. Ruengsakulrach P, Sinclair R, Komeda M, Raman J, Gordon I, Buxton B.

Comparative Histopathology of Radial Artery Versus Internal Thoracic Artery and Risk Factors for Development of Intimal Hyperplasia and Atherosclerosis. Circulation. 1999;100: II-139-Ii-144. doi:10.1161/01.CIR.100.suppl_2.II-139

22. Davies MG, Hagen PO. Reprinted article "Pathophysiology of vein graft failure: a review." Eur J Vasc Endovasc Surg. 2011;42 Suppl 1: S19-29. doi:10.1016/j.ejvs.2011.06.013

23. de Vries MR, Quax PHA. Inflammation in Vein Graft Disease. Front Cardiovasc Med. Frontiers; 2018;5: 3. doi:10.3389/fcvm.2018.00003

24. Osgood MJ, Hocking KM, Voskresensky I V., Li FD, Komalavilas P, Cheung-Flynn J, et al. Surgical vein graft preparation promotes cellular dysfunction, oxidative stress, and intimal hyperplasia in human saphenous vein. Journal of Vascular Surgery. 2014. doi:10.1016/j.jvs.2013.06.004

25. Ludwig R, Virchow K. Cellular pathology [Internet]. John Churchill; 1860. Available: https://books.google.com/books?id=nmEGHJy9uswC&hl=en

26. Cannon WB. ORGANIZATION FOR PHYSIOLOGICAL HOMEOSTASIS. Physiol Rev. 1929;9: 399–431. doi:10.1152/physrev.1929.9.3.399

27. Prior BM, Lloyd PG, Yang HT, Terjung RL. Exercise-induced vascular remodeling. Exerc Sport Sci Rev. 2003;31: 26–33. doi:10.1097/00003677-200301000-00006

28. Matsumoto T, Hayashi K. Mechanical and dimensional adaptation of rat aorta to hypertension. J Biomech Eng. 1994/08/01. 1994;116: 278–283. doi:10.1115/1.2895731

29. Eberth JF, Cardamone L, Humphrey JD. Evolving biaxial mechanical properties of mouse carotid arteries in hypertension. J Biomech. 2011/08/20. Elsevier; 2011;44:

2532–2537. doi:10.1016/j.jbiomech.2011.07.018

30. Rosenson RS, McCormick A, Uretz EF. Distribution of blood viscosity values and biochemical correlates in healthy adults. Clin Chem. 1996;42. Available: http://clinchem.aaccjnls.org/content/42/8/1189.short

31. de Bruyne B, Bartunek J, Sys SU, Pijls NHJ, Heyndrickx GR, Wijns W. Simultaneous Coronary Pressure and Flow Velocity Measurements in Humans Feasibility, Reproducibility, and Hemodynamic Dependence of Coronary Flow Velocity Reserve, Hyperemic Flow Versus Pressure Slope Index, and Fractional Flow Reserve. Circulation. 1996;94: 1842–1849.

32. Humphrey JD, Eberth JF, Dye WW, Gleason RL. Fundamental role of axial stress in compensatory adaptations by arteries. J Biomech. 2008/12/17. 2009;42: 1–8. doi:10.1016/j.jbiomech.2008.11.011

33. Kamiya A, Togawa T. Adaptive regulation of wall shear stress to flow change in the canine carotid artery. Am J Physiol. 1980/07/01. 1980;239: H14-21.

34. Langille BL, O'Donnell F. Reductions in arterial diameter produced by chronic decreases in blood flow are endothelium-dependent. Science (80-). 1986;231: 405–407. doi:10.1126/science.3941904

35. Langille BL. Arterial remodeling: relation to hemodynamics. Can J Physiol Pharmacol. Canada; 1996;74: 834–841.

36. Baeyens N, Nicoli S, Coon BG, Ross TD, Van den Dries K, Han J, et al. Vascular remodeling is governed by a VEGFR3-dependent fluid shear stress set point. Elife. eLife Sciences Publications Limited; 2015;4: e04645. doi:10.7554/eLife.04645

37. Hayashi K, Kakoi D, Makino A. Remodeling of the arterial wall: Response to

restoration of normal blood flow after flow reduction. Biorheology. IOS Press; 2018;54: 95–108. doi:10.3233/BIR-17146

38. Hayashi K, Mori K, Miyazaki H. Biomechanical response of femoral vein to chronic elevation of blood pressure in rabbits. Am J Physiol Heart Circ Physiol. 2003;284: H511-8. doi:10.1152/ajpheart.00620.2002

39. Matsumoto T, Okumura E, Shirono T, Sho E, Masuda H, Sato M. Flow-induced changes in dimensions and mechanical properties of rabbit common carotid arteries. JSME Int Journal, Ser C Mech Syst Mach Elem Manuf. 2006;48. doi:10.1299/jsmec.48.477

40. Fridez P, Zulliger M, Bobard F, Montorzi G, Miyazaki H, Hayashi K, et al. Geometrical, functional, and histomorphometric adaptation of rat carotid artery in induced hypertension. J Biomech. Elsevier; 2003;36: 671–680. doi:10.1016/S0021-9290(02)00445-1

41. Choy JS, Dang Q, Molloi S, Kassab GS. Nonuniformity of axial and circumferential remodeling of large coronary veins in response to ligation. Am J Physiol Circ Physiol. American Physiological Society; 2006;290: H1558–H1565. doi:10.1152/ajpheart.00928.2005

42. Dobrin PB, Littooy FN, Endean ED. Mechanical factors predisposing to intimal hyperplasia and medial thickening in autogenous vein grafts. Surgery. 1989;105: 393–400.

43. Matsumoto T, Hayashi K. Stress and Strain Distribution in Hypertensive and Normotensive Rat Aorta Considering Residual Strain. J Biomech Eng. ASME; 1996;118: 62–73.

44. Gleason RL, Wilson E, Humphrey JD. Biaxial biomechanical adaptations of mouse carotid arteries cultured at altered axial extension. J Biomech. 2007;40: 766–776. doi:http://dx.doi.org/10.1016/j.jbiomech.2006.03.018

45. Powell JT, Gosling M. Molecular and cellular changes in vein grafts: influence of pulsatile stretch. Curr Opin Cardiol. 1998/11/21. 1998;13: 453–458.

46. Eberth JF, Gresham VC, Reddy AK, Popovic N, Wilson E, Humphrey JD. Importance of pulsatility in hypertensive carotid artery growth and remodeling. J Hypertens. 2009/07/09. 2009;27: 2010–2021. doi:10.1097/HJH.0b013e32832e8dc8

47. Eberth JF, Popovic N, Gresham VC, Wilson E, Humphrey JD. Time course of carotid artery growth and remodeling in response to altered pulsatility. Am J Physiol Hear Circ Physiol. 2010/09/21. 2010;299: H1875-83. doi:10.1152/ajpheart.00872.2009

48. Chien S. Mechanotransduction and endothelial cell homeostasis: the wisdom of the cell. Am J Physiol Hear Circ Physiol. 2007;292: H1209–H1224. doi:10.1152/ajpheart.01047.2006

49. Humphrey JD, Dufresne ER, Schwartz M a. Mechanotransduction and extracellular matrix homeostasis. Nat Rev Mol Cell Biol. 2014;15: 802–812. doi:10.1038/nrm3896

50. Jalali S, del Pozo MA, Chen K-D, Miao H, Li Y-S, Schwartz MA, et al. Integrin-mediated mechanotransduction requires its dynamic interaction with specific extracellular matrix (ECM) ligands. Proc Natl Acad Sci. 2001;98: 1042–1046. doi:10.1073/pnas.98.3.1042

51. Desart KM, Butler K, O'Malley KA, Jiang Z, Berceli SA. Time and flow-dependent

changes in the p27(kip1) gene network drive maladaptive vascular remodeling. Journal of Vascular Surgery. Elsevier; 2015. p. 1296–1302.e2. doi:10.1016/j.jvs.2014.05.015

52. Berard X, Déglise S, Alonso F, Saucy F, Meda P, Bordenave L, et al. Role of hemodynamic forces in the ex vivo arterialization of human saphenous veins. J Vasc Surg. 2013;57: 1371–1382. doi:http://dx.doi.org/10.1016/j.jvs.2012.09.041

53. Bolitho GA, Hollis TM. Aortic Histomine Syntesis in Experimental Neurogenic Hypertension. Exp Biol Med. 1975;148: 1189–1192. doi:10.3181/00379727-148-38714

54. Shyy YJ, Hsieh HJ, Usami S, Chien S. Fluid shear stress induces a biphasic response of human monocyte chemotactic protein 1 gene expression in vascular endothelium. Proc Natl Acad Sci. 1994;91.

55. Malek AM, Greene AL, Izumo S. Regulation of endothelin 1 gene by fluid shear stress is transcriptionally mediated and independent of protein kinase C and cAMP. Proc Natl Acad Sci. 1993;90: 5999–6003. Available: http://www.pnas.org/content/90/13/5999.abstract

56. Dewey CF, Bussolari SR, Gimbrone MA, Davies PF. The dynamic response of vascular endothelial cells to fluid shear stress. J Biomech Eng. 1981;103: 177–85. Available: http://www.ncbi.nlm.nih.gov/pubmed/7278196

57. Davies PF, Remuzzi A, Gordon EJ, Dewey Jr. CF, Gimbrone Jr. MA. Turbulent fluid shear stress induces vascular endothelial cell turnover in vitro. Proc Natl Acad Sci U S A. 1986;83: 2114–2117. doi:10.1073/pnas.83.7.2114

58. Ziegler T, Bouzourene K, Harrison VJ, Brunner HR, Hayoz D. Influence of

Oscillatory and Unidirectional Flow Environments on the Expression of Endothelin and Nitric Oxide Synthase in Cultured Endothelial Cells. Arterioscler Thromb Vasc Biol. 1998;18: 686–692. doi:10.1161/01.atv.18.5.686

59. Hsiai TK, Cho SK, Wong PK, Ing M, Salazar A, Sevanian A, et al. Monocyte recruitment to endothelial cells in response to oscillatory shear stress. FASEB J. NIH Public Access; 2003;17: 1648–57. doi:10.1096/fj.02-1064com

60. Blackman BR, García-Cardeña G, Gimbrone MA. A new in vitro model to evaluate differential responses of endothelial cells to simulated arterial shear stress waveforms. J Biomech Eng. 2002;124: 397–407. Available: http://www.ncbi.nlm.nih.gov/pubmed/12188206

61. Kaunas R, Usami S, Chien S. Regulation of stretch-induced JNK activation by stress fiber orientation. Cell Signal. 2006;18: 1924–31. doi:10.1016/j.cellsig.2006.02.008

62. Kaunas R, Nguyen P, Usami S, Chien S. Cooperative effects of Rho and mechanical stretch on stress fiber organization. Proc Natl Acad Sci U S A. 2005;102: 15895–900. doi:10.1073/pnas.0506041102

63. Zhao S, Suciu A, Ziegler T, Moore JE, Bürki E, Meister JJ, et al. Synergistic effects of fluid shear stress and cyclic circumferential stretch on vascular endothelial cell morphology and cytoskeleton. Arterioscler Thromb Vasc Biol. American Heart Association, Inc.; 1995;15: 1781–6. doi:10.1161/01.ATV.15.10.1781

64. Li YS, Haga JH, Chien S. Molecular basis of the effects of shear stress on vascular endothelial cells. J Biomech. 2005;38: 1949–1971. doi:10.1016/j.jbiomech.2004.09.030

65. Tarbell JM, Shi ZD, Dunn J, Jo H. Fluid Mechanics, Arterial Disease, and Gene

Expression. Annu Rev Fluid Mech. 2014;46: 591–614. doi:10.1146/annurev-fluid-010313-141309

66. Davies PF, Barbee KA, Volin M V, Robotewskyj A, Chen J, Joseph L, et al. SPATIAL RELATIONSHIPS IN EARLY SIGNALING EVENTS OF FLOW-MEDIATED ENDOTHELIAL MECHANOTRANSDUCTION. Annu Rev Physiol. 1997;59: 527–549. doi:doi:10.1146/annurev.physiol.59.1.527

67. Leung DYM, Glagov S, Mathews MB. Cyclic stretching stimulates synthesis of matrix components by arterial smooth muscle cells in vitro. Science (80-). 1976;191: 475–477. doi:10.1126/science.128820

68. Tozzi CA, Christiansen DL, Poiani GJ, Riley DJ. Excess collagen in hypertensive pulmonary arteries decreases vascular distensibility. Am J Respir Crit Care Med. 1994;149: 1317–1326. doi:10.1164/ajrccm.149.5.8173773

69. Scott D, Tan Y, Shandas R, Stenmark KR, Tan W. High Pulsatility Flow Stimulates Smooth Muscle Cell Hypertrophy and Contractile Protein Expression. AJP Lung Cell Mol Physiol. 2012; 70–81. doi:10.1152/ajplung.00342.2012

70. Mills CJ, Gabe IT, Gault JH, Mason DT, Ross J, Braunwald E, et al. Pressure-flow relationships and vascular impedance in man. Cardiovasc Res. 1970;4: 405 LP-417. Available: http://cardiovascres.oxfordjournals.org/content/4/4/405.abstract

71. London GM, Guerin AP. Influence of arterial pulse and reflected waves on blood pressure and cardiac function. Am Hear J. 1999/09/01. 1999;138: 220–224. doi:a100205 [pii]

72. O'rourke MF. Vascular impedance in studies of arterial and cardiac function. Physiol Rev. Am Physiological Soc; 1982;62: 570–623.

73. Ku DN. Blood Flow in Arteries. Annu Rev Fluid Mech. 1997;29: 399–434. doi:10.1146/annurev.fluid.29.1.399

74. Dai G, Kaazempur-Mofrad MR, Natarajan S, Zhang Y, Vaughn S, Blackman BR, et al. Distinct endothelial phenotypes evoked by arterial waveforms derived from atherosclerosis-susceptible and -resistant regions of human vasculature. Proc Natl Acad Sci. 2004;101: 14871–14876. doi:10.1073/pnas.0406073101

75. Feaver RE, Gelfand BD, Blackman BR. Human haemodynamic frequency harmonics regulate the inflammatory phenotype of vascular endothelial cells. Nat Commun. 2013;4: 1525. doi:10.1038/ncomms2530

76. Herman IM, Brant AM, Warty VS, Bonaccorso J, Klein EC, Kormos RL, et al. Hemodynamics and the vascular endothelial cytoskeleton. J Cell Biol. Rockefeller University Press; 1987;105: 291–302. doi:10.1083/JCB.105.1.291

77. Berceli SA, Borovetz HS, Sheppeck RA, Moosa HH, Warty VS, Armany MA, et al. Mechanisms of vein graft atherosclerosis: LDL metabolism and endothelial actin reorganization. J Vasc Surg. Elsevier; 1991;13: 336–347. doi:10.1016/0741-5214(91)90227-L

78. Clerin V, Gusic RJ, O'Brien J, Kirshbom PM, Myung RJ, Gaynor JW, et al. Mechanical environment, donor age, and presence of endothelium interact to modulate porcine artery viability ex vivo. Ann Biomed Eng. 2002/12/28. 2002;30: 1117–1127.

79. Bardy N, Merval R, Benessiano J, Samuel JL, Tedgui A. Pressure and angiotensin II synergistically induce aortic fibronectin expression in organ culture model of rabbit aorta. Evidence for a pressure-induced tissue renin-angiotensin system. Circ

Res. American Heart Association, Inc.; 1996;79: 70–8. doi:10.1161/01.RES.79.1.70

80. Montorzi G, Silacci P, Zulliger M, Stergiopulos N. Functional, mechanical and geometrical adaptation of the arterial wall of a non-axisymmetric artery in vitro. J Hypertens. 2004;22: 339–47. Available: http://www.ncbi.nlm.nih.gov/pubmed/15076192

81. Prandi F, Piola M, Soncini M, Colussi C, D'Alessandra Y, Penza E, et al. Adventitial Vessel Growth and Progenitor Cells Activation in an Ex Vivo Culture System Mimicking Human Saphenous Vein Wall Strain after Coronary Artery Bypass Grafting. Madeddu P, editor. PLoS One. Public Library of Science; 2015;10: e0117409. doi:10.1371/journal.pone.0117409

82. Han HC, Marita S, Ku DN. Changes of opening angle in hypertensive and hypotensive arteries in 3-day organ culture. J Biomech. 2006;39: 2410–2418. doi:10.1016/j.jbiomech.2005.08.003

83. Dummler S, Eichhorn S, Tesche C, Schreiber U, Voss B, Deutsch MA, et al. Pulsatile ex vivo perfusion of human saphenous vein grafts under controlled pressure conditions increases MMP-2 expression. Biomed Eng Online. 2011;10: 62. doi:10.1186/1475-925X-10-62

84. Gusic RJ, Myung R, Petko M, Gaynor JW, Gooch KJ. Shear stress and pressure modulate saphenous vein remodeling ex vivo. J Biomech. 2005;38: 1760–1769. doi:10.1016/j.jbiomech.2004.10.030

85. Yoshigi M, Keller BB. Characterization of embryonic aortic impedance with lumped parameter models. Am Physiol Soc. 1997;273: H19–H27.

86. Yoshigi M, Knott GD, Keller BB. Lumped parameter estimation for the embryonic

chick vascular system: a time-domain approach using MLAB. Comput Methods Programs Biomed. Elsevier; 2000;63: 29–41.

87. Stergiopulos N, Westerhof BE, Westerhof N. Total arterial inertance as the fourth element of the windkessel model. Am J Physiol Circ Physiol. Am Physiological Soc; 1999;276: H81–H88.

88. Westerhof N, Elzinga G, Sipkema P. An artificial arterial system for pumping hearts. J Appl Physiol. 1971/11/01. 1971;31: 776–781.

89. Westerhof N, Lankhaar JW, Westerhof BE. The arterial Windkessel. Med Biol Eng Comput. 2008/06/11. 2009;47: 131–141. doi:10.1007/s11517-008-0359-2

90. Eriksson A, Persson HW, Lindström K. A computer-controlled arbitrary flow wave form generator for physiological studies. Rev Sci Instrum. American Institute of Physics; 1999;71: 235. doi:10.1063/1.1150189

91. Tsai W, Savaş Ö. Flow pumping system for physiological waveforms. Med Biol Eng Comput. Springer-Verlag; 2010;48: 197–201. doi:10.1007/s11517-009-0573-6

92. Kung EO, Taylor CA. Development of a Physical Windkessel Module to Re-Create In Vivo Vascular Flow Impedance for In Vitro Experiments. Cardiovasc Eng Technol. 2011;2: 2–14. doi:10.1007/s13239-010-0030-6

93. Pahlevan NM, Gharib M. In-vitro investigation of a potential wave pumping effect in human aorta. J Biomech. Elsevier; 2013;46: 2122–9. doi:10.1016/j.jbiomech.2013.07.006

94. Gusic RJ, Petko M, Myung R, Gaynor JW, Gooch KJ. Mechanical properties of native and ex vivo remodeled porcine saphenous veins. J Biomech. 2005;38: 1770–1779. doi:10.1016/j.jbiomech.2005.04.002

95. Paroz A, Probst H, Saucy F, Mazzolai L, Rizzo E, Ris H-B, et al. Comparison of morphological and functional alterations of human saphenous veins after seven and fourteen days of ex vivo perfusion. Eur Surg Res. Karger Publishers; 2004;36: 274–81. doi:10.1159/000079912

96. Saucy F, Probst H, Alonso F, Berard X, Deglise S, Dunoyer-Geindre S, et al. Ex vivo pulsatile perfusion of human saphenous veins induces intimal hyperplasia and increased levels of the plasminogen activator inhibitor 1. Eur Surg Res. 2010/08/28. 2010;45: 50–59. doi:10.1159/000318602

97. Miyakawa AA, Dallan LAO, Lacchini S, Borin TF, Krieger JE. Human saphenous vein organ culture under controlled hemodynamic conditions. Clinics (Sao Paulo). 2008;63: 683–8. Available: http://www.ncbi.nlm.nih.gov/pubmed/18925330

98. Campos LC, Miyakawa AA, Barauna VG, Cardoso L, Borin TF, Dallan LA, et al. Induction of CRP3/MLP expression during vein arterialization is dependent on stretch rather than shear stress. Cardiovasc Res. 2009;83: 140–147. doi:10.1093/cvr/cvp108

99. Piola M, Prandi F, Bono N, Soncini M, Penza E, Agrifoglio M, et al. A compact and automated ex vivo vessel culture system for the pulsatile pressure conditioning of human saphenous veins. J Tissue Eng Regen Med. 2013; n/a-n/a. doi:10.1002/term.1798

100. Piola M, Prandi F, Fiore GB, Agrifoglio M, Polvani G, Pesce M, et al. Human Saphenous Vein Response to Trans-wall Oxygen Gradients in a Novel Ex Vivo Conditioning Platform. Ann Biomed Eng. 2016;44: 1449–1461. doi:10.1007/s10439-015-1434-0

101. Piola M, Ruiter M, Vismara R, Mastrullo V, Agrifoglio M, Zanobini M, et al. Full Mimicking of Coronary Hemodynamics for Ex-Vivo Stimulation of Human Saphenous Veins. Ann Biomed Eng. Springer US; 2017;45: 884–897. doi:10.1007/s10439-016-1747-7

102. Sabik JF, Bansilal S, Lytle BW. Chapter 65. Coronary Bypass Surgery. In: Fuster V, Walsh RA, Harrington RA, editors. Hurst's The Heart, 13e. New York, NY: The McGraw-Hill Companies; 2011. Available: http://mhmedical.com/content.aspx?aid=7822960

103. Lloyd-Jones D, Adams RJ, Brown TM, Carnethon M, Dai S, De Simone G, et al. Heart Disease and Stroke Statistics—2010 Update: A Report From the American Heart Association. Circulation. 2009/12/19. 2010;121: e46–e215. doi:10.1161/circulationaha.109.192667

104. US Department of Health and Human Services. National Hospital Discharge Survey 2010. 2013.

105. Calafiore AM, Di Giammarco G, Teodori G, D'Annunzio E, Vitolla G, Fino C, et al. Radial artery and inferior epigastric artery in composite grafts: Improved midterm angiographic results. Ann Thorac Surg. 1995;60: 517–524. doi:10.1016/0003-4975(95)00479-5

106. Cao C, Manganas C, Horton M, Bannon P, Munkholm-Larsen S, Ang SC, et al. Angiographic outcomes of radial artery versus saphenous vein in coronary artery bypass graft surgery: A meta-analysis of randomized controlled trials. J Thorac Cardiovasc Surg. 2013;146: 255–261.

107. Cohen G, Tamariz MG, Sever JY, Liaghati N, Guru V, Christakis GT, et al. The

radial artery versus the saphenous vein graft in contemporary CABG: a case-matched study. Ann Thorac Surg. 2001/02/24. 2001;71: 180–186. doi:10.1016/S0003-4975(00)02285-2

108. Desai ND, Cohen EA, Naylor CD, Fremes SE. A randomized comparison of radial-artery and saphenous-vein coronary bypass grafts. N Engl J Med. 2004/11/27. 2004;351: 2302–2309. doi:10.1056/NEJMoa040982

109. Fiore AC, Naunheim KS, Dean P, Kaiser GC, Pennington DG, Willman VL, et al. Results of internal thoracic artery grafting over 15 years: single versus double grafts. Ann Thorac Surg. 1990;49: 202–209.

110. Fitzgibbon GM, Kafka HP, Leach AJ, Keon WJ, Hooper GD, Burton JR. Coronary bypass graft fate and patient outcome: Angiographic follow-up of 5,065 grafts related to survival and reoperation in 1,388 patients during 25 years. J Am Coll Cardiol. 1996;28: 616–626. doi:10.1016/0735-1097(96)00206-9

111. Goldman S, Sethi GK, Holman W, Thai H, McFalls E, Ward HB, et al. Radial artery grafts vs saphenous vein grafts in coronary artery bypass surgery: a randomized trial. Jama. 2011/01/13. 2011;305: 167–174. doi:10.1001/jama.2010.1976

112. Hess CN, Lopes RD, Gibson CM, Hager R, Wojdyla DM, Englum BR, et al. Saphenous Vein Graft Failure After Coronary Artery Bypass Surgery: Insights From PREVENT IV. Circulation. 2014;130: 1445–1451. doi:10.1161/circulationaha.113.008193

113. Loop FD, Lytle BW, Cosgrove DM, Stewart RW, Goormastic M, Williams GW, et al. Influence of the Internal-Mammary-Artery Graft on 10-Year Survival and Other Cardiac Events. N Engl J Med. 1986;314: 1–6.

doi:10.1056/NEJM198601023140101

114. Maniar HS, Sundt TM, Barner HB, Prasad SM, Peterson L, Absi T, et al. Effect of target stenosis and location on radial artery graft patency. J Thorac Cardiovasc Surg. 2002;123: 45–52. doi:10.1067/mtc.2002.118686

115. Royse AG, Royse CF, Tatoulis J, Grigg LE, Shah P, Hunt D, et al. Postoperative radial artery angiography for coronary artery bypass surgery. Eur J Cardio-Thoracic Surg. 2000;17: 294–304. doi:10.1016/s1010-7940(99)00364-4

116. Sabik 3rd JF, Lytle BW, Blackstone EH, Houghtaling PL, Cosgrove DM. Comparison of saphenous vein and internal thoracic artery graft patency by coronary system. Ann Thorac Surg. 2005/02/01. 2005;79: 544–551. doi:10.1016/j.athoracsur.2004.07.047

117. Zacharias A, Habib RH, Schwann TA, Riordan CJ, Durham SJ, Shah A. Improved Survival With Radial Artery Versus Vein Conduits in Coronary Bypass Surgery With Left Internal Thoracic Artery to Left Anterior Descending Artery Grafting. Circulation. 2004;109: 1489–1496. Available: http://circ.ahajournals.org/content/109/12/1489.abstract

118. Bassiouny HS, White S, Glagov S, Choi E, Giddens DP, Zarins CK. Anastomotic intimal hyperplasia: Mechanical injury or flow induced. J Vasc Surg. 1992;15: 708–717. doi:10.1016/0741-5214(92)90019-5

119. Hofer M, Rappitsch G, Perktold K, Trubel W, Schima H. Numerical study of wall mechanics and fluid dynamics in end-to-side anastomoses and correlation to intimal hyperplasia. J Biomech. Elsevier; 1996;29: 1297–1308. doi:10.1016/0021-9290(96)00036-X

120. Fung YC. What are the residual stresses doing in our blood vessels? Ann Biomed Eng. 1991/01/01. 1991;19: 237–249. doi:10.1007/BF02584301

121. Rachev A, Stergiopulos N, Meister JJ. A Model for Geometric and Mechanical Adaptation of Arteries to Sustained Hypertension. J Biomech Eng. 1998;120: 9–17. doi:10.1115/1.2834313

122. Zwolak RM, Adams MC, Clowes AW. Kinetics of vein graft hyperplasia: association with tangential stress. J Vasc Surg. 1987/01/01. 1987;5: 126–136.

123. Bank AJ, Wang H, Holte JE, Mullen K, Shammas R, Kubo SH. Contribution of Collagen, Elastin, and Smooth Muscle to In Vivo Human Brachial Artery Wall Stress and Elastic Modulus. Circulation. 1996;94: 3263–3270. doi:10.1161/01.cir.94.12.3263

124. Cox RH. Passive mechanics and connective tissue composition of canine arteries. Am J Physiol. 1978;234: H533–H541.

125. Roach MR, Burton AC. The reason for the shape of the distensibility curves of arteries. Can J Biochem Physiol. 1957/08/01. 1957;35: 681–690. doi:10.1139/o57-080

126. Konig G, McAllister TN, Dusserre N, Garrido SA, Iyican C, Marini A, et al. Mechanical properties of completely autologous human tissue engineered blood vessels compared to human saphenous vein and mammary artery. Biomaterials. THE BOULEVARD, LANGFORD LANE, KIDLINGTON, OXFORD OX5 1GB, OXON, ENGLAND: ELSEVIER SCI LTD; 2009;30: 1542–1550. doi:10.1016/j.biomaterials.2008.11.011

127. Chamiot-Clerc P, Copie X, Renaud J-F, Safar M, Girerd X. Comparative reactivity

and mechanical properties of human isolated internal mammary and radial arteries. Cardiovasc Res. 1998;37: 811–819. doi:10.1016/S0008-6363(97)00267-8

128. Zambanini A, Cunningham SL, Parker KH, Khir AW, Thom SAM, Hughes AD. Wave-energy patterns in carotid, brachial, and radial arteries: a noninvasive approach using wave-intensity analysis. Am J Physiol Circ Physiol. 2005;289: H270–H276.

129. Canham PB, Finlay HM, Boughner DR. Contrasting structure of the saphenous vein and internal mammary artery used as coronary bypass vessels. Cardiovasc Res. 1997/06/01. 1997;34: 557–567. doi:10.1016/S0008-6363(97)00056-4

130. Dobrin PB, Schwarcz TH, Mrkvicka R. Longitudinal retractive force in pressurized dog and human arteries. J Surg Res. 1990;48: 116–120.

131. Stick C, Hiedl U, Witzleb E. Venous pressure in the saphenous vein near the ankle during changes in posture and exercise at different ambient temperatures. Eur J Appl Physiol Occup Physiol. 1993/01/01. 1993;66: 434–438.

132. Khonsari S, Sintek C, Ardehali A. Cardiac Surgery: Safeguards and Pitfalls in Operative Technique. Wolters Kluwer Health/Lippincott Williams & Wilkins; 2008.

133. Benedetto U, Codispoti M. Age cutoff for the loss of survival benefit from use of radial artery in coronary artery bypass grafting. J Thorac Cardiovasc Surg. 2013/09/17. 2013;146: 1075–1078. doi:10.1016/j.jtcvs.2013.07.025

134. Effler DB, Favaloro RG, Groves LK. Coronary artery surgery utilizing saphenous vein graft techniques. Clinical experience with 224 operations. J Thorac Cardiovasc Surg. 1970;59: 147.

135. Cheng A, Slaughter MS. How I choose conduits and configure grafts for my

patients-rationales and practices. Ann Cardiothorac Surg. 2013;2: 527–532. doi:10.3978/j.issn.2225-319X.2013.07.17

136. Van Loon P. Length-force and volume-pressure relationships of arteries. Biorheology. 1976;14: 181–201.

137. Eberth JF, Taucer AI, Wilson E, Humphrey JD. Mechanics of carotid arteries in a mouse model of Marfan Syndrome. Ann Biomed Eng. 2009/04/08. 2009;37: 1093–1104. doi:10.1007/s10439-009-9686-1

138. Zhou B, Wolf L, Rachev A, Shazly T. A structure-motivated model of the passive mechanical response of the primary porcine renal artery. J Mech Med Biol. World Scientific Publishing Co.; 2013;14: 1450033. doi:10.1142/S021951941450033X

139. Zhou B, Wolf L, Rachev A, Shazly T. A structure-motivated model of the passive mechanical response of the primary porcine renal artery. J Mech Med Biol. 2014;14: 18. doi:10.1142/s021951941450033x

140. Gundiah N, B Ratcliffe M, A Pruitt L. Determination of strain energy function for arterial elastin: Experiments using histology and mechanical tests. J Biomech. 2007;40: 586–594. doi:10.1016/j.jbiomech.2006.02.004

141. Zulliger M a., Fridez P, Hayashi K, Stergiopulos N. A strain energy function for arteries accounting for wall composition and structure. J Biomech. 2004;37: 989–1000. doi:10.1016/j.jbiomech.2003.11.026

142. Bersi MR, Ferruzzi J, Eberth JF, Gleason Jr. RL, Humphrey JD. Consistent Biomechanical Phenotyping of Common Carotid Arteries from Seven Genetic, Pharmacological, and Surgical Mouse Models. Ann Biomed Eng. Springer US; 2014;42: 1207–1223. doi:10.1007/s10439-014-0988-6

143. Zeinali-Davarani S, Choi J, Baek S. On parameter estimation for biaxial mechanical behavior of arteries. J Biomech. Elsevier; 2009;42: 524–530.

144. Cheng J, Stoilov I, Mecham R, Wagenseil J. A fiber-based constitutive model predicts changes in amount and organization of matrix proteins with development and disease in the mouse aorta. Biomech Model Mechanobiol. Springer-Verlag; 2013;12: 497–510. doi:10.1007/s10237-012-0420-9

145. Ferruzzi J, Bersi MR, Humphrey JD. Biomechanical phenotyping of central arteries in health and disease: Advantages of and methods for murine models. Ann Biomed Eng. 2013;41. doi:10.1007/s10439-013-0799-1

146. O'Connor WN, Valle S. A combination Verhoeff's elastic and Masson's trichrome stain for routine histology. Stain Technol. 1982/07/01. 1982;57: 207–210. doi:10.3109/10520298209066710

147. Landini G. Advanced shape analysis with ImageJ. Proceedings of the Second ImageJ User and Developer Conference. Luxembourg; 2008. pp. 116–121. Available: http://www.mecourse.com/landinig/software/software.html

148. Parissis H, Ramesh BC, Al-Alao B. Which is the best graft for the right coronary artery? Asian Cardiovasc Thorac Ann. 2014/03/04. 2014; doi:10.1177/0218492314523766

149. Raja SG, Haider Z, Ahmad M, Zaman H. Saphenous vein grafts: to use or not to use? Hear Lung Circ. 2004;13: 150–156. doi:10.1016/j.hlc.2004.03.013

150. Schwann TA, Tranbaugh RF, Dimitrova KR, Engoren MC, Kabour A, Hoffman DM, et al. Time-varying survival benefit of radial artery versus vein grafting: a multiinstitutional analysis. Ann Thorac Surg. 2013/12/24. 2014;97: 1328–34;

discussion 1334. doi:10.1016/j.athoracsur.2013.09.096

151. Cox JL, Chiasson DA, Gotlieb AI. Stranger in a Strange Land: The Pathogenesis of Saphenous Vein Graph Stenosis With Emphasis on Structural and Functional Differences Between Veins and Arteries. Prog Cardiovasc Dis. 1991;34: 45–68.

152. Ballyk PD, Walsh C, Butany J, Ojha M. Compliance mismatch may promote graft–artery intimal hyperplasia by altering suture-line stresses. J Biomech. 1997;31: 229–237.

153. Wang C, Guo X, Kassab GS. A new observation on the stress distribution in the coronary artery wall. J Biomech Eng. 2009;131: 111011.

154. Veselý J, Horný L, Chlup H, Adámek T, Krajíček M, Žitný R. Constitutive modeling of human saphenous veins at overloading pressures. J Mech Behav Biomed Mater. 2015;45: 101–108. doi:http://dx.doi.org/10.1016/j.jmbbm.2015.01.023

155. Guo X, Kassab GS. Distribution of stress and strain along the porcine aorta and coronary arterial tree. Am J Physiol Circ Physiol. 2004;286: H2361–H2368.

156. Rachev A, Greenwald SE. Residual strains in conduit arteries. J Biomech. 2003;36: 661–670.

157. Hwang M, Berceli SA, Garbey M, Kim NH, Tran-Son-Tay R. The dynamics of vein graft remodeling induced by hemodynamic forces: a mathematical model. Biomech Model Mechanobiol. 2011/06/22. 2012;11: 411–423. doi:10.1007/s10237-011-0321-3

158. Ramachandra AB, Sankaran S, Humphrey JD, Marsden AL. Computational simulation of the adaptive capacity of vein grafts in response to increased pressure. 2014;

159. Shazly T, Rachev A, Lessner S, Argraves WS, Ferdous J, Zhou B, et al. On the Uniaxial Ring Test of Tissue Engineered Constructs. Exp Mech. 2015;55: 41–51. doi:10.1007/s11340-014-9910-2

160. Twal WO, Klatt SC, Harikrishnan K, Gerges E, Cooley MA, Trusk TC, et al. Cellularized microcarriers as adhesive building blocks for fabrication of tubular tissue constructs. Ann Biomed Eng. 2013/08/15. 2014;42: 1470–1481. doi:10.1007/s10439-013-0883-6

161. McFetridge PS, Chaudhuri JB. Design of Vascular Graft Bioreactors. In: Chaudhuri JB, Al-Rubeai M, editors. Bioreactors for Tissue Engineering: Principles, Design, and Operation. Netherlands: Springer; 2005. pp. 269–283.

162. Horny L, Adamek T, Gultova E, Zitny R, Vesely J, Chlup H, et al. Correlations between age, prestrain, diameter and atherosclerosis in the male abdominal aorta. J Mech Behav Biomed Mater. 2011;4: 2128–2132. doi:http://dx.doi.org/10.1016/j.jmbbm.2011.07.011

163. Kamenskiy A V, Pipinos II, Dzenis YA, Phillips NY, Desyatova AS, Kitson J, et al. Effects of age on the physiological and mechanical characteristics of human femoropopliteal arteries. Acta Biomater. 2015;11: 304–313. doi:http://dx.doi.org/10.1016/j.actbio.2014.09.050

164. Baek S, Valentín A, Humphrey JD. Biochemomechanics of Cerebral Vasospasm and its Resolution: II. Constitutive Relations and Model Simulations. Ann Biomed Eng. Springer US; 2007;35: 1498–1509. doi:10.1007/s10439-007-9322-x

165. Harskamp RE, Lopes RD, Baisden CE, de Winter RJ, Alexander JH. Saphenous vein graft failure after coronary artery bypass surgery: pathophysiology,

management, and future directions. Ann Surg. 2013;257: 824–833. doi:10.1097/SLA.0b013e318288c38d

166. Owens CD, Gasper WJ, Rahman AS, Conte MS. Vein graft failure. J Vasc Surg. Elsevier; 2015;61: 203–216. doi:10.1016/j.jvs.2013.08.019

167. Rachev A, Greenwald S, Shazly T. Are geometrical and structural variations along the length of the aorta governed by a principle of "optimal mechanical operation"? J Biomech Eng. 2013/06/01. 2013;135: 81006. doi:10.1115/1.4024664

168. Jones EA V, le Noble F, Eichmann A. What determines blood vessel structure? Genetic prespecification vs. hemodynamics. Physiology. 2006;21: 388–95. doi:10.1152/physiol.00020.2006

169. Kudo FA, Muto A, Maloney SP, Pimiento JM, Bergaya S, Fitzgerald TN, et al. Venous Identity Is Lost but Arterial Identity Is Not Gained During Vein Graft Adaptation. Arterioscler Thromb Vasc Biol. 2007;27: 1562–1571. doi:10.1161/atvbaha.107.143032

170. Chiu JJ, Chien S. Effects of disturbed flow on vascular endothelium: pathophysiological basis and clinical perspectives. Physiol Rev. 2011;91: 327–387. doi:10.1152/physrev.00047.2009

171. Chiu J-J, Usami S, Chien S. Vascular endothelial responses to altered shear stress: Pathologic implications for atherosclerosis. Ann Med. 2009;41: 19–28. doi:doi:10.1080/07853890802186921

172. Haga JH, Li YS, Chien S. Molecular basis of the effects of mechanical stretch on vascular smooth muscle cells. J Biomech. 2007;40: 947–960. doi:10.1016/j.jbiomech.2006.04.011

173. Wilson E, Mai Q, Sudhir K, Weiss RH, Ives HE. Mechanical strain induces growth of vascular smooth muscle cells via autocrine action of PDGF. J Cell Biol. 1993;123: 741–747. doi:10.1083/jcb.123.3.741

174. Majesky MW. Developmental basis of vascular smooth muscle diversity. Arter Thromb Vasc Biol. 2007;27: 1248–1258. doi:10.1161/ATVBAHA.107.141069

175. Awgulewitsch A, Majesky MW. Interpreting inflammation: smooth muscle positional identity and nuclear factor-kappaB signaling. Arter Thromb Vasc Biol. 2013;33: 1113–1115. doi:10.1161/ATVBAHA.113.301407

176. Intengan HD, Schiffrin EL. Vascular Remodeling in Hypertension. Hypertension. 2001;38: 581–587. doi:10.1161/hy09t1.096249

177. Galis ZS, Khatri JJ. Matrix metalloproteinases in vascular remodeling and atherogenesis: the good, the bad, and the ugly. Circ Res. 2002;90: 251–262. doi:10.1161/hh0302.105345

178. Tamura K, Chen YE, Lopez-Ilasaca M, Daviet L, Tamura N, Ishigami T, et al. Molecular mechanism of fibronectin gene activation by cyclic stretch in vascular smooth muscle cells. J Biol Chem. 2000;275: 34619–34627. doi:10.1074/jbc.M004421200

179. Feng Y, Yang JH, Huang H, Kennedy SP, Turi TG, Thompson JF, et al. Transcriptional Profile of Mechanically Induced Genes in Human Vascular Smooth Muscle Cells. Circ Res. 1999;85: 1118–1123. doi:10.1161/01.res.85.12.1118

180. Sorescu GP, Sykes M, Weiss D, Platt MO, Saha A, Hwang J, et al. Bone morphogenic protein 4 produced in endothelial cells by oscillatory shear stress stimulates an inflammatory response. J Biol Chem. 2003;278: 31128–31135.

doi:10.1074/jbc.M300703200

181. O'Callaghan CJ, Williams B. Mechanical Strain-Induced Extracellular Matrix Production by Human Vascular Smooth Muscle Cells : Role of TGF- 1. Hypertension. 2000;36: 319–324. doi:10.1161/01.hyp.36.3.319

182. Azhar M, Schultz JEJ, Grupp I, Dorn GW, Meneton P, Molin DGM, et al. Transforming growth factor beta in cardiovascular development and function. Cytokine Growth Factor Rev. Elsevier; 2003;14: 391–407.

183. Pfaffl MW. A new mathematical model for relative quantification in real-time RT–PCR. Nucleic Acids Res. Oxford, UK: Oxford University Press; 2001;29: e45–e45. Available: http://www.ncbi.nlm.nih.gov/pmc/articles/PMC55695/

184. Deglise S, Martin D, Probst H, Saucy F, Hayoz D, Waeber G, et al. Increased connexin43 expression in human saphenous veins in culture is associated with intimal hyperplasia. J Vasc Surg. 2005;41: 1043–1052. doi:10.1016/j.jvs.2005.02.036

185. Voisard R, Ramiz E, Baur R, Gastrock-Balitsch I, Siebeneich H, Frank O, et al. Pulsed perfusion in a venous human organ culture model with a Windkessel function (pulsed perfusion venous HOC-model). Med Sci Monit. 2010/10/29. 2010;16: Cr523-9.

186. Hu Y, Davison F, Zhang Z, Xu Q. Endothelial Replacement and Angiogenesis in Arteriosclerotic Lesions of Allografts Are Contributed by Circulating Progenitor Cells. Circulation. 2003;108: 3122 LP-3127.

187. Lindner V. Balloon Denudation of Blood Vessels BT - Methods in Endothelial Cell Biology. In: Augustin HG, editor. Berlin, Heidelberg: Springer Berlin Heidelberg;

2004. pp. 187–195. doi:10.1007/978-3-642-18725-4_18

188. Hu Y, Mayr M, Metzler B, Erdel M, Davison F, Xu Q. Both Donor and Recipient Origins of Smooth Muscle Cells in Vein Graft Atherosclerotic Lesions. Circ Res. 2002;91: e13 LP-e20.

189. Zhang L, Freedman NJ, Brian L, Peppel K. Graft-Extrinsic Cells Predominate in Vein Graft Arterialization. Arterioscler Thromb Vasc Biol. 2004;24: 470 LP-476.

190. Leach DF, Nagarkatti M, Nagarkatti P, Cui T. Functional states of resident vascular stem cells and vascular remodeling. Front Biol (Beijing). 2015;10: 387–397. doi:10.1007/s11515-015-1375-x

191. Ramachandra AB, Humphrey JD, Marsden AL. Gradual loading ameliorates maladaptation in computational simulations of vein graft growth and remodelling. J R Soc Interface. The Royal Society; 2017;14. doi:10.1098/rsif.2016.0995

192. McDonald DA. Blood flow in arteries. 2nd ed. London: Edward Arnold; 1974.

193. Faury G. Function-structure relationship of elastic arteries in evolution: from microfibrils to elastin and elastic fibres. Pathol Biol. 2001/06/29. 2001;49: 310–325. doi:S0369-8114(01)00147-X [pii]

194. Mills CJ, Gabe IT, Gault JH, Mason DT, Ross Jr. J, Braunwald E, et al. Blood velocity and pressure wave-forms in the major arteries in man. Clin Sci. 1970;38: 10P.

195. Wilson E, Sudhir K, Ives HE. Mechanical strain of rat vascular smooth muscle cells is sensed by specific extracellular matrix/integrin interactions. J Clin Invest. 1995;96: 2364–72. doi:10.1172/JCI118293

196. Helmlinger G, Geiger R V, Schreck S, Nerem RM. Effects of pulsatile flow on

cultured vascular endothelial cell morphology. J Biomech Eng. 1991;113: 123–131.

197. Matsumoto T, Okumura E, Miura Y, Sato M. Mechanical and dimensional adaptation of rabbit carotid artery cultured in vitro. Med Biol Eng Comput. 1999;37: 252–256. doi:10.1007/BF02513295

198. Muluk SC, Vorp DA, Severyn DA, Gleixner S, Johnson PC, Webster MW. Enhancement of tissue factor expression by vein segments exposed to coronary arterial hemodynamics. J Vasc Surg. 1998;27: 521–527. doi:10.1016/S0741-5214(98)70327-1

199. Piola M, Ruiter M, Vismara R, Mastrullo V, Agrifoglio M, Zanobini M, et al. Full Mimicking of Coronary Hemodynamics for Ex-Vivo Stimulation of Human Saphenous Veins. Ann Biomed Eng. 2017;45: 884–897. doi:10.1007/s10439-016-1747-7

200. Stegemann JP, Nerem RM. Phenotype Modulation in Vascular Tissue Engineering Using Biochemical and Mechanical Stimulation. Ann Biomed Eng. 2003;31: 391–402. doi:10.1114/1.1558031

201. Yamada KM, Cukierman E. Modeling tissue morphogenesis and cancer in 3D. Cell. 2007;130: 601–10. doi:10.1016/j.cell.2007.08.006

202. Freshney RI. Culture of animal cells: a manual of basic technique and specialized applications. 6th ed. Hoboken, N.J.: Wiley-Blackwell; 2010.

203. Patel DJ, Defreitas FM, Fry DL. Hydraulic input impedance to aorta and pulmonary artery in dogs. J Appl Physiol. 1963;18: 134–40.

204. Grant BJ, Paradowski LJ. Characterization of pulmonary arterial input impedance with lumped parameter models. Am J Physiol. 1987;252: H585–H593.

205. Jager GN, Westerhof N, Noordergraaf A. Oscillatory Flow Impedance in Electrical Analog of Arterial System: Representation of Sleeve Effect and Non-Newtonian Properties of Blood. Circ Res. 1965;16: 121–133. doi:10.1161/01.RES.16.2.121

206. Newby AC, Zaltsman AB. Molecular mechanisms in intimal hyperplasia. J Pathol. 2000;190: 300–309.

207. Smith JO. Mathematics of the discrete Fourier transform (DFT): with audio applications. Julius Smith; 2007.

208. Lijnen HR, Silence J, Lemmens G, Frederix L, Collen D. Regulation of gelatinase activity in mice with targeted inactivation of components of the plasminogen/plasmin system. Thromb Haemost. Schattauer GmbH; 1998;79: 1171–1176.

209. Milnor WR. Hemodynamics. 2nd ed. Baltimore: Williams & Wilkins; 1989.

210. Meschia JF, Klaas JP, Brown RD, Brott TG. Evaluation and Management of Atherosclerotic Carotid Stenosis. Mayo Clin Proc. Mayo Foundation for Medical Education and Research; 2017;92: 1144–1157. doi:10.1016/j.mayocp.2017.02.020

211. Go AS, Mozaffarian D, Roger VL, Benjamin EJ, Berry JD, Blaha MJ, et al. Heart Disease and Stroke Statistics—2014 Update: A Report From the American Heart Association. Circulation. 2014;129: e28–e292. doi:10.1161/01.cir.0000441139.02102.80

212. Flaherty ML, Kissela B, Khoury JC, Alwell K, Moomaw CJ, Woo D, et al. Carotid Artery Stenosis as a Cause of Stroke. Neuroepidemiology. 2013;40: 36–41. doi:10.1159/000341410

213. Fernández-Friera L, Peñalvo JL, Fernández-Ortiz A, Ibañez B, López-Melgar B,

Laclaustra M, et al. Prevalence, vascular distribution, and multiterritorial extent of subclinical atherosclerosis in a middle-aged cohort the PESA (Progression of Early Subclinical Atherosclerosis) study. Circulation. 2015;131: 2104–2113. doi:10.1161/CIRCULATIONAHA.114.014310

214. Paini A, Boutouyrie P, Calvet D, Zidi M, Agabiti-Rosei E, Laurent S. Multiaxial mechanical characteristics of carotid plaque. Stroke. Am Heart Assoc; 2007;38: 117–123.

215. Safar ME, Blacher J, Mourad JJ, London GM. Stiffness of carotid artery wall material and blood pressure in humans. Stroke. Am Heart Assoc; 2000;31: 782–790.

216. Brott TG, Hobson RW, Howard G, Roubin GS, Clark WM, Brooks W, et al. Stenting versus endarterectomy for treatment of carotid-artery stenosis. N Engl J Med. Mass Medical Soc; 2010;363: 11–23.

217. Rolland PH, Mekkaoui C, Vidal V, Berry JL, Moore JE, Moreno M, et al. Compliance matching stent placement in the carotid artery of the swine promotes optimal blood flow and attenuates restenosis. Eur J Vasc Endovasc Surg. Elsevier; 2004;28: 431–438.

218. Rolland PH, Charifi A-B, Verrier C, Bodard H, Friggi A, Piquet P, et al. Hemodynamics and wall mechanics after stent placement in swine iliac arteries: comparative results from six stent designs. Radiology. Radiological Society of North America; 1999;213: 229–246.

219. Takamizawa K. Biaxial Contractile Mechanics of Common Carotid Arteries of Rabbit. J Biomech Eng. 2014;137: 5–7. doi:10.1115/1.4028988

220. Zhou B, Alshareef M, Prim DA, Collins M, Kempner M, Hartstone-Rose A, et al.

The perivascular environment along the vertebral artery governs segment-specific structural and mechanical properties. Acta Biomater. 2016;45: 286–295. doi:10.1016/j.actbio.2016.09.004

221. Cardamone L, Valentin A, Eberth JF, Humphrey JD. Origin of axial prestretch and residual stress in arteries. Biomech Model Mechanobiol. 2009/01/06. 2009;8: 431–446. doi:10.1007/s10237-008-0146-x

222. Holt JP, Rhode EA, Holt WW, Kines H. Geometric similarity of aorta, venae cavae, and certain of their branches in mammals. Am J Physiol. 1981;241: R100-4.

223. Weinberg PD, Ross Ethier C. Twenty-fold difference in hemodynamic wall shear stress between murine and human aortas. J Biomech. 2007;40: 1594–8. doi:10.1016/j.jbiomech.2006.07.020

224. Levine HJ. Editorial - Rest Heart Rate and Life Expectancy. J Am Coll Cardiol. 1997;30: 1104–1106.

225. Cox RH. Comparison of carotid artery mechanics in the rat, rabbit, and dog. Am J Physiol. 1978;234: H280-8.

226. Gleason RL, Gray SP, Wilson E, Humphrey JD. A multiaxial computer-controlled organ culture and biomechanical device for mouse carotid arteries. J Biomech Eng. 2005/03/31. 2004;126: 787–795.

227. Zhou B, Prim DA, Romito EJ, McNamara LP, Spinale FG, Shazly T, et al. Contractile Smooth Muscle and Active Stress Generation in Porcine Common Carotids. J Biomech Eng. American Society of Mechanical Engineers; 2017;140: 14501. doi:10.1115/1.4037949

228. Hu J-J, Baek S, Humphrey JD. Stress–strain behavior of the passive basilar artery

in normotension and hypertension. J Biomech. Elsevier; 2007;40: 2559–2563.

229. Weizsäcker HW, Lambert H, Pascale K. Analysis of the passive mechanical properties of rat carotid arteries. J Biomech. 1983;16: 703–715. doi:https://doi.org/10.1016/0021-9290(83)90080-5

230. Takamizawa K. Biaxial Contractile Mechanics of Common Carotid Arteries of Rabbit. J Biomech Eng. 2015;137: 31010. doi:10.1115/1.4028988

231. Kohn JC, Lampi MC, Reinhart-King CA. Age-related vascular stiffening: Causes and consequences. Front Genet. 2015;6: 1–17. doi:10.3389/fgene.2015.00112

232. von Maltzahn WW, Warriyar RG, Keitzer WF. Experimental measurements of elastic properties of media and adventitia of bovine carotid arteries. J Biomech. 1984;17: 839–847. doi:https://doi.org/10.1016/0021-9290(84)90142-8

233. Blondel WCPM, Didelon J, Maurice G, Carteaux J-P, Xiong Wang, Stolz J-F. Investigation of 3-D mechanical properties of blood vessels using a new in vitro tests system: results on sheep common carotid arteries. IEEE Trans Biomed Eng. 2001;48: 442–451. doi:10.1109/10.915710

234. Daugs A, Hutzler B, Meinke M, Schmitz C, Lehmann N, Markhoff A, et al. Detergent-Based Decellularization of Bovine Carotid Arteries for Vascular Tissue Engineering. Ann Biomed Eng. Springer; 2017;45: 2683–2692.

235. Schmidt CE, Baier JM. Acellular vascular tissues: natural biomaterials for tissue repair and tissue engineering. Biomaterials. 2000;21: 2215–2231. doi:https://doi.org/10.1016/S0142-9612(00)00148-4

236. Sommer G, Holzapfel GA. 3D constitutive modeling of the biaxial mechanical response of intact and layer-dissected human carotid arteries. J Mech Behav Biomed

Mater. Elsevier Ltd; 2012;5: 116–128. doi:10.1016/j.jmbbm.2011.08.013

237. Masson I, Boutouyrie P, Laurent S, Humphrey JD, Zidi M. Characterization of arterial wall mechanical behavior and stresses from human clinical data. J Biomech. 2008;41: 2618–2627. doi:10.1016/j.jbiomech.2008.06.022

238. von Maltzahn W-W, Besdo D, Wiemer W. Elastic properties of arteries: A nonlinear two-layer cylindrical model. J Biomech. 1981;14: 389–397. doi:10.1016/0021-9290(81)90056-7

239. Wolinsky H, Glagov S. A Lamellar Unit of Aortic Medial Structure and Function in Mammals. Circ Res. 1967;20: 99 LP-111.

240. West GB, Brown JH, Enquist BJ. A general model for the origin of allometric scaling laws in biology. Science (80-). American Association for the Advancement of Science; 1997;276: 122–126.

241. Fung YC. The mechanical properties of living tissues. New York:Springer–Verlag. Springer New York; 1993.

242. Benrashid E, McCoy CC, Youngwirth LM, Kim J, Manson RJ, Otto JC, et al. Tissue engineered vascular grafts: Origins, development, and current strategies for clinical application. METHODS. 525 B ST, STE 1900, SAN DIEGO, CA 92101-4495 USA: ACADEMIC PRESS INC ELSEVIER SCIENCE; 2016;99: 13–19. doi:10.1016/j.ymeth.2015.07.014

243. Dahl SLM, Koh J, Prabhakar V, Niklason LE. Decellularized native and engineered arterial scaffolds for transplantation. Cell Transplant. 2003;12: 659–666. doi:10.3727/000000003108747136

244. Lawson J, Dahl S, Prichard H, Manson R, Gage S, Kypson A, et al. VS5 Human

Tissue-Engineered Grafts for Hemodialysis: Development, Preclinical Data, and Early Investigational Human Implant Experience. J Vasc Surg. 2014;59: 32S–33S. doi:http://dx.doi.org/10.1016/j.jvs.2014.03.077

245. Niklason LE, Gao J, Abbott WM, Hirschi KK, Houser S, Marini R, et al. Functional Arteries Grown in Vitro. Science (80-). American Association for the Advancement of Science; 1999;284: 489–493. doi:10.1126/science.284.5413.489

246. Sheridan WS, Duffy GP, Murphy BP. Mechanical characterization of a customized decellularized scaffold for vascular tissue engineering. J Mech Behav Biomed Mater. 2012;8: 58–70. doi:10.1016/j.jmbbm.2011.12.003

247. Dolan EB, Gunning GM, Davis TA, Cooney G, Eufrasio T, Murphy BP. The development and mechanical characterisation of a novel reinforced venous conduit that mimics the mechanical properties of an arterial wall. J Mech Behav Biomed Mater. PO BOX 211, 1000 AE AMSTERDAM, NETHERLANDS: ELSEVIER SCIENCE BV; 2017;71: 23–31. doi:10.1016/j.jmbbm.2017.02.012

248. de Vries MR, Simons KH, Jukema JW, Braun J, Quax PHA. Vein graft failure: from pathophysiology to clinical outcomes. Nat Rev Cardiol. 2016;13: 451–470. doi:10.1038/nrcardio.2016.76

249. Shuhaiber JH, Evans AN, Massad MG, Geha AS. Mechanisms and future directions for prevention of vein graft failure in coronary bypass surgery. Eur J Cardiothorac Surg. 2002/09/03. 2002;22: 387–396.

250. Gooch KJ, Firstenberg MS, Shrefler BS, Scandling BW. Biomechanics and Mechanobiology of Saphenous Vein Grafts. J Biomech Eng. American Society of Mechanical Engineers; 2018;140: 20804. doi:10.1115/1.4038705

251. Kassab GS, Navia JA. Biomechanical considerations in the design of graft: the homeostasis hypothesis. Annu Rev Biomed Eng. 2006/07/13. 2006;8: 499–535. doi:10.1146/annurev.bioeng.8.010506.105023

252. Sodek J, Ferrier JM. Collagen remodelling in rat periodontal tissues: compensation for precursor reutilization confirms rapid turnover of collagen. Coll Relat Res. Elsevier; 1988;8: 11–21.

253. McAnulty RJ, Laurent GJ. Collagen synthesis and degradation in vivo. Evidence for rapid rates of collagen turnover with extensive degradation of newly synthesized collagen in tissues of the adult rat. Coll Relat Res. Elsevier; 1987;7: 93–104.

254. Langleben D, Szarek JL, Coflesky JT, Jones RC, Reid LM, Evans JN. Altered artery mechanics and structure in monocrotaline pulmonary hypertension. J Appl Physiol. Am Physiological Soc; 1988;65: 2326–2331.

255. Cyron CJ, Humphrey JD. Growth and remodeling of load-bearing biological soft tissues. Meccanica. Springer Netherlands; 2017;52: 645–664. doi:10.1007/s11012-016-0472-5

256. Sakaguchi K, Shimizu T, Horaguchi S, Sekine H, Yamato M, Umezu M, et al. In Vitro Engineering of Vascularized Tissue Surrogates. Sci Rep. Nature Publishing Group; 2013;3: 1316. doi:10.1038/srep01316

257. Jeong SI, Kwon JH, Lim JI, Cho SW, Jung Y, Sung WJ, et al. Mechano-active tissue engineering of vascular smooth muscle using pulsatile perfusion bioreactors and elastic PLCL scaffolds. Biomaterials. 2005;26: 1405–1411. doi:10.1016/j.biomaterials.2004.04.036

258. Huang AH, Niklason LE. Engineering of arteries in vitro. Cell Mol Life Sci. 2014;71: 2103–2118. doi:10.1007/s00018-013-1546-3

APPENDIX A

JOURNAL PERMISSION FOR USE OF MANUSCRIPT

Published Journal Article (https://www.elsevier.com/about/our-business/policies/sharing/published-journal-article)

Policies for sharing published journal articles differ for subscription and gold open access articles:

Subscription articles

- If you are an author, please share a link to your article rather than the full-text. Millions of researchers have access to the formal publications on ScienceDirect, and so links will help your users to find, access, cite, and use the best available version
- If you are an author, you may also share your Published Journal Article privately with known students or colleagues for their personal use
- Theses and dissertations which contain embedded PJAs as part of the formal submission can be posted publicly by the awarding institution with DOI links back to the formal publications on ScienceDirect
- If you are affiliated with a library that subscribes to ScienceDirect you have additional private sharing rights for others' research accessed under that agreement. This includes use for classroom teaching and internal training at the institution (including use in course packs and courseware programs), and inclusion of the article for grant funding purposes
- Otherwise sharing is by agreement only (https://www.elsevier.com/about/our-business/policies/hosting/commercial-platforms)

Figure A.1 – Permission from Journal of Mechanical Behavior of Biomedical Materials to include published manuscript in this dissertation (Chapter 2).